

## Special Issue on Electrical Power Engineering

This special issue offers a wide range of case studies, empirical research and professional analysis based on the analysis of relevant sources, to assist the academic teacher, researcher or professional dealing with electric power engineering. The special issue is unique in that it does not focus on a single theme on electric power engineering, but provides insights into the world and practices of co-disciplines that are integrally linked to electric power engineering. This edition contains articles from the field of diagnostics of electrical insulation systems represented by "Dielectric Relaxation Spectroscopy of Modern Hybrid Insulation Systems", where the study includes research on modern insulation systems based on hybrid and non-hybrid nanofluid-paper. Another field is represented by the "Investigation of shielding materials for the purposes of shielding the electromagnetic fields" where investigation of the shielding effectiveness of shielding material HSF 54 and window foil Profilon Antispy was investigated. Power system modelling is represented by "Unsymmetrical Three-phase Power System Model: Design and Application". This paper deals with enhancing the three-phase network model for simulation of both symmetrical and unsymmetrical networks under both normal and faulted operation. The field of renewable energy sources was represented with four papers. First paper deals about Operability satisfaction of energy systems with nuclear power plants at different photovoltaic penetration levels. Second paper is focusing on recent challenges regarding the verification of photovoltaic inverters properties and their compliance with technical requirements. Third deal about the role of flexibility resources in the energy transition and fourth focusing on Data driven additive fault detection of wind turbines. The field of energy accumulation is represented by a paper which deals with energy storage system utilization in distribution power system.

We are very thankful to all the authors and the co-authors for their devotion during the formulation of contributions for this special issue and for sharing their results with the journal. Last but not least, we are sincerely thankful to the editorial board of journal Acta Polytechnica Hungarica for preparing and managing this issue technically, as well as Prof. Imre J. Rudas and Prof. Levente Kovács for supporting the publication of this Special Issue.

Zsolt Čonka

Guest Editor

# Asymmetrical, Three-phase Power System Model: Design and Application

**Karel Máslo<sup>1,2</sup>, Jan Koudelka<sup>2</sup>, Branislav Bátorá<sup>2</sup>,  
Václav Vyčítal<sup>2</sup>**

<sup>1</sup>ČEPS, a.s., Transmission System Analysis Department, Elektrárenská 774/2,  
101 52 Prague, Czech Republic, maslo@ceps.cz

<sup>2</sup>Brno University of Technology, Department of Electrical Power Engineering,  
Faculty of Electrical Engineering and Communication, Technická 3082/12, 616 00  
Brno, Czech Republic, maslo@vut.cz, xkoude20@vut.cz, batora@vut.cz,  
vycital@vut.cz

---

*Abstract: The paper deals with enhancing the three-phase network model, for simulation of both symmetrical and asymmetrical networks, under both normal and faulted operation. The modelling approach, which was implemented into the MODES simulation tool, is described in a great detail. Demonstration of the application of the MODES simulation tool, newly extended by the three-phase model, in the field of simultaneous faults analysis, distribution system protection and voltage unbalance evaluation, is done, using simulations on simple test systems. Simulations are complemented by discussion of achieved results and validation is accomplished by using other simulation tools (PSCAD/EMTDC, OpenDSS). Finally, conclusions and future plans for the model extension and its possible applications are presented.*

*Keywords: power system unbalance; network asymmetry; three-phase model; dynamic simulation*

---

## 1 Introduction

For conventional studies, analyses and simulations, transmission power systems are modelled as symmetrical, which is a significant simplification. Symmetrical three-phase power system can be analyzed as a single-phase equivalent, which makes computations and analyses (e.g., load flow studies) significantly faster. The assumption of symmetry in case of transmission systems is reasonable as, generally, transmission lines are transposed and loads, i.e., transformation to distribution system, are symmetrical. In addition, symmetrical fault of three-phase short circuit is frequently analyzed (e.g., for equipment dimensioning or stability assessment). However, distribution system analysis is a different case. There are

sources of significant asymmetry, such as loads not being distributed over phases evenly and lines not being entirely transposed, sometimes even not transposed at all (at medium voltage (MV) and low voltage (LV)) levels, and, last but not least, AC traction feeders. In case of distribution system, unbalanced faults are of importance. In practice, these faults occur more often than symmetrical ones, and they are also used for dimensioning purposes, which is e.g., the case of earth fault in case of impedance-grounded systems. Simultaneous unbalanced faults, such as double earth fault or an earth fault combined with a phase interruption, are simulation challenging, as they require appropriate simulation model and simulation can be time consuming. Even though these faults are uncommon, they practically occur in the distribution system, thus, there is a demand for their analysis.

Distribution system analysis includes a vast number of problems closely related to the grid asymmetry, which must be considered in grid modelling. Usage of the single-phase equivalent in this case is often impractical, sometimes even impossible, comparing to the transmission system analysis. The endeavor to build and use a three-phase model is though evident. However, it is not a trivial issue.

## 1.1 Motivation

MODES<sup>1</sup> simulation tool is a multi-purpose tool for power system dynamics analysis using RMS values (phasors). The simulation engine is used on a daily basis by the Czech Transmission System Operator, not only for load flow calculations and analyses, but also in the dispatch training simulator [1]. Various applications of MODES have been demonstrated in the past, e.g., in the field of stability analysis or short circuit calculations [2]. The simulation engine used to work with symmetrical components only, which allowed to speed up the calculation. However, current development of power systems and planned extension of the power system model by distribution systems imply the need for extending the existing simulation engine to be able to solve problems related to network asymmetry, which means mainly building the new models of grid elements. It is planned to use MODES for simulation of wide area distribution systems, more exactly for co-simulation of Czech transmission and distribution systems.

For such a big system, other solutions allowing analysis of unbalanced power system operation and fault analysis, such as PSCAD/EMTDC or OpenDSS, which were used for validation also in this paper, are a bit inconvenient. The disadvantage is the computation time and robustness – key aspects the newly designed model in MODES is aiming to improve.

Last but not least, MODES is used in Czech universities for teaching purposes. The possibility of simulation of distribution system can enrich the classes and bring new teaching methods, leading into the students are more familiar with the issue of power system dynamics. This issue is of importance in practice.

---

<sup>1</sup> More information about MODES is available from <http://www.modesinfo.com>.

## 1.2 Aims and Paper Structure

The main aim of the paper is to describe the design of the three-phase power system model, which has been implemented to the MODES simulation tool, and its application. The issue is split into three following chapters.

The second chapter gives the description of mathematical models, used for particular grid elements. These models are necessary for analysis of the three-phase power system. Their detailed description makes them replicable for other developers aiming to build the asymmetric power system models.

The third chapter shows three case studies (simulation cases), which were done in order to validate the built model after its implementation to MODES. The first case is the analysis of simultaneous faults; the second case is the operation of the impedance-grounded distribution network, and the last case is the evaluation of voltage unbalance caused by the AC traction feeders. Each case contains test system and simulation scenario description. The chapter shows the validation of results done using other simulation tools or analytical calculations, demonstrating that results from the newly designed model, implemented to MODES, are credible.

The last section concludes the paper and outlines the possible future application of the newly designed three-phase model, which is not only limited to the cases presented in this paper.

## 2 Three-Phase Models of Grid Elements

Symmetrical three-phase power system is easy to analyze, because such a system can be treated as a single-phase equivalent, which is, unfortunately, not applicable in case of an unsymmetrical power system. In general, two basic approaches can be used for power system modelling: analyze the system using phase values (A, B, C) or use symmetrical components (0, 1, 2). Symmetrical components and transition between these approaches are well described in the literature, e.g., in [3]. For application in MODES, the existing symmetrical network model has been extended by the asymmetrical models of basic elements, such as power source, power line, transformer, loads and fault model, which are described in this chapter.

### 2.1 Power Lines and Switches

In general, a three-phase power line with 3 phase conductors (A, B, C), neutral N, alternatively with ground wires, can be described with self-impedances  $\underline{Z}_{AA}$ ,  $\underline{Z}_{BB}$ ,  $\underline{Z}_{CC}$ , mutual impedances  $\underline{Z}_{AB}$ ,  $\underline{Z}_{AC}$ ,  $\underline{Z}_{BC}$ , self-capacitances  $C_{AA}$ ,  $C_{BB}$ ,  $C_{CC}$ , mutual capacitances  $C_{AB}$ ,  $C_{AC}$ ,  $C_{BC}$ , and shunt conductance  $G$ , representing leakage and corona losses. In case of the power line of multiple wires, e.g., low voltage (LV) line – A, B, C, N, the technique of Kron reduction [4] is applied to obtain a 3-wires

equivalent. The nodal admittance matrix (1) gives the relation between current injections to the sending (S) and receiving (R) bus  $\underline{\mathbf{I}}_S$ ,  $\underline{\mathbf{I}}_R$  and nodal voltages  $\underline{\mathbf{V}}_S$ ,  $\underline{\mathbf{V}}_R$ .

Switches are modelled also as power lines, with mutual impedance and mutual capacity equal to zero. Self-impedance has negligible value, e.g.,  $j0.1 \Omega$ .

$$\begin{bmatrix} \underline{\mathbf{I}}_S \\ \underline{\mathbf{I}}_R \end{bmatrix} = \begin{bmatrix} \underline{\mathbf{Z}}^{-1} + \frac{1}{2}\underline{\mathbf{Y}} & -\underline{\mathbf{Z}}^{-1} \\ -\underline{\mathbf{Z}}^{-1} & \underline{\mathbf{Z}}^{-1} + \frac{1}{2}\underline{\mathbf{Y}} \end{bmatrix} \begin{bmatrix} \underline{\mathbf{V}}_S \\ \underline{\mathbf{V}}_R \end{bmatrix} \quad \underline{\mathbf{Y}} = \mathbf{G} + j\omega\mathbf{C}$$

$$\underline{\mathbf{Z}} = \begin{bmatrix} \underline{Z}_{AA} & \underline{Z}_{AB} & \underline{Z}_{AC} \\ \underline{Z}_{AB} & \underline{Z}_{BB} & \underline{Z}_{BC} \\ \underline{Z}_{AC} & \underline{Z}_{BC} & \underline{Z}_{CC} \end{bmatrix} \quad \mathbf{C} = \begin{bmatrix} C_{AA} & -C_{AB} & -C_{AC} \\ -C_{AB} & C_{BB} & -C_{BC} \\ -C_{AC} & -C_{BC} & C_{CC} \end{bmatrix} \quad \mathbf{G} = \begin{bmatrix} G & 0 & 0 \\ 0 & G & 0 \\ 0 & 0 & G \end{bmatrix} \quad (1)$$

## 2.2 Transformers

Two conventional methods exist for modelling of a conventional, two-winding transformer: using phase values and transformer connection, or transition from symmetrical components values to phase values. Three-winding transformer can be modelled by combination of models of two-winding transformer.

### 2.2.1 Phase Values Model of Two-Winding Transformer

Phase values model of a transformer is built in three steps [5]: definition of the transformer primitive admittance matrix, calculation of the windings admittance matrix, and, finally, definition of the transformer admittance matrix using the previous two matrices and taking the vector group into consideration. This approach is described in a detail in [5] with all necessary equations.

### 2.2.2 Symmetrical Components Model of Two-Winding Transformer

The second approach is the symmetrical components model. We assume the transformer with wye-delta connection with solidly grounded neutral point. Considering the transformer admittance matrix in symmetrical components (2) to be known; P stands for primary side and S for secondary side.

$$\underline{\mathbf{Y}} \begin{bmatrix} \underline{\mathbf{I}}_{-P012} \\ \underline{\mathbf{I}}_{-S012} \end{bmatrix} = \begin{bmatrix} \underline{\mathbf{Y}}_{-PP012} & \underline{\mathbf{Y}}_{-PS012} \\ \underline{\mathbf{Y}}_{-PS012} & \underline{\mathbf{Y}}_{-SS012} \end{bmatrix} \begin{bmatrix} \underline{\mathbf{V}}_{-P012} \\ \underline{\mathbf{V}}_{-S012} \end{bmatrix}$$

$$\underline{\mathbf{I}}_{P012} = \begin{bmatrix} \underline{\mathbf{I}}_{P0} \\ \underline{\mathbf{I}}_{P1} \\ \underline{\mathbf{I}}_{P2} \end{bmatrix} \quad \underline{\mathbf{I}}_{S012} = \begin{bmatrix} \underline{\mathbf{I}}_{S0} \\ \underline{\mathbf{I}}_{S1} \\ \underline{\mathbf{I}}_{S2} \end{bmatrix} \quad \underline{\mathbf{V}}_{P012} = \begin{bmatrix} \underline{\mathbf{V}}_{P0} \\ \underline{\mathbf{V}}_{P1} \\ \underline{\mathbf{V}}_{P2} \end{bmatrix} \quad \underline{\mathbf{V}}_{S012} = \begin{bmatrix} \underline{\mathbf{V}}_{S0} \\ \underline{\mathbf{V}}_{S1} \\ \underline{\mathbf{V}}_{S2} \end{bmatrix} \quad (2)$$

For wye-delta connection with a solidly grounded neutral point, matrices of sequence admittances have form of (3), where Y is a leakage susceptance, evaluated from the short-circuit test, and p is transformer ratio.

$$\underline{Y}_{PP012} = \frac{Y}{p^2} \begin{bmatrix} 1 & 0 & 0 \\ 0 & 1 & 0 \\ 0 & 0 & 1 \end{bmatrix} \quad \underline{Y}_{PS012} = -\frac{Y}{p} \begin{bmatrix} 0 & 0 & 0 \\ 0 & 1 & 0 \\ 0 & 0 & 1 \end{bmatrix} \quad \underline{Y}_{SS012} = Y \begin{bmatrix} 0 & 0 & 0 \\ 0 & 1 & 0 \\ 0 & 0 & 1 \end{bmatrix} \quad (3)$$

Matrices (3) reflect the fact that delta winding connection does not allow zero sequence currents to flow. After the transition to phase values, admittance matrix can be expressed as (4).

$$\underline{Y} = Y \begin{bmatrix} \underline{Y}_{PP} & \underline{Y}_{PS} \\ \underline{Y}_{PS} & \underline{Y}_{SS} \end{bmatrix}$$

$$\underline{Y}_{PP} = \frac{1}{p^2} \begin{bmatrix} 1 & 0 & 0 \\ 0 & 1 & 0 \\ 0 & 0 & 1 \end{bmatrix} \quad \underline{Y}_{PS} = -\frac{1}{3p} \begin{bmatrix} 2 & -1 & -1 \\ -1 & 2 & -1 \\ -1 & 0 & 2 \end{bmatrix} \quad \underline{Y}_{SS} = \frac{1}{3} \begin{bmatrix} 2 & -1 & -1 \\ -1 & 2 & -1 \\ -1 & 0 & 2 \end{bmatrix} \quad (4)$$

The matrix (4) is advantageous because it does not cause phase displacement of voltage and current phasors, caused by vector group. For instance, differential protection can be easily modelled without the need of phase displacement compensation.

### 2.2.3 Three-Winding Transformer

Typical connection of a three-winding transformer is wye-wye-delta, where primary winding (wye) neutral point is solidly grounded, secondary winding (wye) neutral point is impedance grounded through the impedance  $Z_N$ , and tertiary winding (delta) is for compensation.

Primitive admittance matrix for three-winding transformer has a size of  $10 \times 10$ . It is more convenient though to use the symmetrical components method and replace the three-winding transformer by three two-winding transformers, as shown in Figure 1.

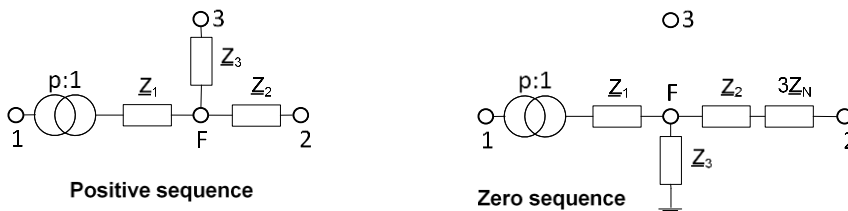


Figure 1

Equivalent diagram of three-winding transformer in symmetrical component representation

This model requires the addition of a fictive bus “F”, but previously developed models of two-winding transformers can be used. Zero sequence impedance diagram, shown in Figure 1, was taken from [6]. For simplified calculations, positive sequence impedances are equal to zero sequence ones. Tap changer is modelled on the primary side (first winding). It is assumed that transformer leakage reactance value varies with a square of transformer ratio, then tap changing does not change its value.

Values of impedances in branches  $\underline{Z}_1$ ,  $\underline{Z}_2$ ,  $\underline{Z}_3$  can be calculated using (5) from measured values from short-circuit test  $\underline{Z}_{12}$ ,  $\underline{Z}_{13}$ ,  $\underline{Z}_{23}$ , which usually have basis of the rated winding voltage and the largest apparent power of the transformer windings (usually the one with wye connection). Grounding impedance  $\underline{Z}_N$  has the basis of the winding to which neutral point the grounding impedance is connected.

$$\underline{Z}_1 = \frac{\underline{Z}_{12} + \underline{Z}_{13} - \underline{Z}_{23}}{2} \quad \underline{Z}_2 = \frac{\underline{Z}_{12} + \underline{Z}_{23} - \underline{Z}_{13}}{2} \quad \underline{Z}_3 = \frac{\underline{Z}_{13} + \underline{Z}_{23} - \underline{Z}_{12}}{2} \quad (5)$$

Following matrices  $\underline{Y}_1$  and  $\underline{Y}_2$  (6) can be used for the first and second winding (wye);  $\mathbf{1}$  is  $3 \times 3$  identity matrix. The third winding (delta) can be modelled by (4).

$$\underline{Y}_1 = \frac{1}{\underline{Z}_1} \begin{bmatrix} \mathbf{1} & \mathbf{1} \\ \frac{1}{p^2} & \frac{1}{p} \\ \frac{1}{p} & \mathbf{1} \end{bmatrix} \quad \underline{Y}_2 = \frac{1}{\underline{Z}_2} \begin{bmatrix} \underline{Y}' & -\underline{Y}' \\ -\underline{Y}' & \underline{Y}' \end{bmatrix} \quad \underline{Y}' = \begin{bmatrix} 1 - \underline{K} & -\underline{K} & -\underline{K} \\ -\underline{K} & 1 - \underline{K} & -\underline{K} \\ -\underline{K} & -\underline{K} & 1 - \underline{K} \end{bmatrix}$$

$$\underline{K} = \frac{1}{3 + \frac{\underline{Z}_2}{\underline{Z}_N}} \quad (6)$$

## 2.3 Generator

Generator can be modelled as an induced voltage  $\underline{E}$  behind the impedance – reactance  $X$ . Generator is considered to be symmetrical, thus voltage phasors  $\underline{E}_{ABC}$  are balanced and simply expressed as (7). For simplified calculations, induced voltage  $\underline{E}$  is considered to have constant value.

$$\underline{E}_{ABC} = \begin{bmatrix} 1 \\ \underline{a} \\ \underline{a}^2 \end{bmatrix} \underline{E} \quad (7)$$

## 2.4 Loads

The simplest model of a complex load (given by power  $\underline{S} = P + jQ$ ) in node with voltage  $\underline{V}$  has a form of constant admittances in ungrounded wye connection. After the elimination of voltage of wye connection, the following admittance matrix (8) is obtained.

$$\begin{bmatrix} \underline{Y}_A \left( 1 - \frac{\underline{Y}_A}{\underline{\Sigma Y}} \right) & -\frac{\underline{Y}_A \underline{Y}_B}{\underline{\Sigma Y}} & -\frac{\underline{Y}_A \underline{Y}_C}{\underline{\Sigma Y}} \\ -\frac{\underline{Y}_A \underline{Y}_B}{\underline{\Sigma Y}} & \underline{Y}_B \left( 1 - \frac{\underline{Y}_B}{\underline{\Sigma Y}} \right) & -\frac{\underline{Y}_B \underline{Y}_C}{\underline{\Sigma Y}} \\ -\frac{\underline{Y}_A \underline{Y}_C}{\underline{\Sigma Y}} & -\frac{\underline{Y}_B \underline{Y}_C}{\underline{\Sigma Y}} & \underline{Y}_C \left( 1 - \frac{\underline{Y}_C}{\underline{\Sigma Y}} \right) \end{bmatrix}$$

$$\underline{\Sigma Y} = \underline{Y}_A + \underline{Y}_B + \underline{Y}_C \quad \underline{Y}_i = \frac{\underline{S}_i^*}{U_i^2} \quad i = A, B, C \quad (8)$$

Also, compensation devices, such as capacitors and coils, can be modelled this way.

A special case of the load is the supply of the AC railway system from a V-connection (open delta) transformer. An example of a 25 kV system supplied from a 110 kV three-phase network is shown in Figure 2. These are actually two single-phase transformers T1 and T2, which are connected to the line-to-line voltage on the primary side (in an open delta – in V). Each of them feeds one section of the traction line from the secondary windings. For reasons of the phase changing, the individual sections are separated by a neutral section. When the train is crossing the neutral section, the power supply to the train is interrupted.

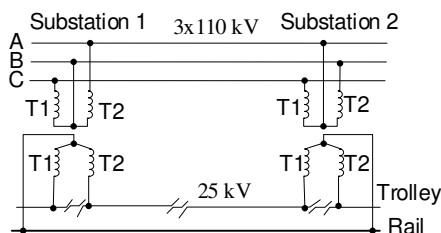


Figure 2

Diagram of power supply of the traction line from transformers connected to V

According to [6], the admittance matrix of such a power supply can be derived in the form of (9), where the left matrix is valid for Substation 1, and the right matrix is valid for Substation 2.  $N_1$  and  $N_2$  are the numbers of turns of the primary and secondary windings and  $Y_L$  is a load admittance connected to the secondary side of transformers T1 and T2.

$$\begin{bmatrix} \underline{Y}_2 & -\underline{Y}_2 & 0 \\ -\underline{Y}_2 & \underline{Y}_1 + \underline{Y}_2 & -\underline{Y}_1 \\ 0 & -\underline{Y}_1 & \underline{Y}_1 \end{bmatrix} \begin{bmatrix} \underline{Y}_1 + \underline{Y}_2 & -\underline{Y}_2 & -\underline{Y}_1 \\ -\underline{Y}_2 & \underline{Y}_2 & 0 \\ -\underline{Y}_1 & 0 & \underline{Y}_1 \end{bmatrix} \underline{Y}_i = \beta^2 \underline{Y}_{Li} \quad \beta = \frac{N_2}{N_1} \quad i = 1,2 \quad (9)$$

If we neglect the leakage reactance of the transformers and the resistances of the supplying lines, and replace the locomotive power consumption with only the active power  $P$ , the load admittance can be simply calculated according to (10).

$$\begin{cases} \underline{Y}_{L1} = \frac{1}{R-jkX} & \underline{Y}_{L2} = 0 & \text{for } -1 \leq k < 0 \\ \underline{Y}_{L1} = 0 & \underline{Y}_{L2} = \frac{1}{R+jkX} & \text{for } 0 < k \leq 1 \end{cases} \quad R = \frac{U^2}{P} \quad (10)$$

In (10),  $U$  is the voltage of the trolley (a nominal value can be considered for simplicity),  $X$  is the equivalent reactance of the entire section of the supplying lines, and  $k$  is a factor indicating the position of the train ( $k = -1$  if the train is at the end of the section fed by transformer T1 and  $k = 1$  if the train is at the end of the section fed by transformer T2). When the train outside the section is powered by transformers T1 and T2 and when the locomotive pantograph crosses the neutral section,  $k = 0$  and both admittances are zero (the power supply is interrupted).

## 2.5 Faults – Short Circuit and Phase Interruption

In phase values, both short circuit and phase interruption can be easily simulated by modification of admittance matrix (1). Short circuit or earth fault means the addition of an infinite value to the corresponding bus (assuming the fault occurred close to the bus), thus the corresponding element of admittance matrix has an infinite value. Phase interruption means the self-admittance of the faulted phase in admittance matrix is zero.

## 3 Application of the Model: Case Studies

This chapter demonstrates the use of the model for analysis of power system dynamics in three selected cases: simultaneous faults analysis, operation of arc suppression coil automatics and voltage unbalance calculations. Case studies were conducted on test networks to show the functionality of the model, but they are applicable to real power systems.

### 3.1 Analysis of Simultaneous Faults

Single unbalance fault (e.g., short circuit or phase interruption, which are the most common faults in distribution networks) can be analyzed using symmetrical components method, as described e.g., in [3]. However, situation is getting complicated when analyzing simultaneous faults. These faults can really occur in the power system – often, they happen consequently (especially due to overvoltage occurrence caused by the first fault). In case of simultaneous faults, especially if different phases are affected, it is recommended to use phase values instead of symmetrical components, which the newly implemented simulation model allows. MODES simulation tool is thus, suitable for simulation of such faults. A demonstration is completed in this section.

#### 3.1.1 Test System Description

A simple test system used for simultaneous faults analysis was taken from [8] and extended by a switch for simulation of a phase interruption. Diagram of the system is shown in Figure 3, together with parameters (reference is 116 kV, 100 MVA). The network was modelled as symmetrical; parameters are given as components values though. Matrices of phase values are created automatically by MODES (this is applicable only for symmetrical systems).

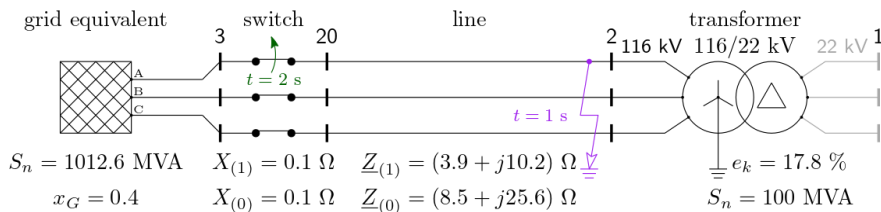


Figure 3

Diagram of the test system for analysis of simultaneous faults

### 3.1.2 Simulation of Simultaneous Earth Fault and Phase Interruption

Simulation scenario is also indicated in Figure 3: single phase A to ground fault (short circuit) near bus 2 is applied in 1 s, and interruption of phase A near bus 3 occurs in 2 s. It means that the short circuit is fed from two sides from 1 to 2 s, and from one side afterwards. Analyzed values were phase A currents on both sides of the line, which together give the fault current. Results are shown in Figure 4; solid lines are from MODES; dashed ones were obtained using PSCAD/EMTDC tool (it was used for simulation validation).

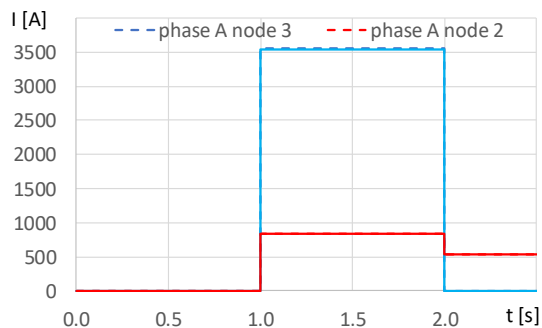


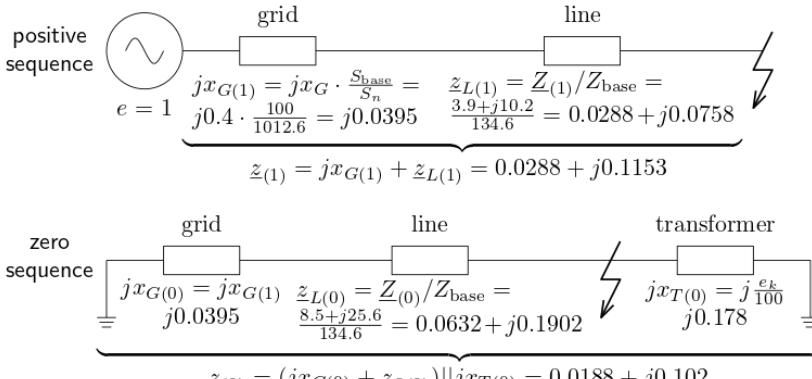
Figure 4

Phase A currents for single line to ground fault and phase A interruption; solid lines – MODES, dashed lines – PSCAD/EMTDC

The results of MODES and PSCAD/EMTDC are matching. The short-circuit current contributions from node 3 (blue waveforms) differs slightly, and the contribution from node 2 (red waveforms) matches completely. The fault current is initially given by a sum of currents from both sides, i.e., about 4400 A, and decays to approx. 500 A after the interruption. Simulation results match the fault currents computed in [8] as 3836 A and 478 A.

For better validation of results, fault current of a single phase to ground fault was computed analytically using symmetrical components. Analytical computation is demonstrated in Figure 5 (reactance of the switch was neglected). Analytically calculated short circuit current is equal to 4393 A. To conclude, the newly built

asymmetric model provides credible results in case of simulation of simultaneous faults, as the results were validated against another simulation tool and also analytical calculation.

$$Z_{\text{base}} = \frac{V_{\text{base}}^2}{S_{\text{base}}} = \frac{(116 \text{ kV})^2}{100 \text{ MVA}} = 134.6 \Omega$$


positive sequence

$$jx_{G(1)} = jx_G \cdot \frac{S_{\text{base}}}{S_n} = j0.4 \cdot \frac{100}{1012.6} = j0.0395$$

$$\underline{z}_{L(1)} = \frac{Z_{(1)}}{Z_{\text{base}}} = \frac{3.9 + j10.2}{134.6} = 0.0288 + j0.0758$$

$$\underline{z}_{(1)} = jx_{G(1)} + \underline{z}_{L(1)} = 0.0288 + j0.1153$$

zero sequence

$$jx_{G(0)} = jx_{G(1)} = j0.0395$$

$$\underline{z}_{L(0)} = \frac{Z_{(0)}}{Z_{\text{base}}} = \frac{8.5 + j25.6}{134.6} = 0.0632 + j0.1902$$

$$jx_{T(0)} = j \frac{e_k}{100} = j0.178$$

$$\underline{z}_{(0)} = (jx_{G(0)} + \underline{z}_{L(0)}) || jx_{T(0)} = 0.0188 + j0.102$$

$$I_{k1} = \frac{3e}{|2\underline{z}_{(1)} + \underline{z}_{(0)}|} \cdot \frac{S_{\text{base}}}{\sqrt{3}V_{\text{base}}} = \frac{3 \cdot 1}{|2 \cdot (0.0288 + j0.1153) + 0.0188 + j0.102|} \cdot \frac{100 \cdot 10^6}{\sqrt{3} \cdot 116 \cdot 10^3} \text{ A} = 4393 \text{ A}$$

Figure 5

Calculation of the single line to ground fault in the test system using symmetrical components method

### 3.1.3 Summary

The first case study showed the application of the created three-phase model for analysis of simultaneous earth fault and phase interruption, the most common faults in distribution networks, on a simple grid model taken from [8]. Results were validated by analytical calculation, by simulation in PSCAD/EMTDC software and also by comparison with results published in the reference [8].

## 3.2 Arc Suppression Coil Automatic Tracking System

Distribution systems, especially MV, are often operated as impedance-grounded. This way of operation increases the operational reliability, as the grid can be operated with an earth fault. On the other hand, it complicates the earth fault localization, which has to be done using advanced protection functions. Modelling of faulted distribution system operation requires advanced modelling possibilities, because asymmetry of line-to-ground capacities of power lines has to be considered, as well as shunt conductance. Otherwise, obtained results are not credible. This was also discussed in [9]. The case study demonstrates the simulation of an automation commonly installed in impedance-grounded MV distribution networks, which are arc suppression coil (ASC) tuning automation, equipped with parallel resistance connection. In addition, simulation of shunting system operation was done.



The parallel resistor  $R$  is commonly used in impedance-grounded system, comparing to the shunting system with resistor  $R_{sh}$ , depicted also in Figure 6. The shunting method (earthing the affected phase in the transformer substation) is described in [12] and [13], and it is applied in case of an earth fault with high resistance. Its aim is to reduce the residual current in fault location by moving the earth fault to the substation. Earthing of the affected phase is done also automatically with the ASCAT system.

### 3.2.2 Tuning of ASC in Fault-Free Operation

The first simulation demonstrates the previously described operation of ASCAT in fault-free operation. In the beginning, ASCAT is tuning the ASC into the resonance with one branch (line V3; line V2 is switched off). Then another branch (V2) is switched at  $t = 1$  s, followed by tuning of ASC to resonance with the new value of grid capacitance. Finally, at  $t = 2.5$  s, second branch (V2) is switched off. ASCAT activates the tuning of ASC again. Simulation results (ASC voltage) are shown in Figure 7a.

Resonance curves for a system equipped with ASC can be calculated analytically, based on the line parameters (conductance and capacity to ground). Resonance curves for the test system from Figure 6 are shown in Figure 7b, each curve correspond to the operational stage of the network (switched branches). Tuning process of ASC is indicated by arrows in Figure 7b. Each arrow is one step change of ASC impedance. Corresponding stages of ASC tuning are marked with numbers ① – ⑤ in Figure 7.

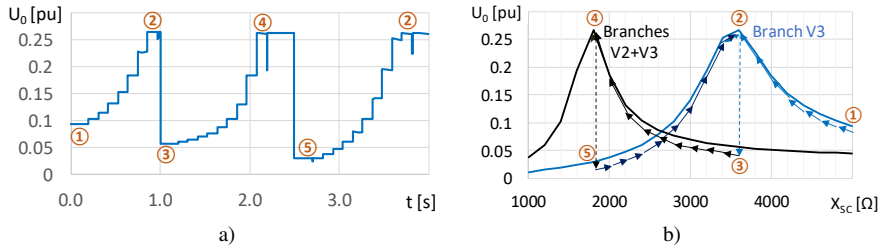


Figure 7

ASCAT test system operation (ASC tuning process) in fault-free operation: a) time course of ASC voltage  $U_0$ , b) ASC voltage  $U_0$  dependent on its impedance  $X_{SC}$  (resonance curves) for operation of one branch (V3) and two branches (V2+V3).

Theoretical value of ASC resonance reactance  $X_{SC}$  for operation of one line (V3) is given by equation (11) – it is equal to 3538  $\Omega$ . For two lines with the same length (operation of both V2 and V3), it is the half, i.e., 1769  $\Omega$ . Values of 3600  $\Omega$  and 1800  $\Omega$  respectively, used in simulation and shown in Figure 7b, are pretty matching.

$$X_{SC} = \frac{1}{B_A + B_B + B_C} = \frac{10^6}{3.14 \cdot 30 + 3.3 \cdot 30 + 2.98 \cdot 30} \Omega = 3538 \Omega \quad (11)$$

### 3.2.3 Earth Fault with Auxiliary Resistor Connection

In the following case, it is assumed that one branch (V3) is in operation, and ASC is tuned into resonance ( $X_{SC} = 3600 \Omega$ ) in the initial state. The earth fault at the end of the line V3 is applied at time  $t = 0.1$  s. ASCAT system automatically detects the earth fault (according to  $U_0$  voltage increase above 30%) and connects the auxiliary resistor for 0.1 s after the set delay of 0.1 s (processes were fastened for simulation purposes). Connecting the resistor eliminates the compensating effect of ASC, thus causes an increase of fault current to the value, which can be detected by earth fault protection.

Simulation results – line currents and ASC voltage – are plotted in Figure 8. Solid lines are the results from the MODES, dashed lines are the results obtained by the simulation validation in OpenDSS simulation tool; results are almost the same and they are overlapping in Figure 8.

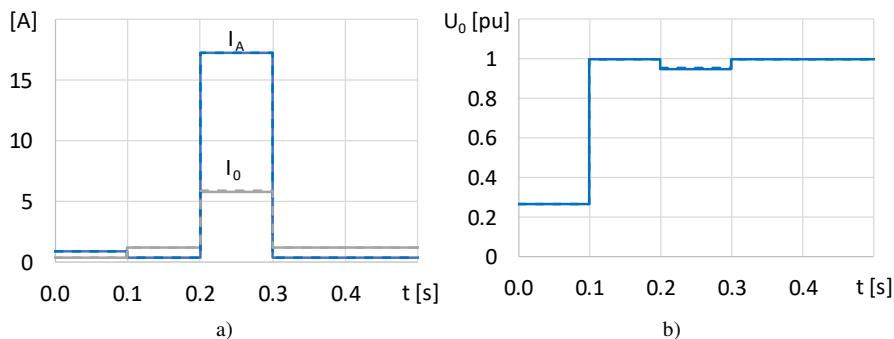


Figure 8

Simulation results of the ASCAT system operation during the earth fault: a) phase A line current  $I_A$  and zero sequence current  $I_0$ , b) ASC voltage  $U_0$ ; solid lines – MODES, dashed lines – OpenDSS

In the moment of the earth fault occurrence (0.1 s), the ASC voltage  $U_0$  increases to the nominal phase voltage (1 p.u.). Auxiliary shunt resistor connection at  $t = 0.2$  s leads to a drop in voltage – a certain ASC detuning. This is much more evident in the phase current  $I_A$  of the line, which is significantly increased as well as its zero-sequence component  $I_0$ , which exceeds the value of 5 A. The directional earth fault protection (ANSI 67N) with the threshold of 4 A detects the fault and issues a message. This message will help with fault localization (faulted branch is identified).

### 3.2.4 Shunting System

The last simulation done on this test system was the demonstration of shunting system. In this last case, both lines V2 and V3 are in operation and ASC is tuned to the resonance ( $X_{SC} = 1800 \Omega$ ). A resistance earth fault (with fault resistance of  $500 \Omega$ ) is applied at the end of the line V3 at  $t = 0.1$  s. The ASCAT actions are

noticeable from the Figure 9, showing the same variables as in previous case and also the simulation validation results from OpenDSS simulation tool; results are almost the same again and they are overlapping in Figure 9.

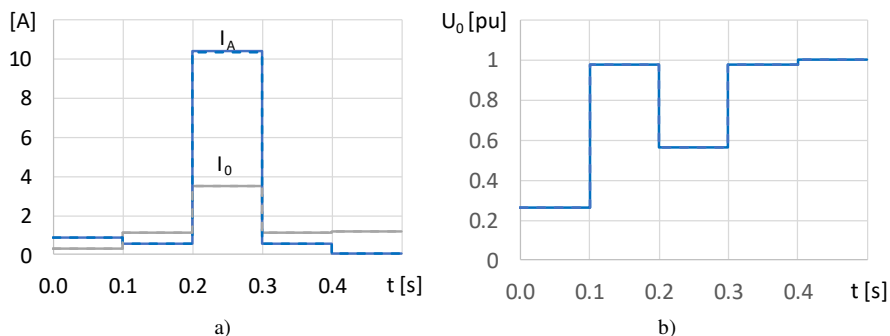


Figure 9

Simulation results of the ASCAT system operation, equipped with shunting system, during the earth fault: a) phase A line current  $I_A$  and zero sequence current  $I_0$ , b) ASC voltage  $U_0$ ; solid lines – MODES, dashed lines – OpenDSS

Earth fault occurrence at  $t = 0.1$  s leads to the increase of voltage  $U_0$  close to the nominal value (1 p.u.), connection of auxiliary shunt resistor at  $t = 0.2$  s for a limited period of time (0.1 s) means an increase of the phase current  $I_A$  of the line, which is slightly smaller than in the previous case. The zero-sequence component of the current is lower than the set threshold of 4 A, so the directional earth fault relay does not detect the fault. At time  $t = 0.4$  s, the affected phase is earthed in the substation through a resistance of 11  $\Omega$ . The fault is thus transmitted to the substation from its actual location, and the fault current  $I_A$  drops to zero. The power system should be still treated as faulted, but moving the fault to the substation minimizes the risks in the fault location (e.g., the arc should extinguish).

### 3.2.5 Summary

The three previous cases demonstrated the use of the newly built asymmetric model for MV distribution system analysis. The possibility to model the asymmetry of power lines and also the shunt conductance, which significantly affects the results (it is impossible to tune the ASC if all lines are entirely symmetrical), is of importance. A complex model of ASCAT system as well as a protection model were implemented in MODES. Presented cases are really simple and deals with the most common fault in the distribution system, which is the earth fault, thus, they are suitable also for education purposes. Results were validated using analytical calculations and OpenDSS simulation tool.

### 3.3 Voltage Unbalance Calculation

One of the causes of asymmetry in power system is the load unbalance caused by uneven distribution of loads over phases. This phenomenon is known especially on lower voltage levels (LV and MV), where some consumers and prosumers have only single-phase connection. However, it is also a problem of AC single-phase railway traction feeders, connected to the HV distribution system [14]. In this case, the use of created three-phase system model for voltage unbalance calculation caused by the railway traction feeders (V-connected) is demonstrated.

#### 3.3.1 Test System Description

For voltage unbalance calculation, modified test system depicted in Figure 10 was used. It is a part of the eight-node network published in [8].

The network was assumed to be balanced, except for loads in buses 7 and 8. These loads are the traction feeders 25 kV, fed from the 220 kV grid through the V-connection (open delta) transformers, according to Figure 2.

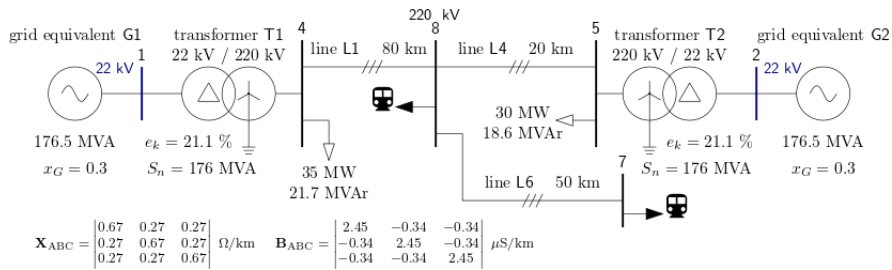


Figure 10

Single-line diagram of the test system for voltage unbalance calculation

#### 3.3.2 Voltage Unbalance Caused by the Train Operation

For voltage unbalance calculation, two scenarios were considered. The first one was the load consumption of  $P = 6$  MW in bus 8, caused by the train operation in the railway segment fed from the transformer T2 in bus 8. The second scenario was the consumption of  $P = 6$  MW in both buses 7 and 8, caused by the train operation in the railway segment fed from transformers T2 connected to these two buses.

It is assumed that the transformer connection at node 8 corresponds to substation 1 in the Figure 2, and the transformer connection at node 7 corresponds to substation 2. The values of power consumption of traction transformers supplied from the 220 kV network can be derived using the relations (9) and (10), the simplifying assumption of symmetrical phase voltages and neglecting reactance  $X$  in the relation (10). Phase values of these powers are  $\underline{S}_A = (3 + j1.73)$  MVA,  $\underline{S}_B = (3 - j1.73)$  MVA,  $\underline{S}_C = 0$  for both nodes. It is worth noting that although the locomotive takes only active power  $P$ , reactive power also flows in the network, causing voltage drops and losses.

When we know the power consumption in the individual phases, we can calculate the voltage asymmetry these consumptions will cause in the 220 kV network. A measure of asymmetry is the negative sequence voltage component. This value for the test system and defined two cases was calculated using the newly implemented network model in MODES; the results in per unit are given in Table 1. In both cases, positive sequence voltage value was almost 1 p.u. Validation calculation was done in PSCAD/EMTDC, results of validation are given also in Table 1 and they are almost the same.

Table 1  
Calculated values of negative sequence voltage

Simulation case	Negative sequence voltage in p.u.			
	Bus 7		Bus 8	
	MODES	PSCAD	MODES	PSCAD
1. – load of 6 MW in bus 8	0.01	0.01	0.01	0.01
2. – load of 6 MW in buses 7 and 8	0.023	0.023	0.0204	0.0201

Results in Table 1 are of interest. The standard EN 50160 [15] gives the admissible value of negative sequence voltage to be 0–2% of positive sequence voltage as the criterion for voltage unbalance. The requirement of EN 50160 is thus not fulfilled in the second case (negative sequence voltage reaches 2.3% and 2.04% respectively).

### 3.3.3 Summary

The chapter shows the use of the three-phase model for the evaluation of voltage unbalance caused by power consumption of traction feeders. The model makes possible to check whether the voltage unbalance does not exceed the limit defined in the standard EN 50160. Results were validated using PSCAD/EMTDC tool.

## 4 General Summary and Future Work

Two general concepts for simulation of three phase power system respecting the asymmetry are applicable, either the symmetrical components (positive, negative and zero sequence) or phase values (phase A, phase B, phase C). The choice of the concept is dependent on the problem being analyzed and to what extent the grid asymmetry needs to be respected.

Newly designed simulation model, implemented to MODES simulation tool and described in this article, can deal with both concepts – it allows data entering in phase values or symmetrical components. The computation method can be also selected as either symmetrical components or phase values. Criteria of selection are summarized in Table 2.

Comparing to other simulation tools, the newly designed three phase model implemented to MODES allows to simulate different fault-free and faulted operation of power system in RMS values, making the computation fast. It is using the MODES simulation engine, which has already implemented advanced protection and automation models. Existing models can be used also in newly build projects, dealing with unbalanced power systems. The asymmetric model is supposed to have various applications in the future, mainly in power system analysis, and additional models of network elements are being prepared. Currently, it is a source model representing single-phase connection of power sources, which is typical for LV networks. Such a model will allow to analyze problems related to prosumers or charging of electric vehicles.

Table 2  
Calculated values of negative sequence voltage

Computation method	Data entering	
	Symmetrical components	Phase values
Symmetrical components	Symmetrical both grid and load. Simulation of simple faults: single line to earth fault, line to line fault, double line to earth fault, single and double phase interruption.	Internal computation of parameters in symmetrical. Both grid and load are symmetrical. Simulation of simple faults: single line to earth fault, line to line fault, double line to earth fault, single and double phase interruption.
Phase values	Symmetrical both grid and load. Internal computation of parameters in phase values. Model allows to simulate also simultaneous faults including phase interruptions and single line to ground faults.	Neither grid nor load need to be symmetrical. It is e.g., possible to simulate the tuning of ASC. Model allows to simulate also simultaneous faults including phase interruptions and single line to ground faults.

## Conclusions

This work shows the process for the creation of a computational tool, allowing calculation of load flow problems, short circuit currents and transient stability assessment using phase values. The MODES simulation tool, newly extended by the asymmetric model, can deal with the grid unbalance, in both initial (fault-free) stage and also those occurring in the grid, due to unbalanced faults, comprising simultaneous faults.

Applications of the model were demonstrated using 3 selected problems from power systems operations – simultaneous faults, operation of arc suppression coil automatic tracking with earth fault protection and assessment of voltage unbalance caused by traction feeders. Results were validated by both analytical calculations and simulations using other tools. Simulation model implemented to MODES is

robust, allowing the analysis of power systems – especially distribution systems – under both fault-free and faulted operation. MODES is supposed to be used for analysis of different phenomena and also topical issues, such as, spread of distributed sources in the power system, in the future. Last but not least, it can be used for educational purposes, to demonstrate selected phenomena, in the grids, for the training of university students. The MODES tool usage is convenient and intuitive, thanks to the graphical user interface.

### **Acknowledgement**

This research work has been carried out in the Centre for Research and Utilization of Renewable Energy (CVVOZE). Authors gratefully acknowledge financial support from the Ministry of Education, Youth and Sports of the Czech Republic under BUT specific research program (grant number FEKT-S-23-8403).

### **References**

- [1] Máslo, K., Kolcun, M.: Simulation engine for dispatcher training and engineering network simulators, Proc IFAC CIGRE/CIRED Workshop on Control of Transmission and Distribution Smart Grids (CTDSG'16), Oct. 2016, pp. 395-399
- [2] Chladová, M., Máslo, K., Křištof, V.: Short circuit calculations and Dynamic stability assessment within dispatch control environment, operational requirements and SW reality, Proc. 10<sup>th</sup> International Scientific Symposium on Electric Power Engineering, Sept. 2019
- [3] Anderson, P. M.: Analysis of faulted power systems, Wiley-IEEE Press, 1995
- [4] Kersting, W. H.: Distribution System Modelling and Analysis, Third Edition, ISBN 978-1-4398-5622-2, CRC Press, 2012
- [5] Coppo, M., Bignucolo, F., Turri, R.: Generalised transformer modelling for power flow calculation in multi-phase unbalanced networks. IET Gener. Transm. Distrib. 2017, 11: 3843-3852. doi: 10.1049/iet-gtd.2016.2080
- [6] IEC TR 60909-4:2000 – Short-circuit currents in three-phase a.c. systems – Part 4: Examples for the calculation of short-circuit currents, 2000
- [7] Chen, B. K., Guo, B. S.: Three phase models of specially connected transformers, IEEE Trans. Power Delivery, Vol. 11, pp. 323-330, Jan. 1996
- [8] Roy L., Rao N. D.: Exact calculation of simultaneous faults involving open-conductors and line-to-ground short circuits on inherently unbalanced power system, IEEE Trans. Power App. Syst., Vol. 101, No.8, pp. 2738-2746, Aug. 1982
- [9] Koudelka, J., Topolanek, D., Toman, P., Fabian, M.: Analysis of Fault Condition Caused by Phase Interruption of HV Overhead Line, CIRED 2021

- The 26<sup>th</sup> International Conference and Exhibition on Electricity Distribution, 2021, pp. 1572-1576, doi: 10.1049/icp.2021.1720
- [10] Trojánek, Z., Chladová, M.: Transients in electrical power systems (Přechodné jevy v ES; In Czech), CTU publishing house, 1988, p. 145
- [11] Topolanek, D., Lehtonen, M., Toman, P., Orsagova, J., Drapela, J.: An earth fault location method based on negative sequence voltage changes at low voltage side of distribution transformers, *Int J Electr Power Energy Syst* 2020;118: 105768, doi: 10.1016/j.ijepes.2019.105768
- [12] Kouba, D., Procházka, K.: The Analysis of Efficiency of Shunt Resistor During a Single-phase Earth Fault Using the Two-port Network Theory, *Proc.of Conference CIRED*, 2013, pp. 1-4, doi: 10.1049/CP.2013.1066
- [13] Topolánek, D., Toman, P., Orságová, J., Dvořák, J.: The Method of the Additional Earthing of the Affected Phase During an Earth Fault and Its Influence on MV Network Safety, *Proc. of the IEEE PowerTech 2011*, pp. 1-8
- [14] Bayliss, C. R., Hardy, B. J.: *Transmission and Distribution Electrical Engineering*, Elsevier, 2012, doi: 10.1016/C2009-0-64342-7
- [15] EN 50160:2010 – Voltage characteristics of electricity supplied by public electricity networks, CENELEC, 2010

# Dielectric Relaxation Spectroscopy of Modern Hybrid Insulation Systems

**Peter Havran<sup>1</sup>, Roman Cimbala<sup>1</sup>, Samuel Bucko<sup>1</sup>, Juraj Kurimský<sup>1</sup>, Bystrík Dolník<sup>1</sup>, Michal Rajňák<sup>1,2</sup>, Jozef Király<sup>1</sup>, Katarína Paulovičová<sup>2</sup>**

<sup>1</sup>Faculty of Electrical Engineering and Informatics, Technical University of Košice, Letná 9, 04200 Košice, Slovakia; peter.havran@tuke.sk; roman.cimbala@tuke.sk; samuel.bucko@tuke.sk; juraj.kurimsky@tuke.sk; bystrik.dolnik@tuke.sk; michal.rajnak@tuke.sk; jozef.kiraly@tuke.sk

<sup>2</sup>Institute of Experimental Physics SAS, Watsonová 47, 04001 Košice, Slovakia; rajnak@saske.sk; paulovic@saske.sk

---

*Abstract: The constant optimization of the properties of insulating materials, is currently highly topical, at a global scale, as it directly concerns the efficiency of the operation of electrical equipment. This study includes research on modern insulation systems based on hybrid and non-hybrid nanofluid-paper. Cellulose insulation is impregnated with Shell Diala S4 ZX-1 transformer oil, enriched with two types of Fe<sub>3</sub>O<sub>4</sub> and C<sub>60</sub> nanoparticles, with varying nanoparticle concentrations. Samples of insulating materials are subjected to analysis using the method of dielectric relaxation spectroscopy in the frequency domain. The results point to electrophysical processes, of a conductive and polarizing nature. The increasing concentration of Fullerene nanoparticles, causes a decrease in dielectric losses and reduces the influence of interfacial polarization and electric double layer polarization in the hybrid nanofluid-paper system. The loss spectra of the complex electric modulus are the same as the spectra of the complex permittivity in the liquid-paper system. The Havriliak-Negami function reveals the dominance of polarization losses over conduction losses in the studied frequency spectrum and their origin when an external alternating electric field is applied.*

*Keywords: frequency domain; magnetic nanoparticle; fullerene nanoparticle; fluid-paper*

---

## 1 Introduction

Transformers in electricity system are one of key devices for a safe operation of the grid. There is a great danger of economic and material damages in case of their failure or damage [1] [2]. Therefore, it is necessary to keep the device in operation without overloads due to high powers, short circuits, etc. [3]. More frequent

overloads of transformers have a negative impact on their isolation system on which the lifetime of a transformer is dependent on. It is possible to detect an increasing trend in the degradation of the system in time by an appropriate monitoring of an isolation system using one of the diagnostic methods. The isolation system in transformers is composed of the combination of liquid and solid dielectric: insulating liquid and paper [4]. Another requirement for this system is also from the view of a heat convection which arises in the area of the transformer winding. Conventional insulating liquids include mineral oils, synthetic esters and natural esters. The latest requirements to increase the performance of transformers and to decrease their dimensions are a motivation for scientists and engineers to discover new approaches and methods in the field of insulating materials.

One of the ideas is to use the nm-sized particles which are freely dispersed in an insulating liquid. This method is able to increase the thermal conductivity of a particular liquid significantly and, as it is proved in certain studies, the liquid breaking strength [5]. Among the materials from the point of view of conductivity, both insulators and semi-conductive and conductive materials are used [6]. Since there is a strong magnetic field in the winding area, the usage of magnetic nanoliquids, where the paramagnetic nanoparticles are used, is considered. Given that the magnetization gradient is opposite to the magnetic field gradient, it is possible to create a natural circulation of a liquid in the transformer vessel [7].

In numerous studies,  $\text{Fe}_3\text{O}_4$  nanoparticles prepared by a chemical method have been used to create a magnetic liquid. Subsequently, a surfactant is applied to the surface of the nanoparticles formed in this way, which prevents the nanoparticles from joining each other in the carrier liquid. The more detailed procedure for the production of nanofluid with  $\text{Fe}_3\text{O}_4$  particles is described in [8].

Fullerene is another progressive material which has been used in experiments over last decade. This work was inspired by [9], where samples of nanofluids with  $\text{Fe}_3\text{O}_4$  nanoparticles with added fullerene were used.

Many of the mentioned studies which deal with electrical properties observe changes in properties only at the level of a liquid material. From the point of view of applicability, it is important to carry out also experiments in the presence of paper or cellulose products, which are a part of the entire insulation system.

## **2 Experiment**

### **2.1 Investigated Materials**

The experiment was carried out on samples of cellulose paper that were impregnated with samples of insulating nanofluids. The carrier-impregnating

substance consisted of modern Shell Diala S4 ZX-1 transformer oil. It is a base oil that is produced by converting natural gas into liquid hydrocarbons using GTL technology (Gas to Liquid). Natural gas continues in the production process by producing synthesis gas, which is subsequently transformed into crystal clear base oil with excellent properties through Fischer-Tropsch synthesis and refining. The progressivity of this oil points to zero sulfur content, which eliminates the risk of copper corrosion in power transformers and other significant properties include, higher thermal conductivity, higher oxidation stability and lower viscosity at low temperatures. Higher oxidation stability causes more excellent resistance of the oil to aging, which is accompanied by the higher formation of acids and oxidation processes. Suppressing these adverse factors with the acceptable properties of Shell Diala S4 ZX-1 oil helps extend cellulose insulation's life in power transformers [10] [11].

Six samples with different combinations of nanoparticle concentrations were prepared. Two types of nanoparticles were dispersed into the first three samples. Magnetic  $\text{Fe}_3\text{O}_4$  nanoparticles were precipitated from an aqueous solution of  $\text{Fe}^{2+}$  and  $\text{Fe}^{3+}$  ions with  $\text{NH}_4\text{OH}$  at  $81^\circ\text{C}$ . Subsequently, steric stabilization took place using one layer of oleic acid  $\text{C}_{18}\text{H}_{34}\text{O}_2$ . The second type of nanoparticle consisted of a spherical molecule of carbon  $\text{C}_{60}$  (Buckminsterfullerene) with triple-bonded atoms representing a closed structure. Purchased fullerene powder with a density of  $1600\text{ kg/m}^3$  was homogeneously dispersed in base oil without surfactant (surface-active substance). Finally, stabilized magnetic nanoparticles with a concentration of  $2.3\text{ \%w/V}$  were added to the first three samples with a concentration of fullerene nanoparticles of  $0.01\text{ \%w/V}$ ,  $0.02\text{ \%w/V}$ , and  $0.03\text{ \%w/V}$  (the ratio of the weight of the nanoparticles to the volume of the liquid). The given dispersion created a final concentration of magnetic nanoparticles of  $0.01\text{ \%w/V}$  in the investigated samples. These samples were mixed at  $60^\circ\text{C}$ , and we call them hybrid nanofluids (HIN, plus HIN-P paper). Other fluid samples are non-hybrid nanofluids (NIN, plus NIN-P paper). The fourth sample is enriched exclusively with fullerene nanoparticles with a concentration of  $0.01\text{ \%w/V}$  without surfactant. The fifth sample represents pure ferrofluid with a concentration of  $0.01\text{ \%w/V}$ , which represents comparison with the other samples due to the concentration of magnetic nanoparticles. The sixth sample consists of pure Shell Diala S4 ZX-1 transformer oil with a low density of  $786\text{ kg/m}^3$ . An overview of the investigated samples of hybrid and non-hybrid liquids, which fulfill the function of impregnation medium for cellulose insulation, is presented in Tab. 1. Impregnation of liquids and cellulose insulation took place in Petri dishes.

Table 1  
Samples of impregnation nanofluids

Sample	Concentration of fullerene nanoparticles C <sub>60</sub> (% w/V)	Concentration of magnetic nanoparticles Fe <sub>3</sub> O <sub>4</sub> (% w/V)
	without surfactant	with surfactant – oleic acid C <sub>18</sub> H <sub>34</sub> O <sub>2</sub>
1.	0.01	0.01
2.	0.02	0.01
3.	0.03	0.01
4.	0.01	0
5.	0	0.01
6.	0	0

## 2.2 Experimental Procedure

Samples of the insulation system hybrid nanofluid-paper and non-hybrid nanofluid-paper were investigated by the method of dielectric relaxation spectroscopy in the frequency domain. Dielectric relaxation spectroscopy is a non-destructive method that applies an electric field to a material to capture a small signal of the dielectric response in the form of dipole rotation and migration of free charges across the material. This modern method approximates the behavior of electrophysical parameters without the potential damage to the material caused by the application of high electric field intensities. Therefore, it is necessary to use professional measuring devices for the experimental procedure. The measurements of the samples examined by us were carried out using the IDAX 300 measuring device. This device applies an alternating electric voltage  $\underline{U}$  to the material with a changing frequency  $f$  from 0.1 mHz to 10 kHz. It measures the alternating electric current  $\underline{I}$  flowing through the material. From these input parameters, the measuring device calculates impedance  $\underline{Z}$ , from which several other electrophysical parameters are further expressed, such as, for example, electrical resistance  $\underline{R}$ , complex capacitance  $\underline{C}^*$ , dissipation factor  $\tan \delta$ , and electrical conductivity  $\underline{\sigma}$ . The output from the IDAX 300 meter was connected to a high-voltage and a low-voltage electrode. The electrode system consisted of Rogowski electrodes with a diameter of 54 mm, between which the tested hybrid and non-hybrid nano liquid-paper insulation system samples were inserted. The distance between the electrodes was 0.42 mm, representing the thickness of the cellulose insulation. The electrode system was placed in a shielded container, which was connected to the grounding of the measuring apparatus. Because wide-range frequencies were applied, the shielded container served as protection against electromagnetic frequencies from the outside environment. These unwanted frequencies could cause interference and deterioration of the quality of the measured data. To measure the samples, an alternating electric voltage of 100 V, was applied with the IDAX 300 measuring

device, which created an alternating electric field intensity of 238 kV/m at the given distance between the electrodes. The measuring apparatus is shown in Fig. 1.

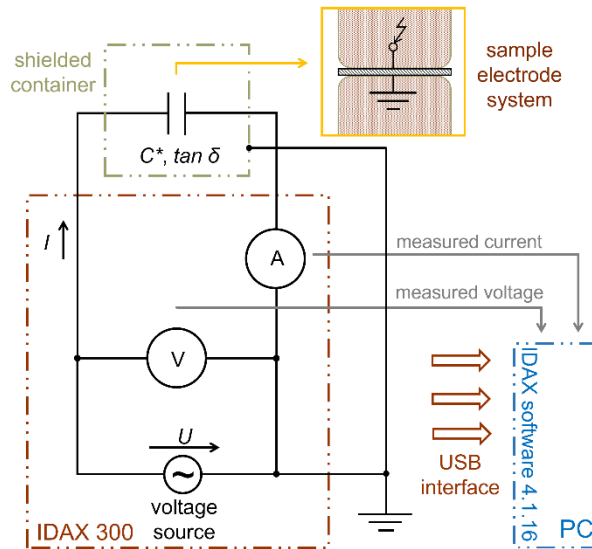


Figure 1  
Experimental setup

The experimental procedure was exposed in the laboratory to an air pressure of 1013hPa, an air humidity of 36%, and an air temperature of 21 °C. The research began with the assembly of the experimental setup, which was connected according to Fig. 1, and proceeded to measure the nanofluid-paper samples. Due to the higher intensity of the electric field, the frequency band was shortened to 1 mHz – 3 kHz because it was impossible to measure the frequency spectrum of 3 kHz – 10 kHz. The reason was decreased capacitive reactance and increased electric current, which loaded the voltage source in the IDAX 300 measuring device. The measuring device recorded the measured data of the capacitance  $C$  and the dissipation factor  $\tan \delta$  via a USB bus connected to a computer with the IDAX 4.1.16 software. Since electrophysical parameters such as capacitance  $C$  and dissipation factor  $\tan \delta$  are mostly applied in technical practice [12], for a more accurate description of dielectric behavior within the research area, these data were converted to complex permittivity  $\underline{\epsilon}^*$ , i.e., to its real  $\epsilon'$  and imaginary component  $\epsilon''$ . The reason for using complex permittivity to describe electrophysical processes was the modeling of relaxation and conduction mechanisms according to the characteristic response function, which reflected the parameters of the distribution of relaxation times. From recent studies, it was also found that the complex electric modulus  $\underline{M}^*$ , as the inverse value of the complex permittivity  $\underline{\epsilon}^*$ , can point out in detail the dynamics of the distribution of polarization processes by eliminating the conduction process that

is present in the low-frequency band [13]-[16]. Therefore, the complex electric modulus  $M^*$  and the complex permittivity  $\underline{\epsilon}^*$  will be used to analyze hybrid and non-hybrid nanofluid-paper samples.

### 3 Results and Discussion

The results of the experiment are analyzed in this section. We present the results of the complex permittivity, which will be accompanied by the results of the complex electric modulus for a comprehensive description of the investigated materials. In the third part of this chapter, electrophysical processes will be captured and analyzed through the distribution of relaxation times according to the Havriliak-Negami dielectric model.

#### 3.1 Complex Permittivity

The complex permittivity of samples of hybrid and non-hybrid nanofluids forming an insulating system together with cellulose paper is presented in this section. In Fig. 2, we present the real permittivity in the frequency band 1 mHz – 3 kHz. In the case of samples containing magnetic nanoparticles, a low-frequency dispersion is captured, which is attributed to at least one relaxation phenomenon. In higher frequencies, the real permittivity is stable at the value of 2.2 with a slight decrease. The exception is the 5. and 3. samples with a 1.07 times higher value, i.e., the sample with zero and the highest concentration of fullerene nanoparticles (0.03 %w/V). 6. the paper sample impregnated with pure GTL oil has the lowest real permittivity, moving at the value level of 2.2. The effect of fullerene nanoparticles is manifested by an increase in the real permittivity by a value of 0.04 in the entire frequency spectrum.

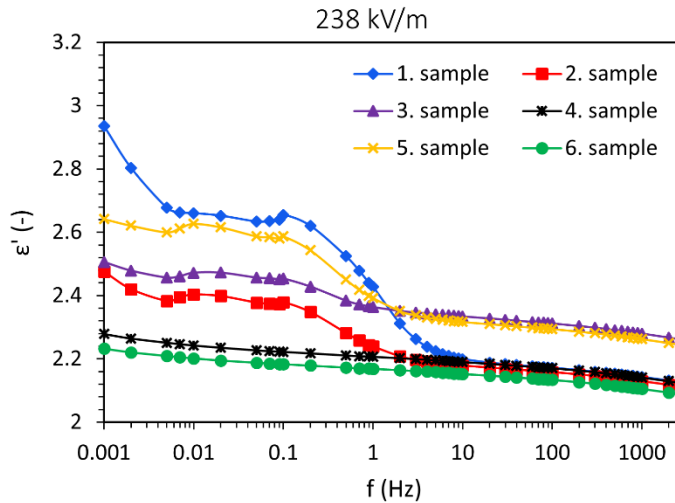


Figure 2

The frequency-dependent real permittivity  $\varepsilon'(f)$  of the investigated samples

In Fig. 3, we present the imaginary permittivity in the examined frequency band. As mentioned in the characteristics of real permittivity, samples containing magnetic nanoparticles show a clear dielectric relaxation in the low-frequency and medium-frequency bands, which confirms the imaginary permittivity spectrum. Samples 1, 2, 3, and 5, i.e., samples with magnetic nanoparticles, reflect a remarkable loss maximum in the band 0.1 Hz – 1 Hz, which subsequently changes to increasing dielectric losses again as the frequency decreases. Comparing the HIN-P samples, an inverse decrease of the relaxation maximum with increasing concentration of fullerenes can be seen. In addition to the reduction of the relaxation peak, the captured mechanism is shifted to lower frequencies. This exciting feature reduces dielectric losses at 50 Hz and 60 Hz operating frequencies, representing important information in applying the given insulation system. The samples without magnetic nanoparticles (4 and 6) do not show a relaxation maximum at a frequency of 1 Hz. However, their dielectric losses increase in the low-frequency band, similar to the other samples. The mentioned increase in dielectric losses can be caused by conduction losses manifested in the low-frequency band. The fullerene fraction in the GTL carrier oil in the fluid-paper system (4 sample) slightly increases the dielectric loss and the real permittivity compared to the oil-paper sample (6. sample).

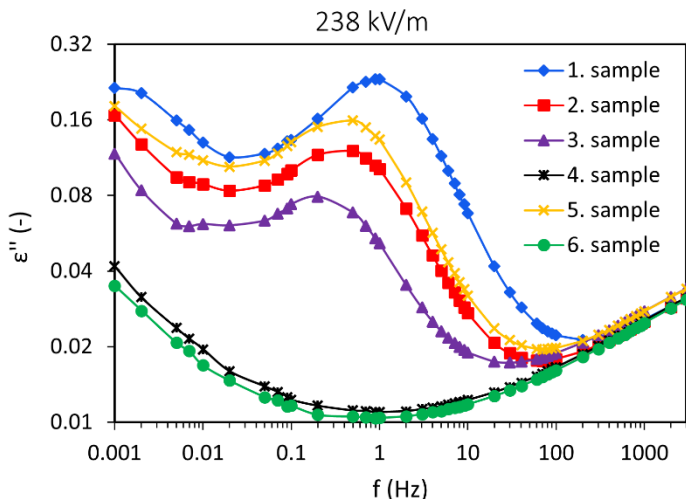


Figure 3

The frequency-dependent imaginary permittivity  $\underline{\varepsilon}''=f(f)$  of the investigated samples

The complex permittivity diagram in the complex plane is shown in Fig. 4. In the given display, the measured values of  $\underline{\varepsilon}''$  are plotted as a function of  $\underline{\varepsilon}'$  at different frequencies (1 mHz – 3 kHz). If the individual measured points in this diagram belong to a semicircle, then the given insulating system reacts to the external electric field with a relaxation response. In practice, very few materials exhibit a single polarization mechanism with a relaxation time, so that this fact can be attributed to the distribution of relaxation times. From plotting the complex permittivity to the complex plane, we can observe for samples with magnetic nanoparticles an indication of the development of the curves into a semicircle, which corresponds to the relaxation peaks of the imaginary permittivity. Samples without the magnetic nanoparticle fraction have V-shaped characteristics, while it is not known whether the low-frequency increase is caused by a relaxation or conduction process. We also encounter a similar dilemma with samples 2, 3, and 5. The HIN-P sample with the same concentration of fullerenes and magnetic nanoparticles 0.01 %w/V (1 sample) copies a certain imaginary semicircle in the low-frequency band, which would reflect the presence of a relaxation phenomenon. Based on the development of the measured permittivity spectra into a complex plane, it is not possible in our case to accurately characterize electrophysical processes at the molecular level. Because of this, the complex permittivity values were recalculated to the values of the complex electric modulus, as an inverse complex dielectric parameter.

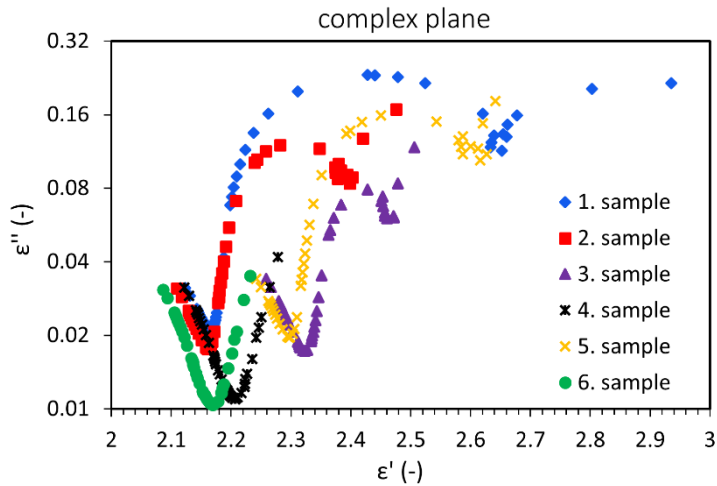


Figure 4

Complex permittivity in the complex plane  $\varepsilon''=f(\varepsilon')$

### 3.2 Complex Electric Modulus

The complex electric modulus is widely known due to its property of presenting the studied material without the influence of the conduction process and electrode polarization. These processes can affect the low-frequency spectrum of dielectric losses, which would distort the analysis of the measured data, presenting inaccurate identification of electrophysical processes in the low-frequency range. Some electrotechnical equipment, working on the principle of direct current, shows a failure rate based on the failure of the insulation system. Therefore, it is necessary to accurately identify electrophysical processes in the low-frequency band with subsequent prediction or provide relevant information to improve the insulation system. Fig. 5 shows the frequency spectra of the real modulus. Compared with the real permittivity in Fig. 2, the exact shape of the characteristics can be seen, which are reversed. It is possible to proceed from the findings that were described in subsection 3.1.

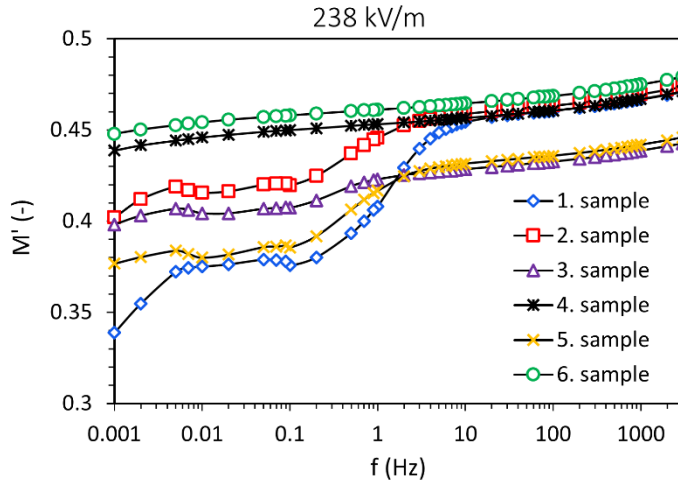


Figure 5

The frequency-dependent real modulus  $\underline{M}'=f(f)$  of the investigated samples

The complex electric modulus shows the dielectric behavior of the investigated materials exclusively from the point of view of relaxation processes. This means that it only provides the relaxation response of the investigated material, excluding the electrode polarization. Fig. 6 represents an insight into the loss spectra of a complex electric modulus. When comparing the frequency dependences of  $\underline{\varepsilon}''$  and  $\underline{M}''$  of liquid insulation (oils, nanofluids),  $\underline{M}''$  has a shifted relaxation mechanism to the band of higher frequencies [8] [13]. From Fig. 3 and Fig. 6, it can be seen that the dielectric loss characteristics are the same, and there is no shift of the polarization peaks to the band of higher frequencies at  $\underline{M}''$ . The fluid-paper insulation system does not change the dielectric response, which is presented by two parameters. It follows that the imaginary modulus for the fluid-paper system does not reveal polarization processes that were not recorded by the imaginary permittivity. Based on this, we find that the investigated frequency band is dominated by relaxation mechanisms and conduction losses suppressed by the losses of the relevant relaxation processes.

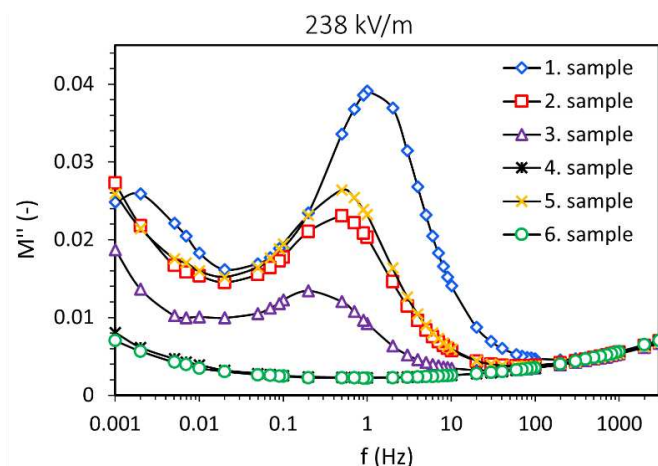


Figure 6

The frequency-dependent imaginary modulus  $M''=f(f)$  of the investigated samples

### 3.3 Havriliak-Negami Plots

In subsections 3.1 and 3.2, the examined samples were subjected to complex permittivity and complex electric modulus analysis. The results indicate that polarization losses in the low-frequency band could suppress conduction losses. Modeling electrophysical processes will verify the given statement with the Havriliak-Negami function (hereinafter referred to as "H-N"). Based on this dielectric model, the conduction and polarization losses are described by the relations:

$$\varepsilon''_{DC}(\omega) = \frac{\sigma_{DC}}{i\omega\varepsilon_0} \quad (1)$$

$$\varepsilon''_p(\omega) = +Im\left\{\varepsilon_\infty + \frac{\varepsilon_s - \varepsilon_\infty}{[1 + (i\omega\tau)^\alpha]^\beta}\right\} \quad (2)$$

considering that  $\sigma_{DC}$  represents the direct electrical conductivity,  $\omega$  is the angular frequency,  $\varepsilon_0$  is the vacuum permittivity,  $\varepsilon_s$  is the static or low-frequency permittivity ( $\varepsilon' \rightarrow 0$ ),  $\varepsilon_\infty$  is the optical or high-frequency permittivity ( $\varepsilon' \rightarrow \infty$ ),  $\tau$  represents the time relaxations of the polarization process and  $\alpha$  and  $\beta$  are empirical parameters describing the degree of distribution of relaxation times [17]. Fig. 7 shows the modeled curve of the 1. sample according to the H-N function. Modeling with approximation to the measured characteristic was performed with a deviation of 2.52%. The modeled characteristic is the sum of individual polarization losses  $\varepsilon''_{px}$  and conduction losses  $\varepsilon''_{DC}$ . The modeled spectra prove that the polarization process is more dominant in the low-frequency band than in the conduction process.

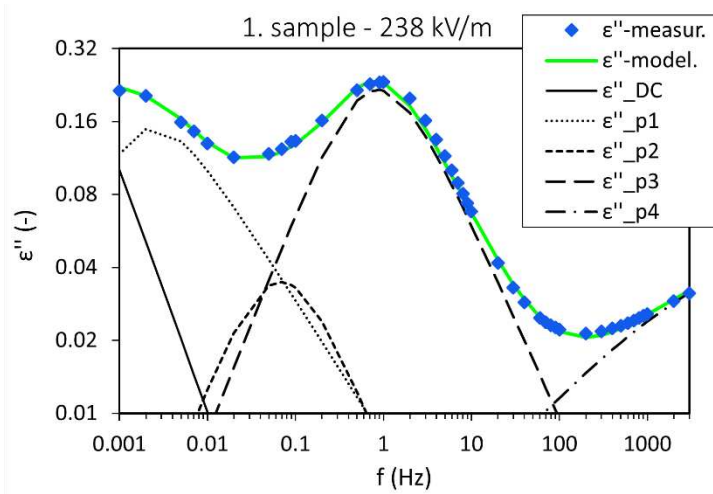


Figure 7

Modeling of electrophysical processes occurring in the 1. sample

The HIN-P insulation system responds to an applied electric field in the frequency band 1 mHz – 3 kHz by the presence of four polarization processes and a conduction process that is suppressed by relaxation losses. The polarization losses  $\varepsilon''_{p1}$  at a frequency of 2 mHz could be caused by the polarization of the space charge when applying a relatively high intensity alternating electric field. We estimate that the mentioned relaxation is not related to the fraction of  $\text{Fe}_3\text{O}_4$  and  $\text{C}_{60}$  nanoparticles because the 6. sample without these nanoparticles shows a remarkable increase in dielectric losses in the low-frequency region (Fig. 12). The polarization process causes the contribution of dielectric losses  $\varepsilon''_{p2}$  at a frequency of 0.07 Hz. From Fig. 3 and Fig. 6, we see that the origin of the given relaxation is related to magnetic nanoparticles. Thus, it can be an interfacial polarization at the magnetic nanoparticle-oil interface. All investigated samples with a concentration of magnetic nanoparticles (HIN-P and 5. sample) show similar behavior with this polarization at a frequency of 0.07 Hz. Fullerene nanoparticles do not cause this process because the 5. sample without these nanoparticles supports the occurrence of  $\varepsilon''_{p2}$  polarization losses (Fig. 11). Another proof is the characteristic of the 4. sample without magnetic nanoparticles (with  $\text{C}_{60}$  0.01 %w/V), which has no  $\varepsilon''_{p2}$  contribution (Fig. 10). The most significant influence of polarization losses on the dielectric response is present around the frequency of 1 Hz. The polarization losses  $\varepsilon''_{p3}$  are related to the electric double layer polarization that occurs in ferrofluids at frequencies close to 1 Hz [8] [12] [18-20]. Magnetic nanoparticles are stabilized by a surfactant whose head is polar, creating a negatively charged particle. This system forms the first electrical layer that electrostatically attracts the positive ions present in the nanofluid. This mechanism supports the formation of a second electric layer on the nanoparticle's surface, which polarizes the system under an applied electric

field. By increasing the frequency, further increase of polarization losses in the band 100 Hz – 3 kHz is investigated. The contribution  $\epsilon''_{p4}$  causes interfacial fluid-paper polarization. This is confirmed by the finding from Fig. 3 and Fig. 6, which reveals a high-frequency increase in dielectric loss for every sample investigated, even for (6 sample) (NIN-P) without magnetic and fullerene nanoparticles. The individual relaxation parameters involved in modeling the H-N function are listed in Tab. 2.

Fig. 8 shows the modeling of electrophysical processes of the 2. HIN-P sample. We state that the deviation of the modeled characteristic from the measured characteristic is equal to 3.3%. The lower the deviation, the more accurate the values of the modeling parameters of the characteristic  $\epsilon''_{model}$ , given in Tab. 2. The (2 sample) differs from the (1 sample) in the increased concentration of fullerene nanoparticles by 0.01 %w/V ( $C_{60} = 0.02$  %w/V). With this sample, we capture the same types of electrophysical processes as in Fig. 7.

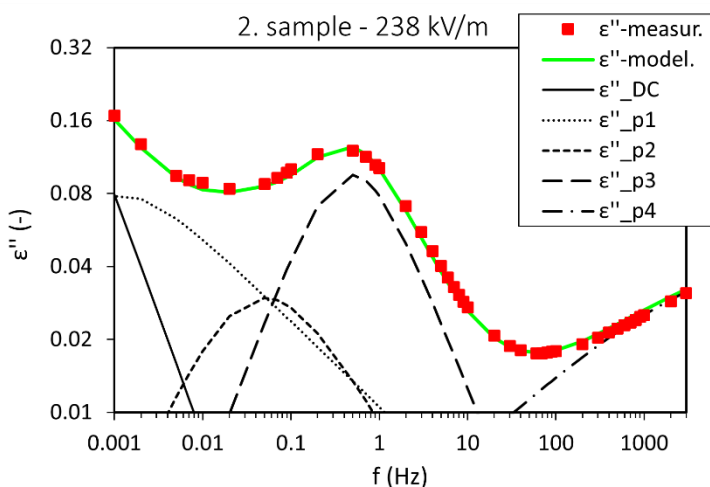


Figure 8

Modeling of electrophysical processes occurring in the 2. sample

Modeling of electrophysical processes of the 3. sample HIN-P is shown in Fig. 9. We note that the deviation of the modeled curve from the measured curve is equal to 2.63%. Similarly, as with samples 1 and 2, the same types of electrophysical processes are present. The difference is that the increase in the concentration of fullerene nanoparticles in HIN-P limits the contributions of  $\epsilon''_{p1}$ ,  $\epsilon''_{p2}$ , and  $\epsilon''_{p3}$ , thereby reducing the dielectric losses and shifting these contributions to lower frequencies. Dielectric losses are also reduced at operating frequencies of 50 Hz and 60 Hz, which is a remarkable feature in the potential application of these samples.

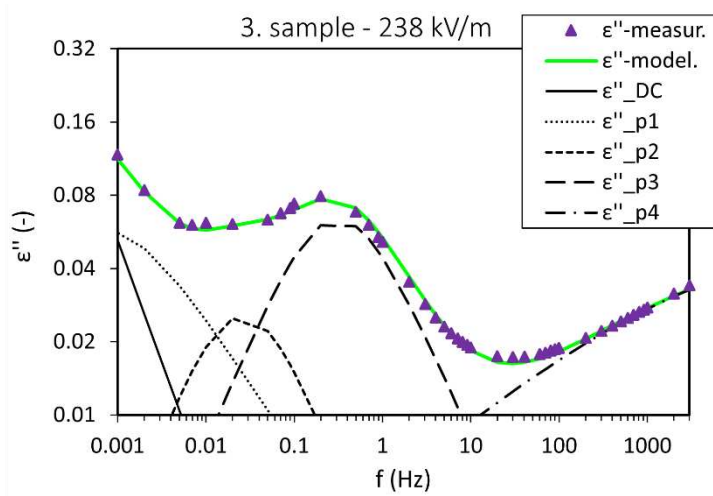


Figure 9

Modeling of electrophysical processes occurring in the 3. sample

In Fig. 10, we show the modeling of electrophysical processes of the (4 sample) NIN-P, which has only the fullerene fraction. We state that the deviation of the modeled characteristic from the measured characteristic is equal to 2.64%. This sample does not show the contributions of polarization losses  $\epsilon''_{p2}$  and  $\epsilon''_{p3}$  because it does not contain magnetic nanoparticles, like samples HIN-P and (5 sample). We register only space charge polarization and fluid-paper interfacial polarization. The parameter values are recorded in Tab. 2.

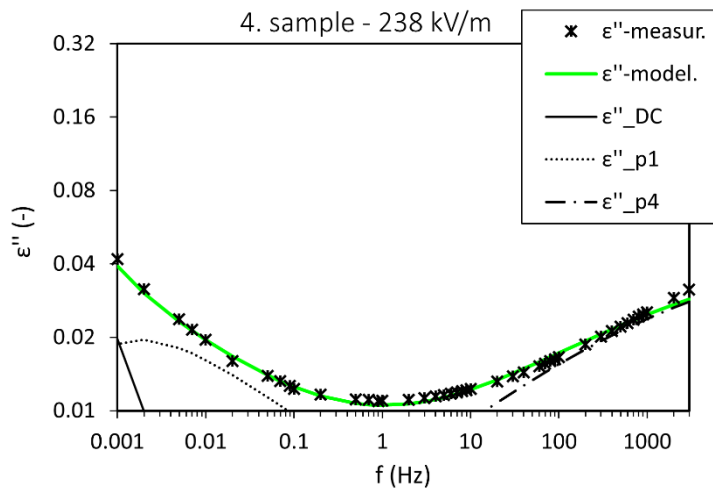


Figure 10

Modeling of electrophysical processes occurring in the 4. sample

Modeling of sample 5 NIN-P, which contains exclusively magnetic nanoparticles, is presented in Fig. 11. The occurrence of types of electrophysical processes is the same as for HIN-P samples. It is, therefore, evident that fullerene nanoparticles are not responsible for the contribution of polarization losses  $\varepsilon''_{p2}$  and  $\varepsilon''_{p3}$ , which would cause a reduction of their contributions with a shift in the frequency spectrum. The deviation of the modeled characteristic of sample 5, is at the level of 3.82%.

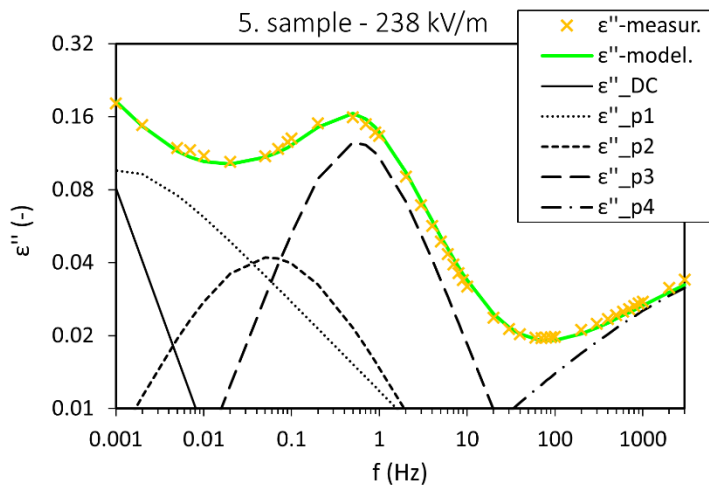


Figure 11

Modeling of electrophysical processes occurring in the 5. sample

Fig. 12 shows the modeled characteristics of the sample 6 NIN-P, which does not contain any concentration of nanoparticles. It consists exclusively of an oil-paper system. We note that the deviation of the modeled characteristic is equal to 3.69%. Similarly, as with sample 4, we do not register the contributions of polarization losses  $\varepsilon''_{p2}$  and  $\varepsilon''_{p3}$ . Sample 4, which differs from sample 6, with the presence of fullerene nanoparticles, shows an increase in the contribution of polarization losses  $\varepsilon''_{p1}$  and conduction losses  $\varepsilon''_{DC}$ . This is due to the fullerene fraction, which causes a higher conductivity of the material and a higher polarizability of the space charge in the low-frequency band of dielectric losses.

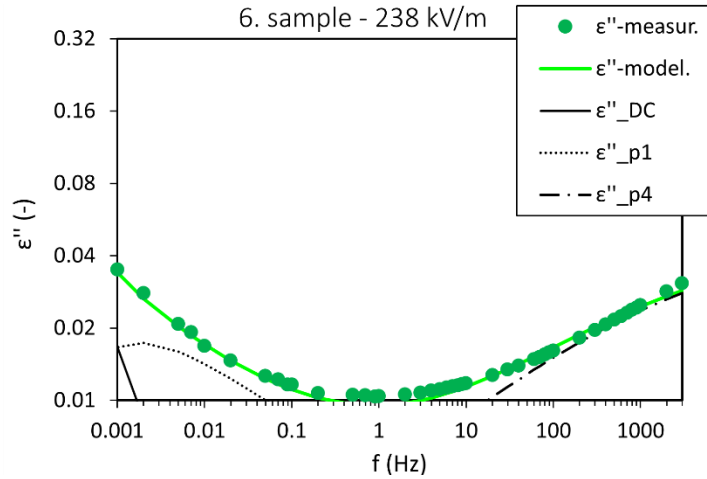


Figure 12

Modeling of electrophysical processes occurring in the 6. sample

As mentioned above in the text, Tab. 2 shows the parameter values of electrophysical process modeling of hybrid and non-hybrid nanofluid-paper insulation system samples using the H-N function. These parameters were modeled through equations (1) and (2). We note that the deviations mentioned above during modeling would slightly change the values of the individual parameters of the  $\epsilon''_{model}$  characteristic.

Table 2

Parameter values of modeling electrophysical processes through the H-N function

sample	parameter	p1	p2	p3	p4
1.	$\epsilon_s$ (-)	3.06	2.65	2.69	2.16
	$\epsilon_\infty$ (-)	2.65	2.57	2.17	1.512
	$\alpha$ (-)	0.96	0.925	0.921	0.412
	$\beta$ (-)	0.6	0.95	0.881	0.201
	$\tau$ (s)	100.2	2.449	0.205	0.000022
2.	$\epsilon_s$ (-)	2.65	2.67	2.35	2.3
	$\epsilon_\infty$ (-)	2.36	2.58	2.14	1.65
	$\alpha$ (-)	0.91	0.8	0.95	0.36
	$\beta$ (-)	0.39	0.79	0.96	0.23
	$\tau$ (s)	301.4	4.123	0.338	0.000022
3.	$\epsilon_s$ (-)	2.55	2.64	2.525	2.39
	$\epsilon_\infty$ (-)	2.37	2.58	2.365	1.59
	$\alpha$ (-)	0.81	0.91	0.87	0.31
	$\beta$ (-)	0.69	0.96	0.95	0.22
	$\tau$ (s)	312.5	6.373	0.538	0.000022

4.	$\varepsilon_s$ (-)	2.305	-	-	2.21
	$\varepsilon_\infty$ (-)	2.21	-	-	1.64
	$\alpha$ (-)	0.81	-	-	0.29
	$\beta$ (-)	0.31	-	-	0.29
	$\tau$ (s)	305.8	-	-	0.000022
5.	$\varepsilon_s$ (-)	2.72	2.72	2.61	2.3
	$\varepsilon_\infty$ (-)	2.37	2.58	2.33	1.65
	$\alpha$ (-)	0.9	0.7	0.94	0.36
	$\beta$ (-)	0.41	0.95	0.97	0.23
	$\tau$ (s)	301.6	3.154	0.304	0.000022
6.	$\varepsilon_s$ (-)	2.303	-	-	2.21
	$\varepsilon_\infty$ (-)	2.22	-	-	1.64
	$\alpha$ (-)	0.85	-	-	0.3
	$\beta$ (-)	0.29	-	-	0.28
	$\tau$ (s)	306.2	-	-	0.000022

## Conclusions

This study analyzed modern insulating materials based on the fluid-paper system. Hybrid and non-hybrid insulation systems were studied using the dielectric relaxation spectroscopy method in the frequency domain. These are unique results in the diagnostics of insulation materials for high-voltage applications, as samples of hybrid and non-hybrid nanofluids with different types and combinations of nanoparticles that formed a single unit with cellulose insulation were investigated and compared. Such materials are not sufficiently researched; therefore, the added value of this publication is precisely the research of the given modern insulation system. Frequency-dependent dielectric spectroscopy showed that dielectric losses in hybrid insulation systems could be reduced by increasing the concentration of fullerene nanoparticles. Increasing fullerene nanoparticles limited the contributions of relaxation processes such as interfacial polarization at the magnetic nanoparticle-fluid interface and electric double layer polarization. The presence of electrical double layer polarization was responsible for increasing dielectric losses at industrial frequencies of 50Hz and 60Hz. Therefore, the stated finding is sympathetic to the potential application of the studied samples in practice. In the opposite case, in the non-hybrid nanofluid-paper system, there was an increase in dielectric losses at the concentration of fullerene nanoparticles with a fraction of 0.01 %w/V, mainly in the low-frequency band.

This study also showed that the complex electric modulus in the fluid-paper system does not shift the relaxation information to higher frequencies compared to the complex permittivity. Their dielectric responses ranged at the same frequencies. Therefore, it is possible to analyze these systems with one complex parameter and use the modeling of electrophysical processes through the Havriliak-Negami function. Based on this function, the parameter values of individual electrophysical

processes, which make up the frequency spectrum of the studied modern materials, were revealed. The liquid-paper insulating system with a concentration of magnetic nanoparticles exhibits four polarization processes and one conduction process in the frequency spectrum of 1 MHz – 3 kHz. The examined frequency spectrum of samples without magnetic nanoparticles contains two polarization processes and one conduction process. Individual types of polarization processes were presented in the results of this study. This work also provides a springboard for continuing research into these modern insulation systems. It is necessary to experimentally verify the behavior of these materials under various degradation factors and through several diagnostic methods for a comprehensive description of changes in the electrophysical structure of the given modern material. Dielectric relaxation response in the frequency band at the operating temperatures of the power transformer, with the application of these temperatures in a specific time horizon, would be no less important information concerning the insulating state of these materials.

### **Acknowledgement**

This research was funded by the Ministry of Education, Youth and Sports within the project VEGA 2/0011/20 and 1/0154/21 and the Slovak Agency for Research and Development based on contracts no. APVV-15-0438, APVV-17-0372, and APVV-18-0160.

### **References**

- [1] H. Hu *et al.*: Association rule mining from failure analysis test reports of transformers, The 16<sup>th</sup> IET International Conference on AC and DC Power Transmission (ACDC 2020), 2020, pp. 2101-2105
- [2] O. Kulakov, A. Katunin, M. Kustov, E. Slepuzhnikov and S. Rudakov: Investigation of Reliability of Emergency Shutdown of Consumers in Electric Power Systems of Explosive Hazardous Zones, 2022 IEEE 3<sup>rd</sup> KhPI Week on Advanced Technology (KhPIWeek), 2022, pp. 1-5
- [3] Z. Čonka, V. Kohan, M. Kolcun, P. Judith and I. J. Rudas: Fault localization method using WAM systems, 2020 21<sup>st</sup> International Scientific Conference on Electric Power Engineering (EPE), 2020, pp. 1-4
- [4] IEEE Standard for Liquid-Immersed Transformers Designed to Operate at Temperatures Above Conventional Limits Using High- Temperature Insulation Systems - Redline, in IEEE Std C57.154-2022 (Revision of IEEE Std C57.154-2012) – Redline, 18 Aug. 2022, pp. 1-96
- [5] M. Rajňák, J. Kurimský, R. Cimbala, Z. Čonka, P. Bartko, M. Šuga, K. Paulovičová, J. Tóthová, M. Karpets, P. Kopčanský, M. Timko: Statistical analysis of AC dielectric breakdown in transformer oil-based magnetic nanofluids, *Journal of Molecular Liquids*, Vol. 309, July 2020, pp. 113243-1-7

- [6] M. Rafiq, M. Shafique, A. Azam, M. Ateeq: Transformer oil-based nanofluid: The application of nanomaterials on thermal, electrical and physicochemical properties of liquid insulation-A review, *Ain Shams Engineering Journal*, Vol. 12, 2021, pp. 555-576
- [7] S. S. Leong, Z. Ahmad and JK Lim: Magnetophoresis of superparamagnetic nanoparticles at low field gradient: hydrodynamic effect, *Soft Matter*, Vol. 11, 2015, pp. 6968-9680
- [8] R. Cimbala, P. Havran, J. Király, M. Rajňák, J. Kurimský, M. Šárpataky, B. Dolník, K. Paulovičová: Dielectric response of a hybrid nanofluid containing fullerene C<sub>60</sub> and iron oxide nanoparticles, *Journal of Molecular Liquids*, Vol. 359, May 2022, pp. 1-9
- [9] K. Paulovičová, J. Tóthová, M. Rajňák, M. Timko, P. Kopčanský, V. Lisý: Nanofluid Based on New Generation Transformer Oil: Synthesis and Flow Properties, *ACTA PHYSICA POLONICA A*, Vol. 137, May 2020, pp. 908-910
- [10] P. Havran, R. Cimbala, J. Kurimský, B. Dolník, I. Kolcunová, D. Medved', J. Király, V. Kohan, E. Šárpataky: Dielectric Properties of Electrical Insulating Liquids for High Voltage Electric Devices in a Time-Varying Electric Field, *Energies*, Vol. 15, 391, Jan. 2022, pp. 1-21
- [11] Shell Lubricants, Technical Paper, Available online: <file:///C:/Users/phavr/Downloads/diala-white-paper-low.pdf> (accessed on 24 September 2022)
- [12] M. Rajňák, J. Kurimský, B. Dolník, P. Kopčanský, N. Tomašovičová, E. A. Taculescu-Moaca, M. Timko: Dielectric-spectroscopy approach to ferrofluid nanoparticle clustering induced by an external electric field, *Physical Review E*, Vol. 90, Sept. 2014, pp. 032310-1-9
- [13] M. Wübbenhorst, J. Turnhout: Analysis of complex spectra. I. One-dimensional derivative techniques and three-dimensional modeling, *Journal of Non-Crystalline Solids*, Vol. 305, July 2002, pp. 40-49
- [14] L. Sheng-Tao, W. Hui, L. Chun-Jiang, L. Jian-Ying: Dielectric modulus response of CaCu<sub>3</sub>Ti<sub>4</sub>O<sub>12</sub> ceramic, *Acta Physica Sinica*, Vol. 62, Aug. 2013, pp. 087701-1-6
- [15] I. M. Ward: *Anelastic and dielectric effects in polymeric solids*, Wiley: New York and London, 1967
- [16] K. Yang, M. Dong, Y. Hu, J. Xie, M. Ren: The Application of Dielectric Modulus in the Oil-impregnated Paper Insulation, 2020 *Elect. Insul. Conf. (EIC)*, IEEE press, Knoxville TN USA, 05 Aug. 2020, pp. 103-106
- [17] J. Xie, M. Dong, Y. Hu, T. Zhuang, R. Albarracín-Sánchez, J.M. Rodríguez-Serna: Modeling Oil-paper Insulation Frequency Domain Spectroscopy

- Based on its Microscopic Dielectric Processes, *IEEE Transactions on Dielectrics and Electrical Insulation*, Vol. 26, Dec. 2019, pp. 1788-1796
- [18] R. P. Misra, S. Das, S. K. Mitra: Electric double layer force between charged surfaces: Effect of solvent polarization, *The Journal of Chemical Physics*, Vol. 138, Mar. 2013, pp. 114703
- [19] Š. Hardoň, J. Kúdelčík, M. Gutten: Dielectric Spectroscopy of Two Concentrations of Magnetic Nanoparticles in Oil-Based Ferrofluid, *Acta Physica Polonica A*, Vol. 137, May 2020, pp. 961-963
- [20] V. N. Shilov, A. V. Delgado, F. González-Caballero, J. Horno, J. J. López-García, C. Grosse: Polarization of the Electrical Double Layer. Time Evolution after Application of an Electric Field, *Journal of Colloid and Interface Science*, Vol. 232, Dec. 2000, pp. 141-148

# Investigation of Shielding Materials, for the Purpose of Shielding Electromagnetic Fields

**Ján Zbojovský, Marek Pavlík, Iraida Kolcunová, Juraj Kurimský, Roman Cimbala**

Technical University of Košice, Department of Electric Power Engineering,  
Mäsiarska 74, 040 01 Košice, Slovakia; jan.zbojovsky@tuke.sk,  
marek.pavlik@tuke.sk, iraida.kolcunova@tuke.sk, juraj.kurimsky@tuke.sk,  
roman.cimbala@tuke.sk

---

*Abstract: This paper deals with an investigation of the shielding effectiveness of shielding material HSF 54 and windows foil Profilon Antyspy. The motivation for this research was the ongoing need in the field, for improvement of shielding properties against electromagnetic fields. It is focused on the frequency range 0.8-9 GHz. Measurements were performed according to the IEEE 299-2006 Standard. The shielding coating was applied directly, on the MDF board, then measurements of shielding effectiveness and reflection of for all samples were performed in an anechoic chamber. The attenuation of the investigated samples was calculated from the measured values. Subsequently, the presence of spatial charge on the examined samples were measured in the anechoic chamber. It was found that all materials have shielding ability, to prevent the penetration of an electromagnetic field. The presence of spatial charge varies depending on the frequency of the electromagnetic field and its duration. It can be stated that it is necessary to ground each shielding coating, in order to avoid injury or destruction of electronic equipment.*

*Keywords: electromagnetic wave; frequency; absorption; reflection; shielding, spatial charge*

---

## 1 Introduction

In the past, electromagnetic radiation was an unknown topic for the lay public. With the dramatic increase of wireless technologies (mobile phones, Wi-Fi Internet, etc.), even the lay public is becoming increasingly interested in the issue. Mobile transmitters are placed on residential buildings, which can pose a threat from a possible radiation source. Currently, there are several options to protect against radiation from electrical equipment.

Limiting electromagnetic radiation is already possible during the design of electrical equipment. The manufacturer of the device must comply with standards for the emission of electromagnetic radiation. However, it is not possible to completely eliminate electromagnetic radiation. On the other hand, for the operation of mobile devices, it is not desirable that the signal be eliminated. In that case, the only way to prevent electromagnetic radiation is to use shielding. There are many studies in the world that focus on the health problems caused by excessive exposure to the electromagnetic field.

It is necessary to realize that a person is constantly exposed to an electromagnetic field. Up to 80% of a person's time is spent inside buildings - at work, at home while shopping, etc. Therefore, buildings can offer a natural shielding of materials against the effects of the electromagnetic field. In our papers [1-5] we investigated the shielding effectiveness of commonly available building materials. We investigated that even common building materials have a shielding ability. In the case of the polystyrene material, the shielding ability is minimal to none. In the case of brick, we observed the shielding effectiveness in the frequency range from 1 GHz to 9 GHz. It is also true that with the increasing thickness of the shielding material, the shielding ability of the material increases. The shielding ability of the material is defined by the shielding effectiveness *SE*. If it is necessary to increase the shielding effectiveness, it is possible to do the following:

- a) Change the thickness of the material - it is unrealistic for buildings
- b) Add additional material, for example, shielding coating, foil, etc.
- c) In this article, we focus on the use of a shielding coating and the use of a shielding foil.

## **2 Shielding Effectiveness of the Electromagnetic Field**

The shielding ability of the material can be defined by the shielding effectiveness of the electromagnetic field. Shielding effectiveness can be determined in two ways:

- a) According to IEEE 299-2006 Standard, Method for Measuring the Effectiveness of Electromagnetic Shielding Enclosures based on the measurement of shielding effectiveness. This measurement was performed in an anechoic chamber. The measurement consists of two steps – with and without shielding, and based on the difference between these values, we calculate the shielding effectiveness of the shielding. The IEEE Standard determines the calculation of the shielding effectiveness based on parameters - electric field intensity, magnetic field intensity, electromagnetic field power and electromagnetic field voltage.

- b) The shielding effectiveness can be calculated based on the relation (1), where  $A$  is the absorption of the electromagnetic field and  $R$  is the reflection of the electromagnetic field. If we know the parameters  $A$  and  $R$ , then the effectiveness of the shielding of the electromagnetic field is given by the sum of absorption and reflection of the electromagnetic field. The following figure (Fig.1) shows how the electromagnetic wave penetrates through the shielding material. It can be seen that part of the wave is reflected, part of the wave is absorbed by the shielding material and part of the wave passes through the material in the form of a transmitted wave. In practice, however, it is difficult to measure the absorption of the electromagnetic field because the absorption occurs inside the material. Therefore, the absorption of the electromagnetic field can be calculated from the shielding effectiveness and the reflection of the electromagnetic field. The  $SE$  and  $R$  parameters can be measured in an anechoic chamber based on the IEEE standard.

In this paper, we focused on the research of the shielding effectiveness of electromagnetic field and reflection for the above-mentioned shielding foils and coatings. In our measurements, the values of the electromagnetic field intensity were in dB, therefore the equation (2) was used to calculate the shielding effectiveness

$$SE=A+R \quad (1)$$

$$SE=P_1+P_2 \quad (2)$$

where  $P_1$  is the power of the electromagnetic field hitting on the shielding material and  $P_2$  is the power of the electromagnetic field behind the shielding material.

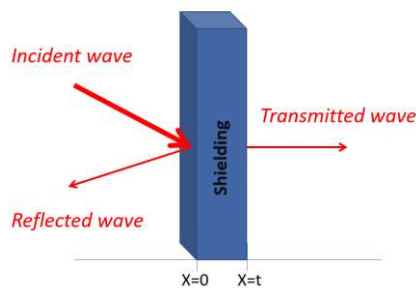


Figure 1

Propagation of the electromagnetic wave through the shielding material.

The second part of article was focused on the investigation of the formation of spatial charge on the examined samples.

### 3 Shielding Effectiveness Measuring Setup

As mentioned earlier, in this paper, we focus our research on the shielding effectiveness of electromagnetic fields, using different shielding materials. Three materials were used:

- a) Shielding material HSF 54
- b) Shielding foil 1 – for commercial use (Profilon Antyspy)
- c) Shielding foil 2 – for commercial use (Profilon Antyspy)

HSF 54 shielding coating is a universal electrically conductive coating used to shield low and high frequency electromagnetic radiation. It composed on the basis of carbon and high-quality acrylic binder. It is frost-resistant and this makes it a widely applicable coating for both interiors and exteriors. PROFILON AntiSpy window foil is a special security type of foil designed to block RF, IR, UV and solar energy. In addition, it is also intended for protection against electromagnetic interference (EMI). It is installed on the buildings or on window. According to the technical sheet, the shielding effectiveness of this foil ranges up to 33 dB (AS100) and up to 46 dB (AS260). During the measurement, we marked this foil as foil 1. We marked the second foil as foil 2.

The set of the measuring workplace consists of a receiving antenna, transmitting antenna, pulse generator and a spectrum analyzer. In the first step, the workplace was calibrated based on the telecommunications equation:

$$P_p = P_v - L_0 + G_v + G_p \quad (3)$$

where  $P_p$  is the received power,  $P_v$  is the transmitted power,  $L_0$  is the free space losses,  $G_v$  is the gain of the transmitting antenna and  $G_p$  is the gain of the receiving antenna [6-8].

The principal view of the arrangement of antennas is shown in Fig. 2. However, no shielding was placed between the antennas during calibration. We placed the receiving and transmitting antenna at a distance of 2 m from each other at the same height from the floor and turned the antennas as precisely as possible perpendicular to each other. After the successful calibration, we placed the shielding material - a wooden board and the shielding effectiveness was measured. The shielding effectiveness values were considered as reference values. This is because the coating and foils were placed on a wooden board. If the measurement without shielding was considered as the reference value, then the shielding effectiveness value of the wooden board would be included in the shielding effectiveness. Therefore, the values of the shielding effectiveness of the wooden board were subtracted from the values of the shielding effectiveness of the shielding materials. The measurement was performed in the frequency range from 0.8 GHz to 9 GHz with a step of 0.01 GHz.

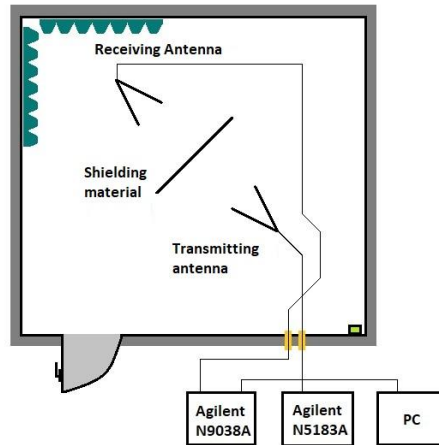


Figure 2

Experiment setup for measuring shielding effectiveness of electromagnetic field

When measuring the reflection of the electromagnetic field, the arrangement of the antennas inside the chamber is shown in Fig. 3. The arrangement was performed so that the antennas did not interfere with each other.

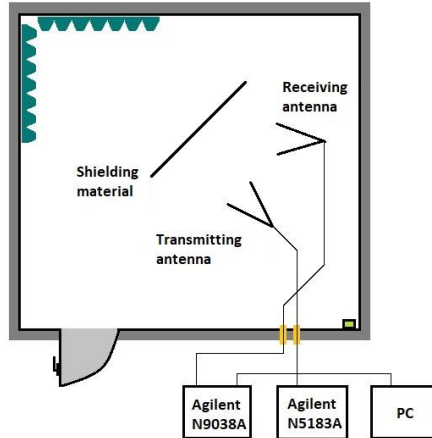


Figure 3

Experiment setup for measuring reflection of electromagnetic field

## 4 Experimental Results

### a) Shielding Effectiveness

As mentioned earlier, the measurement of shielding effectiveness is a comparative method where we compare the measurement without shielding and with shielding. After subtracting these two values, we have the value of the shielding effectiveness in the investigated frequency range.

Figure 4 shows the dependence of electromagnetic field shielding effectiveness for three shielding materials – shielding coating HSF 54, shielding foil 1 and shielding foil 2.

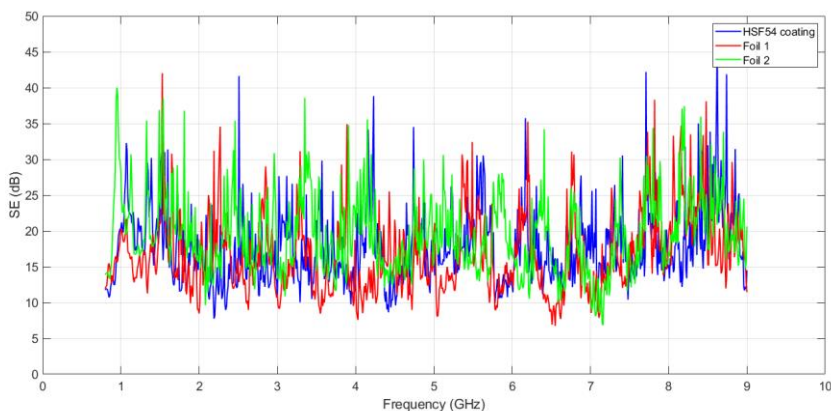


Figure 4

Shielding effectiveness in the frequency range from 0.9 GHz to 9 GHz

From the results, a similar shielding effect can be observed for all three shielding materials. The material "Foil 1" have the lowest values. The shielding effectiveness in the investigated frequency range reaches values from 10 dB to 30 dB. We do not observe a rising or falling trend in the monitored frequency range. All three shielding materials have approximately the same values in the whole measured range. In the research that we published in [1-5] the same was true for the material polystyrene. Also, no trend was observed. However, an increasing trend was observed in the investigated frequency range for the brick material. In addition, the shielding effectiveness reached low values in the first third of the observed frequency range. The highest shielding effectiveness values were achieved in the last third of the observed frequency range. However, for measuring of shielding effectiveness - HSF 54 shielding coating, shielding foil 1 and shielding foil 2 - this fact was not confirmed. It follows that all three materials are suitable for shielding the investigated frequency range and have a similar shielding effect.

## b) Reflection of Electromagnetic Field

As mentioned in the section a), the shielding effectiveness does not reach a clear trend, but the values are defined in the range. However, this does not mean that the same applies to the reflection of the electromagnetic field. This is because the ratio of absorption and reflection can change in the monitored frequency range. This ratio can be change depending on the shielding material. However, it is still true that the sum of the reflection and absorption of the electromagnetic field is equal to the shielding effectiveness. In Fig. 5 it is possible to see the dependence of the reflection of the electromagnetic field in the observed frequency band from 0.9 GHz to 9 GHz.

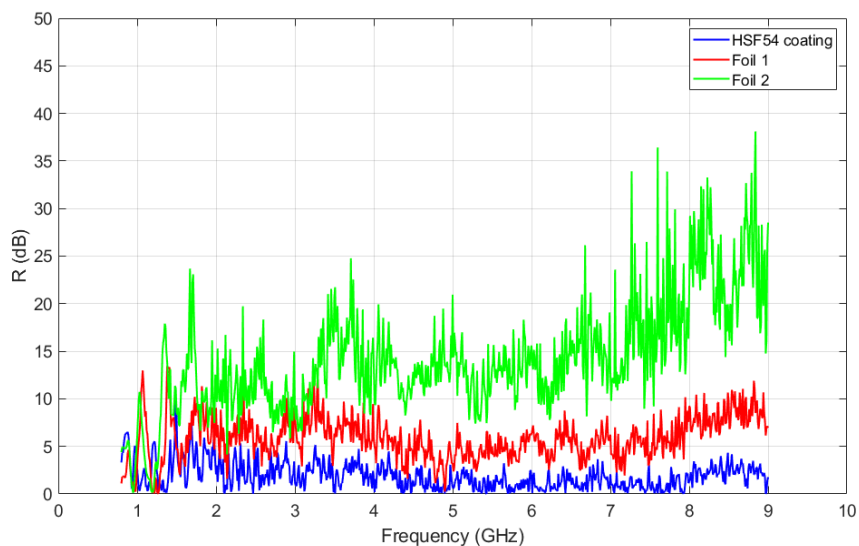


Figure 5

Reflection of electromagnetic field in the frequency range from 0.9 GHz to 9 GHz

From the results, it can be seen that the material Foil 2 achieves the highest values of electromagnetic field reflection. The material HSF 54 achieves the lowest values. In the investigated frequency range, an increasing trend of electromagnetic field reflection can be observed.

In the case of HSF 54 material, no trend was observed and the values are within a narrow range. The maximum value of electromagnetic field reflection for HSF 54 material is approximately 5 dB. The results show that the absorption of the electromagnetic field represent a larger part of the shielding effectiveness. This material therefore, absorbs the electromagnetic field more than it reflects it.

In the case of the Foil 2 material, the situation is the opposite. As the frequency increases, so does the proportion of electromagnetic field reflection. With the frequency increasing, the proportion of absorption decreases.

**c) Measuring the Spatial Charge**

The issue regarding the formation of spatial charge on shielding materials is relatively new. Accumulation of spatial charge may be dangerous for sensitive electronic devices. The main motive of the investigation the spatial charge was whether it would occur on the samples and in what quantity.

The measurement time was set to 100 seconds, while the measurement took place in the following manner. At time  $t_0 = 0$  s the measurement started, at time  $t_1 = 30$  s the antenna, i.e., the source of the electromagnetic field, was turned off, and the measurement of the spatial charge continued. The results were recorded by a computer connected to the measuring device. Subsequently, the voltage values were read at the respective times  $t_1 = 30$  s,  $t_2 = 60$  s and  $t_3 = 90$  s.

The workplace for spatial charge measurement is shown in Fig. 6. The Trek 541 A device was used for the measurement, with a measuring range from -1 kV to +1 kV. The measuring probe with high sensitivity is placed closest to the measured object at a distance of 2.5 mm – 1 mm. During the measurement, the transmitting antenna was placed at a distance of 1 m from the measured sample. The following figure 6, shows the wiring diagram.

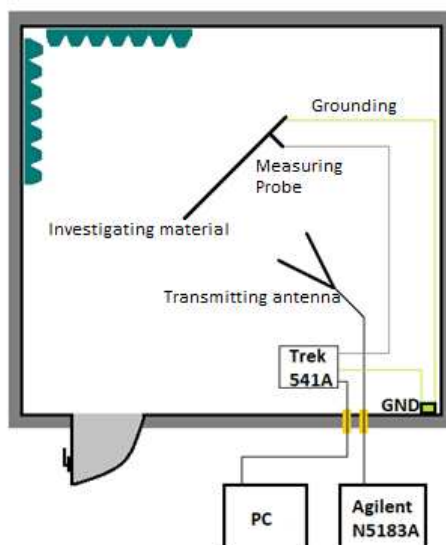


Figure 6

Experiment setup for measuring the spatial charge

The spatial charge measurement was performed with a grounded and ungrounded sample. Since the measured value was 0V when measuring with a grounded plate, the results will not be presented in the tables.

First sample on which the voltage of spatial charge was measured was a MDF board painted with professional paint YShield HSF 54. With an ungrounded plate, the value of the spatial charge voltage increased together with increasing frequency. The decrease in value occurred at the 7.4 GHz frequency. At frequencies of 8.6 GHz, the value increased sharply and reached the maximum value achieved with this sample. The charge had a positive polarity during the entire measurement at all frequencies.

Table 1

Values of measured spatial charge for a MDF board with HSF 54 shielding paint

f [GHz]	Ungrounded plate		
	Voltage of the spatial charge U [V]		
	t1 = 30s	t2 = 60s	t3 = 90s
0.9	5.5	5.5	6
2.1	6	5.5	6
2.6	5.5	5.5	6
3.8	6	6.5	6.5
5	7.5	7	7
6.2	7	7.5	6.5
7.4	3	7	6
8.6	12	11.5	13.5

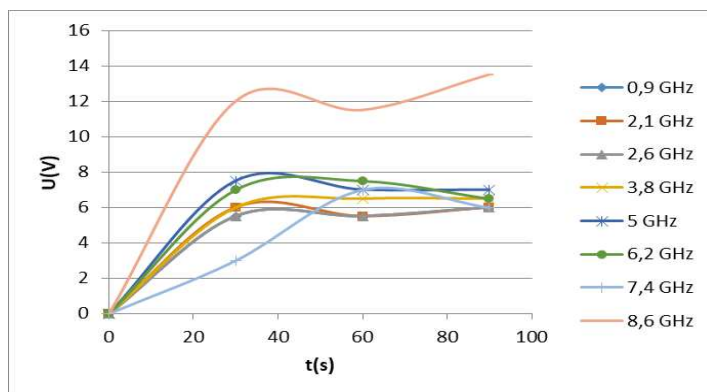


Figure 7

Dependence of spatial charge voltage on an ungrounded MDF board with HSF 54 shielding paint

The sample shielding foil 1 at the initial frequency of 900 MHz reached negative values of the spatial charge at all measured times in the range from -21V to -4.5V.

As the frequency increased to 2.1 Ghz, there was a sharp increase and subsequent pre-polarization. By gradually increasing the frequency, the spatial charge remained approximately the same, and the change occurred at a frequency of 6.2 GHz, when the charge increased slightly, until the frequency increased to 8.6 GHz, when the charge decreased again. Graphically, this course is shown on the Figure 8.

Table 2  
Values of measured spatial charge for a shielding foil 1

f [GHz]	Ungrounded plate		
	Voltage of the spatial charge U [V]		
	t1 = 30s	t2 = 60s	t3 = 90s
0.9	-24.5	-23	-21
2.1	3	1	1.5
2.6	0	3	1
3.8	1.5	1	1
5	1.5	3.5	2
6.2	4.5	5.5	7
7.4	6	7	6.5
8.6	2.5	2	3

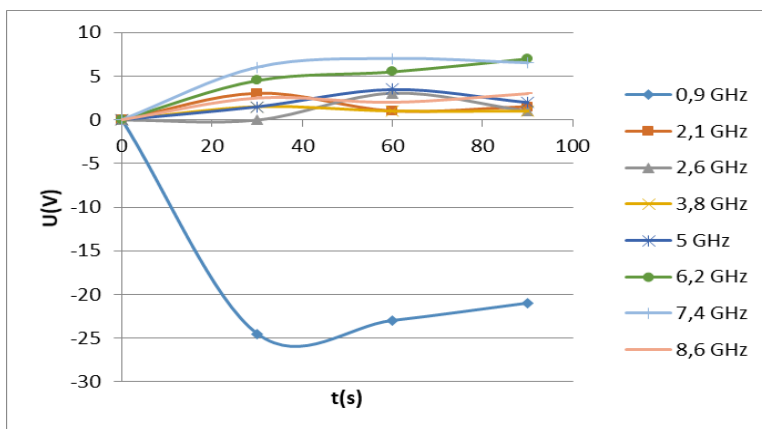


Figure 8  
Dependence of spatial charge voltage on an ungrounded shielding foil 1

The following table shows the results for a shielding foil 2.

Table 3  
Values of measured spatial charge for a shielding foil 2

f [GHz]	Ungrounded plate		
	Voltage of the spatial charge U [V]		
	t1 = 30s	t2 = 60s	t3 = 90s
0.9	-2.5	-0.5	-0.5
2.1	-1	-1	-1
2.6	-8	-10	-11.5
3.8	-11	-11	-13.5
5	-11.5	-12	-11.5
6.2	-9.5	-10.5	-11.5
7.4	-9	-11.5	-11.5
8.6	-10	-11.5	-10.5

Shielding foil 2 reached negative voltage values, which increased even after the antenna was turned off. The highest value of the voltage was at the frequency of 3.8 GHz at the time of 90 s, when 60 s had passed since the antenna was turned off. The change occurs at the frequency of 2.6 GHz at which the value of the charge increased, and from this value the space charge did not change much by changing the frequency.

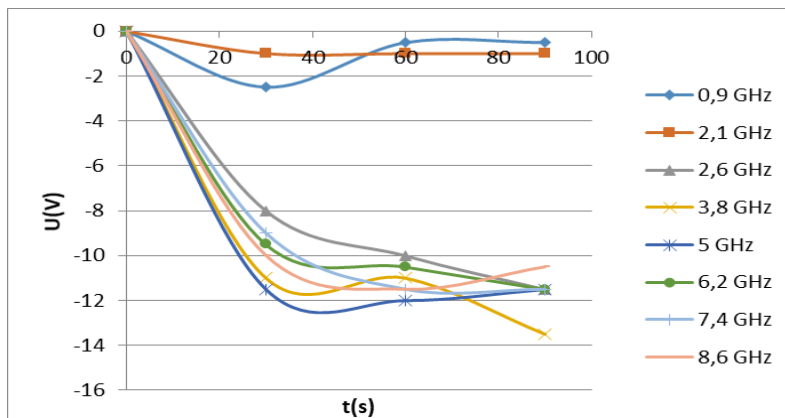


Figure 9

Dependence of spatial charge voltage on an ungrounded shielding foil 2

## Conclusions

This paper is focused on examining shielding effectiveness, measuring and reflection of electromagnetic fields. Shielding effectiveness consists of reflection and absorption of the electromagnetic field. If we know shielding effectiveness and reflection of the electromagnetic field, it is possible to calculate the absorption of the electromagnetic field. The measurements were performed in an anechoic

chamber, within the frequency range of 0.9 GHz to 9 GHz. Each measurement was repeated 3 times, in order to increase accuracy. Based on the measurements, it is possible to evaluate the research:

- a) By measuring the effectiveness of the shielding, it was found that all three materials have the shielding ability to prevent the penetration of the electromagnetic field. No of increase or decrease trend in shielding effectiveness values was observed. The values are defined in range from 10 dB to 30 dB.
- b) By measuring the reflection of the electromagnetic field, the situation is different. The material Foil 2 achieves the highest values of electromagnetic field reflection. The material HSF 54 achieves the lowest values. In the investigated frequency range, an increasing trend of electromagnetic field reflection can be observed. In the case of HSF 54 and Foil 1 material, no value trend was observed.
- c) The material HSF 54 achieves the lowest values of reflection of the electromagnetic field. It follows that this material achieves high values of absorption and is therefore suitable for absorbing the electromagnetic field. The same applies to foil 1. In the case of foil 2, the electromagnetic field reflection values also increase with increasing frequency. It follows that the absorption of the electromagnetic field decreases with increasing frequency.
- d) HSF 54 material is more suitable for absorbing the electromagnetic field. Foil 1 is also suitable for electromagnetic field absorption. In the case of foil 2, the absorption of the electromagnetic field decreases with increasing frequency, and at the same time the reflection of the electromagnetic field increases.

This research shows how to wisely choose shielding materials, in building planning and practice. There are cases when the reflection of the electromagnetic field is undesirable. In this case, the material HSF 54, is a suitable shielding for these purposes.

The second part of this work was focused on the measurement possibilities for the creation the spatial charge. Accumulation of spatial charge may be dangerous for sensitive electronic devices. Spatial charge was detected on all ungrounded samples under the influence of a high-frequency electromagnetic field. The presence of charge varies, depending on the frequency of the electromagnetic field and its duration. It can be stated that it is necessary to ground each shielding coating, in order to avoid injuries or the destruction of electronic equipment.

### **Acknowledgement**

This work was supported by the Scientific Grant Agency of the Ministry of Education of Slovak Republic and the Slovak Academy of Sciences by the projects, APVV-18-0160, VEGA 2/0011/20 and VEGA 1/0154/21.

## References

- [1] J. Zbojovský, M. Pavlík, D. Medved', I. Kolcunová, Modeling the propagation of HF electromagnetic field through the “brick” building material, 2019. In: Proceedings of the IEEE 2<sup>nd</sup> International Conference and Workshop in Óbuda on Electrical and Power Engineering. - New York (USA): Institute of Electrical and Electronics Engineers s. 17-20 [online] - ISBN 978-1-7281-4358-3
- [2] M. Pavlík, J. Zbojovský, M. Oliinyk, M. Ivančák, Compare of shielding effectiveness for building materials with different air gap, In: Elektroenergetika 2019 : Proceedings of the 10<sup>th</sup> International Scientific Symposium on Electrical Power Engineering. - Košice (Slovensko) : Technická univerzita v Košiciach s. 189-192 [CD-ROM] - ISBN 978-80-553-3324-3
- [3] J. Zbojovsky, L. Sarpataky, M. Sarpataky, "Shielding effectiveness of concrete in dependence of his electric properties", In: Przegląd Elektrotechniczny = Electrotechnical Review. - Warsaw : Stowarzyszenie Elektrykow Polskich, 1919 Vol. 98, No. 1 (2022) pp. 204-207 [print, online] - ISSN 0033-2097 DOI: <https://doi.org/10.15199/48.2022.01.45>
- [4] M. Pavlik, J. Zbojovsky, M. Oliinyk and M. Ivancak, "Experimental Study of High Frequency Electromagnetic Field Penetration Through Building Material - Concrete Wall," *2019 20<sup>th</sup> International Scientific Conference on Electric Power Engineering (EPE)*, 2019, pp. 1-4, doi: 10.1109/EPE.2019.8778183
- [5] N. Abbas, H. T. Kim, Multi-Walled Carbon Nanotube/Polyethersulfone Nanocomposites for Enhanced Electrical Conductivity, Dielectric Properties and Efficient Electromagnetic Interference Shielding at Low Thickness. In: *Macromolecular Research*, Vol. 24, issue 12, p. 1084-1090, December 2016. ISSN 2092-7673. DOI:10.1007/s13233-016-4152-z
- [6] M. Kolcun, A. Gawlak, M. Kornatka, Z. Conka, “Active and Reactive Power Losses in Distribution Transformers”, 2020, ACTA POLYTECHNICA HUNGARICA 17 (1), pp.161-174, DOI: 10.12700/APH.17.1.2020.1.9
- [7] E. Lumnitzer, P. Liptai, R. Drahos, "Measurement and Assessment of Pulsed Magnetic Fields in the Working Environment" In: Proceedings of the 8th International Scientific Symposium on Electrical Power Engineering - ELEKTROENERGETIKA 2015. Košice : TU, 2015 pp. 331-333. ISBN 978-80-553-2187-5
- [8] G. Bachir, H. Abdechafik, and K. Mecheri, “Comparison electromagnetic shielding effectiveness between single layer and multilayer shields,” 2016 51<sup>st</sup> International Universities Power Engineering Conference (UPEC). IEEE, Sep. 2016. doi: 10.1109/upec.2016.8114106

- [9] D. Medved, P. Zvanda, "Electromagnetic Field Distribution Modeling and Measuring of the 110 kV Substation", In: Proceedings of the 10<sup>th</sup> International Scientific Symposium on Electrical Power Engineering - ELEKTROENERGETIKA 2019. Košice: TU, 2019, pp. 81-86. ISBN 978-80-553-3324-3
- [10] I. Kolcunová, J. Zbojovský, M. Pavlík, S. Bucko, J. Labun, M. Hegedus M. Vavra, R. Cimbala, J. Kurimsky, B. Dolnik, J. Petráš, J. Džmura, "Shielding Effectiveness of Electromagnetic Field by Specially Developed Shielding Coating" In: Acta Physica Polonica A., Instytut Fizyki Vol. 137, No. 5 (2020), pp. 711-713, ISSN 0587-4246, doi: <https://doi.org/10.12693/APhysPolA.137.711>
- [11] S. Ch. Lin, Ch. Ch. M. Ma, Sh. Ts. Hsiao, Yu. Sh. Wang, Ch. Yu. Yang, W. H. Liao, S. M. Li, J. An Wang, T. Yu Cheng, Ch. Wen Lin, R. Bin Yang, Electromagnetic interference shielding performance of waterborne polyurethane composites filled with silver nanoparticles deposited on functionalized graphene. In: Applied Surface Science, Vol. 385, pp. 436-444, November 2016, ISSN 0169-4332 DOI: 10.1016/j.apsusc.2016.05.063
- [12] IEEE 299-2006 Standard, Method for Measuring the Effectiveness of Electromagnetic Shielding Enclosures, EMC Society, New York 2006, p. 39

# Recent Challenges Regarding the Verification of Photovoltaic Inverters Properties and their Compliance with Technical Requirements

**Martin Vojtek, Petr Mastny, Jan Moravek, Jiri Drapela, Michal Vrana, Jiri Dvoracek**

Faculty of Electrical Engineering and Communication, Brno University of Technology, Technicka 12, 61600 Brno, Czech republic  
vojtek@vut.cz, mastny@vut.cz, moravek@vut.cz, drapela@vut.cz,  
xvrana10@vut.cz, dvoracekj@vut.cz

---

*Abstract: Distributed generation by renewable energy sources, is a new phenomenon in recent years and it brings several challenges for electric power system operations. Given that, distributed generators shall be strictly in compliance with relevant standards and technical requirements, to preserve current level of quality and reliability of electric power supply. Therefore, this research is aimed at compliance verification of non-synchronous power generating modules, with any relevant requirements. At the beginning, it provides comprehensive review on this issue including historical development, the current situation in the Czech Republic and relationships between legislation and standards, currently in force. The main contribution of the paper lies in the experiments performed on photovoltaic inverters, which represent the key components of photovoltaic systems and are responsible for fulfilling the imposed operational requirements. The results provide a real-world picture of the current state, in this field. We found that none of the tested inverters fulfilled the requirements to the full extent and therefore, we recommend careful verification of the power generating modules, units or component's ability in this regard, before commissioning.*

*Keywords: photovoltaic; inverter; requirements; RfG; EN50549-1; compliance*

---

## 1 Introduction

The growth of living standards and constant social and economic development arising the need to secure more and more energy in a sustainable way. Currently, the majority of energy (more than 70% [1]) comes from fossil sources such as oil, coal and natural gas. The global trend is a gradual transition to renewable energy sources (RES) due to several factors. First, there is a question of climate change, which an integral part of fossil fuel usage and the associated greenhouse gas

formation. Also, with increasing global energy consumption, the required amount of fossil fuels increases. Non-renewable resources are limited and energy extraction is therefore not sustainable in the long term. Similarly, there is an effort of individual countries to increase their energy independence on fossil fuels imported from abroad. All these factors lead in developed countries to national and transnational policies for carbon neutrality with clearly defined milestones for individual years (for example, 2030 or 2050). This is possible only by gradually increasing the share of RES used in electricity production but also, for example, in transport. Developing countries are also following these goals. For example, China, which is the largest producer of greenhouse gases in the world, aims to be carbon neutral by 2060 [2]. Despite this, fossil fuels remain the main source for electricity generation with a share of approximately 40% from a global perspective [3].

Photovoltaic (PV) power plants are among the most widespread RES in the Czech Republic, primarily due to the favorable climatic conditions and problem-free availability of the primary source. The breakthrough years were 2009-2012, when the so-called "PV boom" caused by massive government support resulted in a strong increase of installed capacity (from 39.5 MWp in 2008 to 1959.1 MWp in 2010). The most significant part was created by PV plants with nominal power outputs ranging from ones up to tens of MW connected at the medium voltage (MV) level. Due to the unexpectedly fast progress towards the fulfillment of the European Union energy targets until 2020 [4], to which the Czech Republic committed itself, the government support was gradually reduced and finally completely suspended from 1 January 2014. After this date, legislative support gradually began to move towards to sources with low power output aiming on maximizing the consumption of the generated electricity at the place of production. For example, in 2014, a subsidy program called new green savings [5] was launched, which was intended for energy savings in family houses and apartment buildings (the next stage is currently underway, which is expanded to include other areas of energy savings). Subsequently, in 2016, the term "microsource" was introduced by decree No 16/2016 of the Energy Regulatory Office [6]. Microsource is source with a rated current of up to and including 16 A per phase and a total maximum installed power of up to and including 10 kW. Advantage is, that there is no license needed and the decree provides also the possibility of a simplified connection process of small sources falling into this category after meeting defined conditions, which include, for example, preventing the power supply to the distribution system (DS) by appropriate technical means. In practice, they are almost exclusively PV plants connected to the low voltage (LV) with some form of surpluses accumulation and outputs in the order of kW. This led to a change in the previous trend and the expansion of the so-called hybrid systems, which can be very effective when properly designed and optimized [7]. In case of any interest in the supply of electricity to the DS, the microsource must undergo the "first parallel connection process". Subsequently, the owner of the resource has various business models at his disposal, such as the

supply of electricity to the grid at spot prices, or recently increasingly popular concept called "virtual battery".

Historical and related legislative developments in the field of RES lead to the current situation where a large number of distributed generation (DG) with low power output are gradually connected to the grid across the country. Annual increments in the number of PV installations and the total amount of installed power are shown in Figure 1. There is clear exponential trend currently fueled especially by high energy prices. In the first half of 2022, higher numbers of installations were added with an overall larger portion of installed capacity than in the entire previous year.

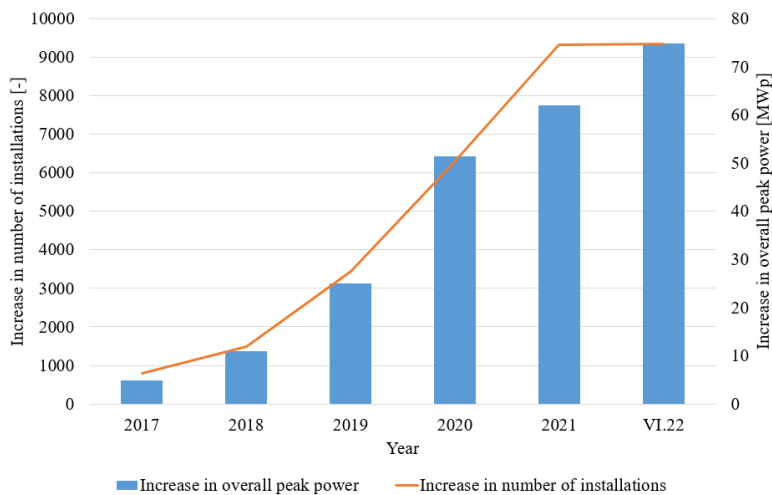


Figure 1

Increase in PV installed capacity and number of installations in the Czech Republic [8]

DG represents a change in existing approaches and brings a number of challenges in terms of managing the operation of the electric power system. In certain types of DS, there may be problems with power flow direction and voltage limits. This is mainly the case of the LV grids in rural areas. These are typical by long radial feeders with a relatively small cross-section, the consequence of which can be a high impedance at the point of common coupling (PCC). The load profile in rural areas is also significant factor, which is low during the day while PV plants power generation is high. The combination of these factors at a certain level of RES penetration can lead to a reverse power flow to the superior system and increase in voltage above the permitted limits defined in the EN 50160 [9]. Subsequently, it can cause source protections tripping, which is undesirable for both the distribution system operator (DSO) and the source owner. From the source owner point of view the electricity is not generated, and from the DSO point of view, problem is solved only for very short time. After tripping, voltage will return to the permitted limits, plant will resynchronize and problem will recur. In addition

there are also another issues which can possibly occur [10], including voltage asymmetry or harmonic current distortion by power electronics, which can affect loads, protections and increase losses of distribution transformers [11] [12].

Considering the aforementioned potential problems, it was necessary to formulate clear requirements on DG in order to prevent negative phenomena and maintain the current quality and reliability of electric power supply. From the European point of view, the Network Code on Requirements for Grid Connection of Generators (RfG) [13] was established in 2016. The power generating modules (PGMs) are divided into individual categories depending on the nominal power output with different mandatory and non-mandatory requirements imposed on each category and generation technology (synchronous or non-synchronous). RfG became integral part of regional grid codes, because ENTSO-E members have been obliged (according to [13]) to implement the requirements by April 27<sup>th</sup>, 2019. EU countries have taken different approaches of implementation, but in any case, the result is that all newly connected power generation facilities (PGFs) or PGMs must meet the requirements. The RfG task is not to solve the grid specifics in individual countries, therefore the implementation of optional requirements or the specific range of required values for several mandatory requirements is left to local technical regulations.

Product standards were subsequently created in line with RfG - EN 50549-1 [14] and EN 50549-2 [15] focusing on sources connected to LV and MV, respectively. The standards are established so that the PGFs/PGMs assembled from products which conform with EN 50549-1/2 are able to achieve compliance with the RfG and its national implementation (national grid code, e.g., PPDS:P4 [16] in the Czech Republic). The specific parameters of individual RfG and EN 50549-1/2 requirements are defined at the national level, or even at the level of individual DSOs according to local specifics. The relationships between national technical regulations, standards and EU regulations are shown in Figure 2.

According to [17], the manufacturer must ensure that products which he is going to introduce on the market are designed and manufactured according established regulations and technical requirements. He submits all the information and documentation necessary to prove the conformity of the product to the competent national authority. It is also his duty to draw up and issue a product declaration of conformity with the relevant requirements, but manufacturer is in conflict of interests, because he has significant economic interest in introducing the product on the market. Therefore, the declaration of conformity may not provide a guarantee of conformity fulfillment. This can lead to the introduction of such products on the market, which do not meet the requirements partially, or even in their entirety.

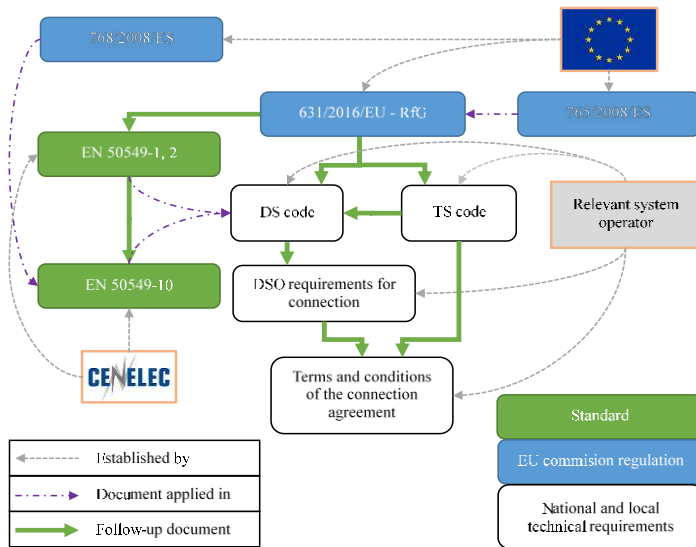


Figure 2

Relationships between relevant documents

The purpose of all legislative regulations and technical requirements related to DG, including PV plants, is to ensure their safe operation and to mitigate or completely eliminate negative impacts, such as voltage rise, etc. Therefore, it is absolutely necessary to ensure the correct and uniform application of the regulations to all products from all manufacturers placed on the common European market. This basic assumption is currently only slightly enforced in practice. For example, in the Czech Republic, the DSOs within the first parallel connection process (process of connecting such a source that is expected to supply the electricity to the grid) require proof of compliance through the "Document of generating module". However, it is only an ordinary form in which the contractor and the PGF owner guarantee the compliance with RfG and PPDS:P4 by their signature. The weight of such a document is therefore controversial and since the declaration of conformity is also not a reliable way how to prove the compliance, the only option, which is logically offered, is independent verification, for example, in certified third-party laboratories. The problem is the lack of testing workplaces and non-existing verification methodology or related standards nowadays (2022).

The aim of this contribution is to provide a comprehensive overview about the operational characteristics of DG (especially PV plants) and their verification. Currently, apart from the authors' contributions [18]-[22], there is only a minimum of publications [23] [24] focused on this very important but at the same time often overlooked area. The requirements imposed on non-synchronous PGFs are analyzed, potential problems and risks associated with their implementation are identified, and the need for systematic compliance verification is rationalized.

The practical experiments are focused on PV systems where the key component of the system, the PV grid-tie or hybrid inverter, is responsible for the whole system operational properties. Presented verification results provide a realistic picture of the current situation in the requirements implementation by individual manufacturers of PV inverters.

## 2 Selected Requirements for Verification

RfG and EN 50549-1/2 contain a number of requirements regarding synchronous and non-synchronous PGMs. As this contribution deals with compliance of PV inverters, requirements for non-synchronous PGMs are relevant and those that can have a fundamental impact on DS operation have been chosen for verification. The tested PV inverters are considered as components intended for use in A category of PGMs and for connection to LV DS. Therefore, the technical standard EN 50549-1 (hereinafter as EN) and local implementation of RfG – PPDS:P4 is applied and verified. An overview of selected requirements is given in Table 1. From an overall perspective, they can be divided into requirements imposed on withstand capability to sudden change of certain quantity and requirements that require an active response as the reaction to the change in the related quantity. In the following subsections, these requirements will be explained in detail together with the relevant legislative documents as well as technical standards and the specification of individual parameters with regard to national localization through the grid code in the Czech Republic.

Table 1  
List of selected requirements

Requirement	RfG (article)	EN 50549- 1 (subclause)
Rate of change of frequency (ROCOF) immunity	13.1(b)	4.5.2
Power response to over-frequency	13.2	4.6.1
Automatic connection and starting to generate electrical power	13.7	4.10
Voltage support by reactive power	17.2	4.7.2
Voltage related active power reduction	-	4.7.3

### 2.1 Rate of Change of Frequency (ROCOF) Immunity

In general, PGFs should contribute to overall stability by withstanding dynamic changes in magnitude and frequency of voltage, unless safety standards require disconnection. ROCOF immunity is the only one of the selected, for verification, which can be considered to meet the withstand capability requirement. Other examples, which are not subjects in this paper, are the fault-ride-through

capability, defined in RfG and the Under-voltage ride through or Over-voltage ride through defined in EN.

ROCOF immunity shall be provided regardless of protection settings. It means that the PGF shall remain connected and able to operate during frequency changes at a defined rate. The PGMs within the PGF shall have ROCOF immunity greater than or equal to the value defined by the responsible party (DSO or TSO) according to EN and RfG. It is also stated in EN, that when the ROCOF immunity is not defined by the responsible party, at least 2 Hz/s must apply for non-synchronous generation technologies.

Grid code in the Czech Republic requires the same value for non-synchronous PGMs as default stated in EN – 2 Hz/s.

## 2.2 Power Response to Over-frequency

Power response to over-frequency is defined both in EN and RfG, while RfG uses the term “limited frequency sensitive mode – over-frequency (LFSM-O)”.

PGF shall activate active power response to over-frequency after reaching an activation frequency threshold. Active power shall decrease with predefined droop as a response to increasing frequency. Both the frequency threshold for activation ( $f_1$ ) and frequency droop ( $s$ ) shall be programmable in the range of at least 50.2 to 52 Hz and at least 2 to 12%, respectively, according to EN. The parameters are specified by relevant transmission system operator (TSO).

The droop reference power is  $P_{ref}$ , which is different for synchronous and non-synchronous PGMs. For non-synchronous PGFs  $P_{ref}$  is the power generated at the moment when the frequency reaches the threshold value. The value of active power calculated according to reference power  $P_{ref}$  and droop defines the maximum power limit (Figure 3). For example, when the power of the primary source decrease during activated active power response to over-frequency, lower values of delivered power are allowed.

EN also requires the possibility to set a threshold value for deactivating the function ( $f_{stop}$ ), which is used in some countries. Its basic principle (graphically explained in Figure 3) is that the power to which the PGF was limited remains constant even when the frequency is decreasing until the threshold value for deactivation is reached. After deactivation, power can be increased gradually with the same rate as defined in requirements for automatic connection and starting to generate electrical power.

The frequency threshold for activation is 50.2 Hz, the frequency threshold for deactivation is 50.05 Hz a droop is 5% according to Czech grid code.

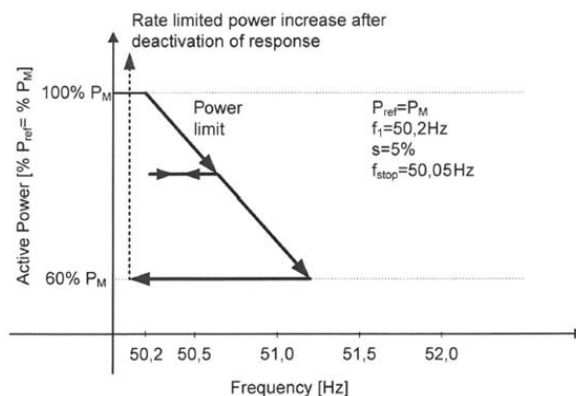


Figure 3

Power response to over-frequency - settings according to Czech grid code

### 2.3 Automatic Connection and Starting to Generate Electrical Power

Synchronization of PGFs with DS shall be fully automatized. Relevant TSO shall specify requirements on automatic connection and starting to generate power according to RfG. EN imposes two categories of requirements depending on whether it is automatic reconnection and starting to generate power after interface protection tripping (as a fault result) or it is standard operational start. For both situations automatic connection and starting to generate electrical power is allowed only if the voltage and frequency are within the permitted range for at least the evaluation period that is specified. Permitted ranges as well as evaluation period shall be settable within minimal ranges provided by EN, together with the default values which shall apply when no settings are specified by the DSO.

The subject of compliance testing presented in this article are requirements for automatic reconnection and starting to generate power after fault occurrence. The Czech grid code enables automatic connection and starting to generate electrical power after interface protection tripping in this situation:

- Frequency and voltage are for at least 5 min in the ranges below:
  - $U = (0.85 - 1.10) \times U_n$
  - $f = 47.5 - 50.05 \text{ Hz}$

Also, power output shall rise gradually up to available power with maximum rise rate (gradient) of 10% of nominal power per minute after synchronization.

## 2.4 Voltage Support by Reactive Power

RfG does not impose any requirements for reactive power regarding to A category PGMs. Voltage support by reactive power is defined in EN within requirements referred as power response to voltage changes. It states that the PGFs must be able to control active and reactive power if required by the relevant DSO. At the same time, PGF must not lead to exceeding the permitted voltage limits in [9] and during the normal operation conditions shall be able to contribute to maintaining the voltage within the limit. Requirements for reactive power capability are in line with EN in the Czech republic and they are shown in Figure 4.

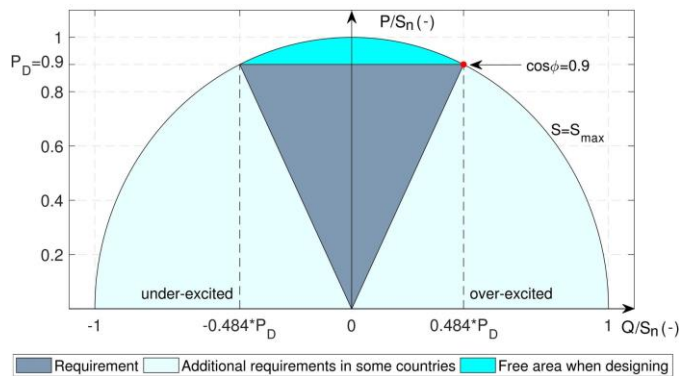


Figure 4

Requirements on reactive power of PGMs in the Czech Republic

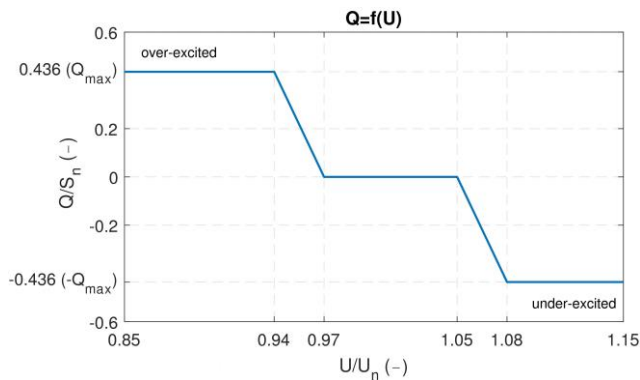


Figure 5

The most common setting of reactive power control characteristic in the Czech Republic

There are several control modes which can utilize reactive power capability defined in EN. They include simple fixed  $Q$  and  $\cos\phi$  setpoint control modes or more complex one, based on predefined control characteristics – reactive power dependent on voltage -  $Q(U)$  or  $\cos\phi$  dependent on active power -  $\cos\phi(P)$ .

Currently, all DSOs in the Czech Republic require exclusively Q(U) control mode. This mode automatically set reactive power, which corresponds to specific voltage value based on control characteristic. The specific setting can be required individually in connection agreement, but the Czech grid code specifies the default setting shown in the Figure 5.

## 2.5 Voltage Related Active Power Reduction

Similar to the previous case, active power reduction is not required within the RfG. EN also does not directly define this requirement, but allows the implementation of a function that reduces the active power depending on the voltage in order to prevent the overvoltage protection tripping. Based on our long time practice in the field, control characteristic in Figure 6, which is characterized by two points - values of voltage for 100% and 0% of nominal inverter power is the most commonly implemented. The setting of control characteristics in Figure 6, is commonly required by the largest DSO in the Czech Republic. However, different settings can be required individually in connection agreements.

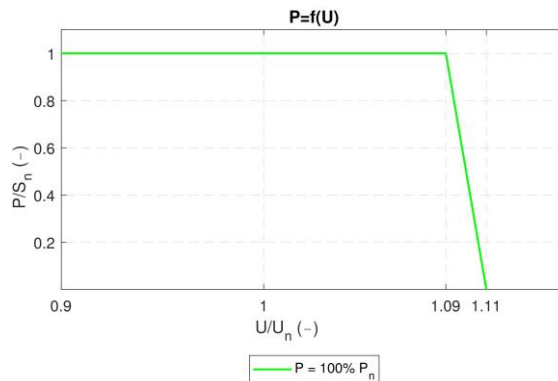


Figure 6

The most common setting of voltage related active power reduction control in the Czech Republic

## 3 Test Platform and Tested Inverters

A test platform with the necessary equipment for complex compliance testing of 1-phase and 3-phase PGUs and components of PGMs up to 50 kW with the requirements of EN 50549-1/2 [14] [15], RfG [13] and PPDS:P4 [16] was built at Department of Electrical Power Engineering at Brno University of Technology. Its composition allows to simulate low voltage alternating current system, enabling the simulation of selected phenomena on the output voltage, separately from the public DS, for testing the behavior and response of the inverter based PGUs or

components of PGMs, but also more complex local energy management systems in cooperation with battery energy storage systems and loads. The wiring diagram with all of the equipment used for compliance verification is shown in Figure 7.

Selected laboratory equipment allows to perform repeatable tests always with the same parameters according to predefined test procedures. A DUT – in this case a tested PV inverter is supplied by programmable DC source at its DC side. DC source can be operated in PV simulator mode and is able to simulate various nonlinear voltage-current characteristics of PV module or PV array up to 10 kW. The 4-quadrant AC programmable source is powered by DS and it is used to create an artificial grid where the tested inverter is connected. Source output voltage and frequency can be changed arbitrarily and different test sequences can be programmed using the appropriate software. Selected quantities (voltage, current, power, etc.) were measured at the inverter's input and output. Aggregated values were recorded every 50ms - the smallest sample time of the analyzer used.

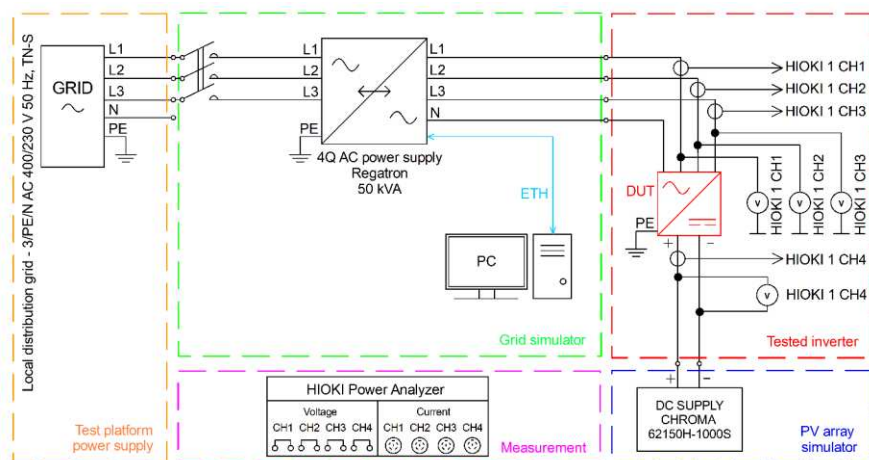


Figure 7

Test platform wiring diagram for inverters verification purposes

Overall, three photovoltaic inverters from three different manufacturers were tested. Their brief specification and marks used in the results presentation are given in Table 2. All of the tested inverters are available on the common European market and were purchased in the Czech Republic while also had a declaration of conformity with RfG and EN. Before the testing, the firmware was updated to the latest version. Then, they were configured in order to operate according to Czech grid code. This option is available in user interface of each inverter after entering the installer code and this is the most common way of parametrization by certified installers based on which they declare the compliance in "Document of generating module", which is required by DSO.

Table 2  
Inverter's specifications

Mark	Nominal power $P_n$ [W]	Number of phases [-]	Type
A	10000	3	hybrid
B	6000	3	hybrid
C	6000	3	hybrid

## 4 Results and Comments

Graphs, which are used for the results presentation and evaluation of the individual requirements described in chapter 2, contains the measured values together with the required response of the inverter according to the requirements in the Czech Republic. In order to allow easy comparison of the results, values of active and reactive power were converted into per unit system. A base unit to which measured values are referenced are nominal power outputs of each inverter. Inverters B and C were tested at output power equal to 100% of nominal, while inverter A at 80% of nominal due to laboratory equipment and MPPT input limitations.

The first of the verified requirements is automatic connection and starting to generate electric power after a fault. In this case, the 3-phase symmetrical overvoltage was simulated as the fault and the integrated interface protection of all inverters tripped. The course of the active power from the moment when the voltage returns to the nominal value is shown in Figure 8. The frequency was equal to the nominal value of 50 Hz and constant during the whole test. As can be seen, the inverter B and C fulfill the requirement on time delay before synchronizing to the grid after the voltage and frequency return to the interval between limit values, because the observation time until the inverters started to generate power was exactly 300 s. Subsequently, inverter C increased the output power with a gradient of precisely prescribed 10%  $P_n$ /min while inverter B with a slightly lower gradient, namely 9.66%  $P_n$ /min. However, a gradient lower than the prescribed one is allowed and therefore it can be concluded that the inverter B and C meets the requirements. On the contrary, Inverter A synchronized to the grid approximately 30 s after the voltage returned to the limits and began to supply all available power almost immediately. This means that it does not respect the requirements in the Czech republic and therefore, does not comply.

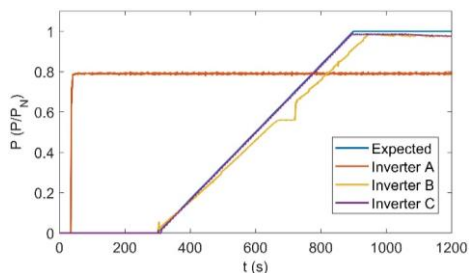


Figure 8

Active power during starting to generate electrical power after synchronization

Verification of withstand capability to fast frequency changes was performed for overall three changes, as can be seen in the right part of Figure 9. All the frequency changes were performed with  $ROCOF = 2 \text{ Hz/s}$ , as this is the minimum required rate that the inverters must withstand. At the beginning of the test sequence, the voltage and frequency were kept constant until inverters synchronize. After inverters ramped up to the available power and reached a steady state, the frequency was increased by 1 Hz, followed by 2 Hz decrease and 1 Hz increase back to the nominal frequency. The decisive criterion for the ROCOF requirement compliance evaluation is that the inverter remains connected and is able to operate during fast frequency changes. As can be seen in the left part of the figure, all three tested inverters remained connected and continued to supply active power to the grid. Therefore, the requirement for ROCOF immunity can be considered fulfilled and in compliance with the requirements in the Czech Republic for all tested inverters.

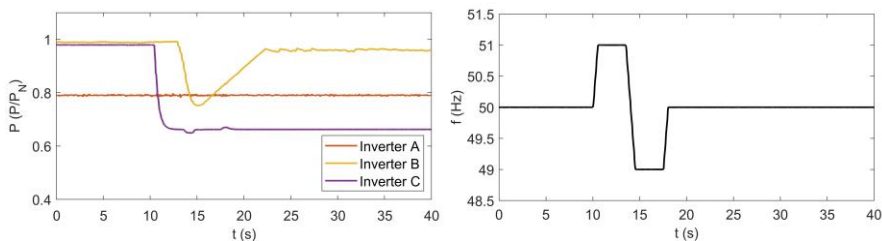


Figure 9

Active power response to rapid frequency changes

As already mentioned, the inverters have been configured to default setting for the Czech Republic without any changes, and thus active response to frequency changes (LFSM-O) should be activated. Inverter A did not respond in any way to the frequency drop, which probably indicates that it has a high response time, or this function is not active. For inverters B and C, the active power decrease occurs, probably due to LFSM-O, while it can be seen that the inverters have different response and inverter B has higher response time. In the next sequence, a

test dedicated exclusively to the verification of LFSM-O will be described, where this behavior will be clarified.

At the beginning of testing sequence for verifying of LFSM-O compliance, similar to the previous case, constant frequency and voltage were applied at the inverters terminals to reach the steady state. After that, the test sequence continued by the smooth increase of the frequency from the nominal value up to 52 Hz, followed by the smooth decrease back to the nominal value with 5 mHz/s rate of change of frequency. The frequency during the testing sequence can be seen in the right part of Figure 10 and the response of the inverters in the left part. The measured values were also averaged in one second and plotted in the P-f area (Figure 11) for easy compliance assessment and evaluation of the response settings (frequency threshold for activation and deactivation of the function, reference power and droop). The results show that, as indicated by the ROCOF test, power output of inverter A does not respond to frequency changes. In addition, the integrated interface protections tripped the inverter at 51.8 Hz. This behavior does not meet the requirements for LFSM-O even for the protection settings (in the Czech Republic, the non-synchronous PGMs shall be disconnected if the frequency exceeds 52 Hz). In this respect, inverter B and C did not show any deviations and LFSM-O is active in both of them. Droop and threshold value for activation are correctly set. On the other hand, inverter B does not have set the threshold value for deactivation and therefore does not comply with the requirements. Inverter C has a correctly set threshold value for deactivation, but does not respect the prescribed power increase gradient to be applied according to EN. After reaching the threshold value for deactivation, it waits for 300s and after that, it ramps up the output power to the available power rapidly. For this reason, it can be concluded that only inverter C has LFSM-O in compliance with the requirements in the Czech Republic, but it does not conform with EN.

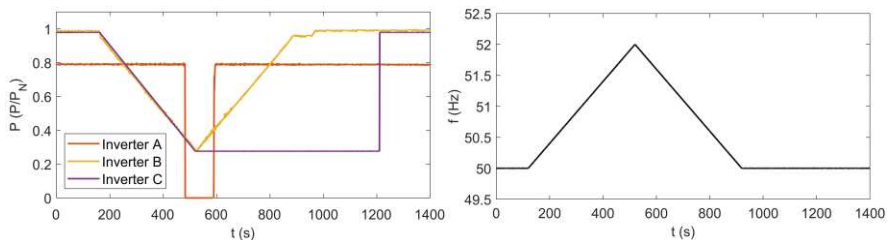


Figure 10

Active power response to over-frequency

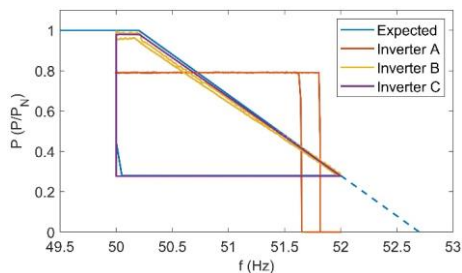


Figure 11

Active power response to over-frequency in P-f area

To verify the response of active and reactive power to voltage changes, a gradual change of voltage from a nominal value to 258 V, followed by a gradual decrease to 202 V and a return to the nominal value was used after steady state was reached. The rate of change of voltage was 50 mV/s. The test signal can be seen in the right part and the reactive and active power response in the left part of Figure 12 and Figure 13, respectively. Similar to the previous case, measured values were averaged in one second and plotted in Q-U and P-U area (Figure 13) respectively. Based on the measured data, it is clear that the inverter A was operated with a constant power factor (approximately about 0.9) and both the Q(U) and P(U) control mode were not active. In addition, it was not capable of continuous operation at a voltage lower than 215 V, when it was disconnected. Due to incorrect implementation of the requirements for automatic connection and the starting to generate electrical power, the inverter was repeatedly connected and disconnected from the grid, with the disconnection occurring after the output power has increased to the available power. This behavior can have a negative impact on the power quality, especially on the voltage fluctuations at the point of common coupling. Measured values during period of repeated connection and disconnection have been removed from P-U and P-Q area for better readability. Inverter B activated the control mode for voltage support by reactive power depending on the voltage both in the case of an increase and a decrease in voltage.

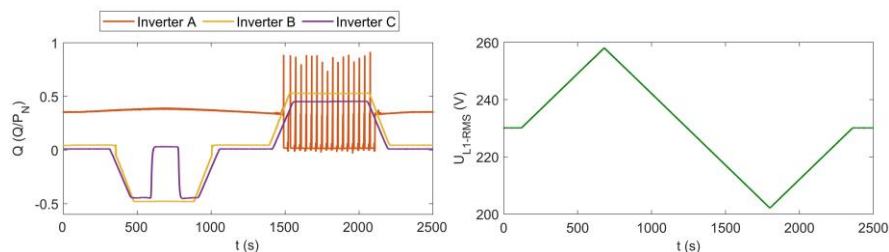


Figure 12

Reactive power response to voltage changes

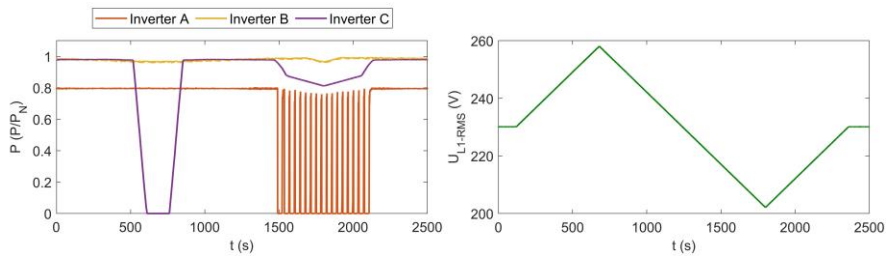


Figure 13

Active power response to voltage changes

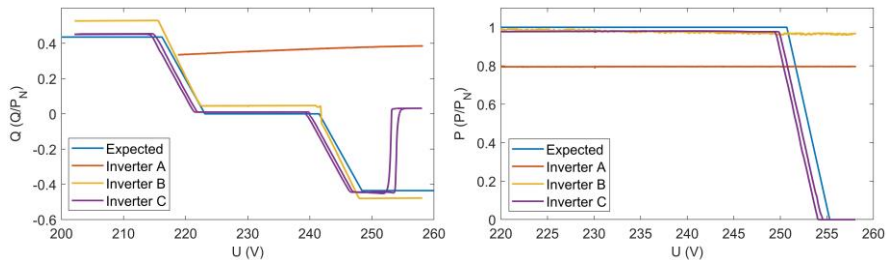


Figure 14

Reactive and Active power response to voltage changes in Q-U area and P-U area respectively

It is clear from the Figure 14 that the parameters of the Q(U) control mode are not in compliance with the requirements in the Czech Republic because inverter exceeds maximum and minimum required reactive power and therefore reaches lower power factor than 0.9 in both cases. Voltage dependent active power regulation was not activated in the entire tested voltage range. Inverter C supplies the reactive power according to required Q(U) control characteristic, but values of reactive power are a little bit shifted to the left. This could occur due to different measurement uncertainty of the inverter and power analyzer. Also, reactive power response is not exactly the same for the same voltage when voltage is increasing and decreasing respectively. Active power response to voltage is valid and according to requirements, but same the same statements are valid as in the previous case. After active power was limited to the zero, inverter was no longer able to provide reactive power support of voltage. The measured values were also processed into the P-Q area (Figure 15) together with the expected working space according to the nominal apparent power declared by the manufacturer. Inverter B and C are able to exceed the nominal current limits, while for inverter A, this could not be assessed. In view of the above facts, it is clear that none of the tested inverters is in compliance with the requirements for the reactive power supply depending on voltage, and only inverter C, is in compliance with the requirement for voltage related active power reduction.

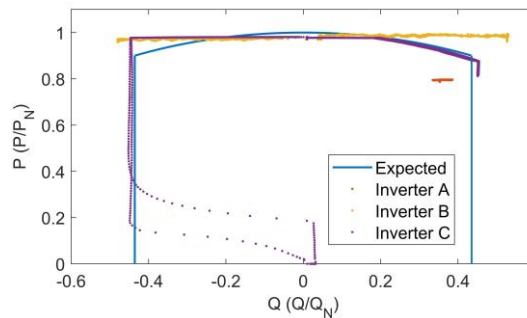


Figure 15  
PQ diagram of tested inverters

## Conclusions

This paper examines the requirements imposed on one of the most crucial components of non-synchronous power generating modules - photovoltaic inverters and experimental laboratory verification of their compliance with the requirements in the Czech Republic. Verification was carried out in ResLab laboratory at Brno University of Technology. The main goal is to present the actual situation in this area and to point out the serious problems, that occur in the implementation of requirements, by the inverter manufacturers.

Overall, three inverters were tested. It was found and proven by the results obtained and presented in this paper, that none of the tested inverters fulfilled the requirements according to the RfG, EN 50549-1 standard and their Czech localization, through the grid code referred here as PPDS:P4. This fact leads to the conclusion that PV inverter manufacturers are not able to correctly and consistently implement the requirements, as defined by national/international standards and regulations, as well as provide sets of settings for individual markets and local grid code requirements. If this trend continues, it may, in the future, have a fundamentally negative impact on the safety, reliability, quality, efficiency and predictability of the DS operations, as well as the operations for the entire electric power system.

Among the most significant deviations found were:

- Not respecting the grid parameters observing time before synchronizing and subsequent power rise gradient after fault
- Inactive or incorrectly set active power response at over-frequency
- Inability to operate in the entire operating range of voltage
- Inactive or incorrectly set reactive power response to voltage changes
- Inactive or incorrectly set active power response to voltage changes

Considering the above mentioned, we strongly recommend the swift establishment of standards for testing and verification of non-synchronous power generating modules, units and components. Furthermore, the introduction of certification processes and accredited laboratories, intended for the detailed examination of the compliance of all power generating modules, to be used in parallel operation with DS, at least within the type range.

Last, but not least, reliable requests and control of compliance with any imposed requirements, not only on the basis of a declaration of conformity, but on the basis of certificates issued by third parties, for example, certified laboratories that have no economic motivations, in relation to a component manufacturer.

### **Acknowledgement**

This research work has been carried out in the Centre for Research and Utilization of Renewable Energy (CVVOZE). Authors gratefully acknowledge financial support from the Technology Agency of the Czech Republic (project No. TK04020103).

### **References**

- [1] International energy agency. Available online: <https://www.iea.org/fuels-and-technologies/renewables> (accessed 4.11.2022)
- [2] D. Song, B. Jia, H. Jiao: Review of Renewable Energy Subsidy System in China, *Energies* 2022, 15(19), 7429, <https://doi.org/10.3390/en15197429>
- [3] O. O. Apeh, E. L. Meyer, O. K. Overen: Contributions of Solar Photovoltaic Systems to Environmental and Socioeconomic Aspects of National Development—A Review, *Energies* 2022, 15, 5963, <https://doi.org/10.3390/en15165963>
- [4] Directive 2009/28/EC of the European Parliament and of the Council of 23 April 2009 on the Promotion of the Use of Energy from Renewable Sources and Amending and Subsequently Repealing Directives 2001/77/EC and 2003/30/EC. 2009, Available online: <https://eur-lex.europa.eu/legal-content/EN/ALL/?uri=CELEX%3A32009L0028> (accessed 5 Nov. 2022)
- [5] New Green Savings Programme—Directive No. 1 NZU 2014 and Its Annexes. Czech Republic, 2014, Available online: <http://www.novazelenausporam.cz/> (accessed 5 Nov. 2022) (In Czech)
- [6] Czech Energy Regulatory Office: Decree No 16/2016: Conditions for Connection to the Public Electricity Grid in Czech Language; Czech Energy Regulatory Office: Jihlava, Czech Republic, 2016
- [7] P. A. Cordero, J. L. Garcia, F. Jurado: Optimization of an Off-Grid Hybrid System Using Lithium Ion Batteries, *Acta Polytechnica Hungarica*, Vol. 17, No. 3, 2020, pp.185-206

- [8] Solar association: Annual reports. Available online: <https://www.solarniasociace.cz/cs/o-nas/vyrocnni-zpravy> (accessed 5 November 2022) (In Czech)
- [9] EN 50160 - Voltage characteristics of electricity supplied by public electricity networks, 2010
- [10] O. Gandhi, D. S. Kumar, C. D. Rodríguez-Gallegos, D. Srinivasan: Review of power system impacts at high PV penetration Part I: Factors limiting PV penetration, *Solar Energy*, Vol. 210, November 2020, pp. 181-201
- [11] D. Pejovski, K. Najdenkoski, M. Digalovski: Impact of different harmonic loads on distribution transformers, *Procedia Engineering*, Volume 202, 2017, pp. 76-87, ISSN 1877-7058, <https://doi.org/10.1016/j.proeng.2017.09.696>
- [12] M. Kolcun, A. Gawlak, M. Kornatka, Z. Conka: Active and Reactive Power Losses in Distribution Transformers, *Acta Polytechnica Hungarica*, Vol. 17, No. 1, 2020, pp. 161-174
- [13] Commission Regulation (EU) 2016/631 of 14 April 2016 Establishing a Network Code on Requirements for Grid Connection of Generators (NC RfG). 2016. Available online: <https://eur-lex.europa.eu/legal-content/CS/TXT/PDF/?uri=CELEX:32016R0631&from=LT> (accessed on 6 November 2020)
- [14] EN 50549-1 - Requirements for generating plants to be connected in parallel with distribution networks - Part 1: Connection to a LV distribution network - Generating plants up to and including Type B, 2019
- [15] EN 50549-2 - Requirements for generating plants to be connected in parallel with distribution networks - Part 2: Connection to a MV distribution network - Generating plants up to and including Type B, 2019
- [16] Energy Regulatory Office, “Rules for operation of distribution power system Annex 4: Rules for parallel operation of generators and accumulation devices with the distribution system operator's power system”, June 2021
- [17] Decision No 768/2008/EC of the European Parliament and of the Council of 9 July 2008 on a common framework for the marketing of products, and repealing Council Decision 93/465/EEC. 2008, Available online: <https://eur-lex.europa.eu/legal-content/EN/TXT/?uri=CELEX:32008D0768>
- [18] P. Mastný, M. Vojtek, J. Morávek, M. Vrána, J. Klusáček: Validation of PV Inverters Frequency Response Using Laboratory Test Platform, 2020 21<sup>st</sup> International Scientific Conference on Electric Power Engineering (EPE), 2020, pp. 1-5, doi: 10.1109/EPE51172.2020.9269247

- [19] M. Vojtek, P. Mastný, J. Morávek, J. Drápela, M. Vrána: Verification of Photovoltaic Inverters Properties and Their Compliance With Grid Code Requirements in the Czech Republic, Proceedings of the 11<sup>th</sup> International Scientific Symposium on Electrical Power Engineering, ELEKTROENERGETIKA 2022, 12-14.9.2022, pp. 204-209
- [20] J. Drapela, J. Moravek, M. Vrana, P. Mastny: Power Generating Modules Field Testing Concepts for Verification of Compliance with Operational Requirements, 2020 21<sup>st</sup> International Scientific Conference on Electric Power Engineering (EPE), 2020, pp. 1-6, doi: 10.1109/EPE51172.2020.9269230
- [21] P. Mastny, J. Moravek, J. Drapela, M. Vrana, M. Vojtek: Problems of verification of operating parameters of DC/AC inverters and their integration into the distribution system in the Czech Republic, CIRED Porto Workshop 2022: E-mobility and power distribution systems, 2022, pp. 304-308, doi: 10.1049/icp.2022.0716
- [22] J. Dvoracek, J. Drapela, J. Moravek, M. Vojtek, P. Toman: On Verification of Power Generating Modules Compliance with Network Requirements, 2022 22<sup>nd</sup> International Scientific Conference on Electric Power Engineering (EPE), 2022, pp. 1-6, doi: 10.1109/EPE54603.2022.9814092
- [23] L. Yu-Jen, L. Pei-Hsiu, L. Hong-Hsun: Grid-Connected PV Inverter Test System for Solar Photovoltaic Power System Certification. In Proceedings of the IEEE PES General Meeting Conference & Exposition, National Harbor, MD, USA, 27-31 July 2014
- [24] K. Chmielowiec, Ł. Topolski, A. Piszczek, Z. Hanzelka: Photovoltaic Inverter Profiles in Relation to the European Network Code NC RfG and the Requirements of Polish Distribution System Operators. *Energies* 2021, 14, 1486, <https://doi.org/10.3390/en14051486>

# Data Driven, Additive Fault Detection for Wind Turbines

Dušan Krokavec\*, Anna Filasová

Department of Cybernetics and Artificial Intelligence, Faculty of Electrical Engineering and Informatics, Technical University of Košice

Letná 9, 042 00 Košice, Slovakia

e-mail: {dusan.krokavec, anna.filasova}@tuke.sk

\*Corresponding author

---

*Abstract: This paper covers an approach for fault residuals construction, when carrying out the data driven techniques. The method is based on the system input and output data and is built on a difference between data of a “normal” and a “faulty” system behavior. The research evaluates the performance of the structures, based on the subspace identification technique, to highlight the acceptable usefulness of the resulting data driven approach. Following the same lines, it delineates the connection to input/output data and provides an approach to computation of the parameterized data matrices. The principle is applied directly in analysis of the data generated by the wind turbine model.*

*Keywords: fault detection; fault residuals; data driven techniques; wind turbine models*

---

## 1 Introduction

Beginning in the 70s of the last century, the analytical redundancy approach, instead of hardware redundancy, forces the concept of fault detection filters, constructed on the observations derived from the system measurements using Kalman filters [1] and system state observers [2]. The principal focus points on the fault detection and diagnosis were oriented on the chemical and petrochemical processes [3], the first applications of the data-driven methods are also linked to this industry area [4]. Thus, in the main context, the fault detection and isolation (FDI) part of such diagnostic systems have to give an efficient solution with small fault detection time delays.

Many models based FDI techniques have been proposed including the above mentioned Kalman filters [5], unknown input observers [6] and  $H_\infty/H_2$  observer-based residual filter schemes [7]. The underlying idea behind the model based FDI is to use a mathematical model of the system as the source of redundant information and to produce the state estimate-based fault residuals by using the

systems measured outputs. For all representations based on system models the fundamental question is the system observability. The disadvantage of this approach is the need for an accurate model of the process.

An alternative approach known as data driven FDI (DD FDI) uses a collection of measured data to discover patterns related to the normal and faulty system behavior. The data driven FDIs prevalingly reflect results in machine learning, computational intelligence and data mining. The most popular DD FDI techniques are data feature-based prediction techniques using the nonlinear time series based on the projection-based techniques [8], prediction principle [9], the correlation analysis and Bayesian inference principle [10] and the fault feature extraction and classification using computational intelligence principle [11]. The additive fault estimators can also be considered as data driven procedures, usually applicable in the case of poor analytical knowledge of the system dynamics and external disturbances [12] [13].

The wind turbine technology is one of the appropriate ways for increased use of renewable energy. Thus, in order to improve a wind turbine behavior and reliability, faults prevention in the parts of the wind turbine and fault tolerant control stay relevant objectives. A way to ensure these tasks consists in introducing advanced fault detection, isolation, and accommodation schemes [14-15], where FDIs are designed to estimate the filter speed by using a bank of state observers and bank of unknown input observers, respectively. To improve diagnosis of faults the wind farm level can be applied, when a wind turbine is considered in comparison to another turbine of the wind farm [16].

The starting data-driven solution in the wind turbine diagnosis relies on Takagi–Sugeno (T-S) fuzzy models that are derived from a clustering c-means algorithm, followed by an identification procedure [17]. To achieve maximization of the wind power extraction, T-S fuzzy models of reduced dimension are proposed [18]. The power of the approach can be amplified when combining the wind power extraction T-S models by DD FDI and the weighting two or more metrics related with analytical FDI [19] [20]. In all schemes, a properly large data set should be available as a-priori knowledge to train the structure in the fault-free case.

In this paper a basic ground is taken on the data driven approaches, based on subspace identification methods, for additive fault detection of wind turbines. Since the system state-space description projects the system state into output variables, it is a natural way for constructive data driven approaches to suppress the system model description and to identify only the parameterized matrices of system data. This leads to formulas for the matrix pseudo inverse operations on the predetermined data matrices that seems to be basic. Of course, this application of the orthogonal complement of non-square data matrices for identification of parameterized matrices of the system is not new and the presented way seems to be only a new adaptation.

The paper is organized as follows. Ensuing introduction in Sect. 1 and continuing by the system description using lagged variables in Sect. 2, constructions of data matrix null spaces are given in Sect. 3. The fault residuals generation is analyzed in Sect. 4 and suppression of noise effects is explained in Sect. 5. In the task relation, Sect. 6 describes substantial details in a reference model of wind turbines and applicability of the proposed method using benchmark model parameters is in Sect. 7. Finally, in Sect. 8, some prioritized concluding remarks are presented.

For sake of convenience, throughout this paper used notations reflect usual conventionality so that  $\mathbf{x}^T$ ,  $\mathbf{X}^T$  mean transpose of the vector  $\mathbf{x}$  and the matrix  $\mathbf{X}$ , the notation  $\mathbf{X}^\dagger$  denotes the Moore-Penrose pseudo inverse of a non-square matrix,  $\mathbf{X}^\perp$  reflects the orthogonal complement of a non-square matrix  $\mathbf{X}$ ,  $\mathbf{I}_n$  is the  $n^{\text{th}}$  order identity matrix and  $\mathbb{R}^{n \times r}$  signifies the set  $n \times r$  real matrices.

## 2 Lagged Variables

Considering that the task is focuses on developing the FDI method in the data-driven fashion, the linear discrete-time model of the square system is used in the standard state space representation given by

$$\mathbf{q}(i+1) = \mathbf{F}\mathbf{q}(i) + \mathbf{G}\mathbf{u}(i) + \mathbf{v}(i) \quad (1)$$

$$\mathbf{y}(i) = \mathbf{C}\mathbf{q}(i) + \mathbf{w}(i) \quad (2)$$

where  $\mathbf{q}(i) \in \mathbb{R}^n$  is the state vector,  $\mathbf{u}(i) \in \mathbb{R}^{r_u}$ ,  $\mathbf{y}(i) \in \mathbb{R}^m$  is the input and the output vector, respectively, while  $\mathbf{F} \in \mathbb{R}^{n \times n}$ ,  $\mathbf{G} \in \mathbb{R}^{n \times r_u}$ ,  $\mathbf{C} \in \mathbb{R}^{m \times n}$ . The system is corrupted by the stochastic disturbances  $\mathbf{v}(i) \in \mathbb{R}^n$ ,  $\mathbf{w}(i) \in \mathbb{R}^m$ , which are zero means and normally distributed white noise.

Taking (1), (2) the following can be performed for the square system ( $r_u = m$ )

$$\begin{aligned} \mathbf{y}(i) &= \mathbf{C}\mathbf{q}(i) + \mathbf{w}(i) \\ \mathbf{y}(i+1) &= \mathbf{C}\mathbf{F}\mathbf{q}(i) + \mathbf{C}\mathbf{G}\mathbf{u}(i) + \mathbf{C}\mathbf{v}(i) + \mathbf{w}(i) \\ &\vdots \\ \mathbf{y}(i+s-1) &= \mathbf{C}\mathbf{F}^{s-1}\mathbf{q}(i) + [\mathbf{C}\mathbf{F}^{s-2}\mathbf{G} \ \dots \ \mathbf{C}\mathbf{G} \ \mathbf{0}]\mathbf{u}_o(i) + \\ &\quad + [\mathbf{C}\mathbf{F}^{s-2} \ \dots \ \mathbf{C} \ \mathbf{0}]\mathbf{v}_o(i) + \mathbf{w}(i+s-1) \end{aligned} \quad (3)$$

writing with

$$\mathbf{u}_o(i) = \begin{bmatrix} \mathbf{u}(i) \\ \vdots \\ \mathbf{u}(i+s-1) \end{bmatrix}, \quad \mathbf{v}_o(i) = \begin{bmatrix} \mathbf{v}(i) \\ \vdots \\ \mathbf{v}(i+s-1) \end{bmatrix}, \quad \mathbf{w}_o(i) = \begin{bmatrix} \mathbf{w}(i) \\ \vdots \\ \mathbf{w}(i+s-1) \end{bmatrix} \quad (4)$$

which can be rewritten as:

$$\mathbf{y}_o(i) = \mathbf{P}\mathbf{q}(i) + \mathbf{R}\mathbf{u}_o(i) + \mathbf{S}\mathbf{v}_o(i) + \mathbf{w}_o(i) \quad (5)$$

where,

$$\mathbf{y}_o(i) = \begin{bmatrix} \mathbf{u}(i) \\ \vdots \\ \mathbf{u}(i+s-1) \end{bmatrix}, \quad \mathbf{R} = \begin{bmatrix} \mathbf{0} & \mathbf{0} & \cdots & \mathbf{0} & \mathbf{0} \\ \mathbf{CG} & \mathbf{0} & \cdots & \mathbf{0} & \mathbf{0} \\ \vdots & \vdots & \ddots & \vdots & \vdots \\ \mathbf{CF}^{s-2}\mathbf{G} & \mathbf{CF}^{s-3}\mathbf{G} & \cdots & \mathbf{CG} & \mathbf{0} \end{bmatrix} \quad (6)$$

$$\mathbf{P} = \begin{bmatrix} \mathbf{C} \\ \mathbf{CF} \\ \vdots \\ \mathbf{CF}^{s-1} \end{bmatrix}, \quad \mathbf{S} = \begin{bmatrix} \mathbf{0} & \mathbf{0} & \cdots & \mathbf{0} & \mathbf{0} \\ \mathbf{C} & \mathbf{0} & \cdots & \mathbf{0} & \mathbf{0} \\ \vdots & \vdots & \ddots & \vdots & \vdots \\ \mathbf{CF}^{s-2} & \mathbf{CF}^{s-3} & \cdots & \mathbf{C} & \mathbf{0} \end{bmatrix} \quad (7)$$

and  $\mathbf{y}_o(i), \mathbf{u}_o(i), \mathbf{w}_o(i) \in \mathbb{R}^{sm}$ ,  $\mathbf{v}_o(i) \in \mathbb{R}^{sn}$ ,  $\mathbf{P} \in \mathbb{R}^{sm \times n}$ ,  $\mathbf{R} \in \mathbb{R}^{sm \times sm}$ ,  $\mathbf{S} \in \mathbb{R}^{sm \times sm}$ .

Thus, applying the input and output data sets, the related data structures can be investigated, defined as:

$$\mathbf{y}_g(i) = \begin{bmatrix} \mathbf{y}(i-r) \\ \vdots \\ \mathbf{y}(i-1) \end{bmatrix}, \quad \mathbf{u}_g(i) = \begin{bmatrix} \mathbf{u}(i-r) \\ \vdots \\ \mathbf{u}(i-1) \end{bmatrix}, \quad \mathbf{z}_g(i) = \begin{bmatrix} \mathbf{y}_g(i) \\ \mathbf{u}_g(i) \end{bmatrix}, \quad \mathbf{z}_o(i) = \begin{bmatrix} \mathbf{y}_o(i) \\ \mathbf{u}_o(i) \end{bmatrix} \quad (8)$$

where  $\mathbf{z}_g(i) \in \mathbb{R}^{2rm}$ ,  $\mathbf{z}_o(i) \in \mathbb{R}^{2sm}$  and  $s \geq r > n$

The structural relations (5) can be parameterized such that:

$$\mathbf{Y}_{o,p} = \mathbf{P}\mathbf{Q}_{o,p} + \mathbf{R}\mathbf{U}_{o,p} + \mathbf{D}_{o,p} \quad (9)$$

where,

$$\mathbf{Y}_{o,p} = [\mathbf{y}_o(i) \cdots \mathbf{y}_o(i+p-1)], \quad \mathbf{Q}_{o,p} = [\mathbf{q}(i) \cdots \mathbf{q}(i+p-1)] \quad (10)$$

$$\mathbf{U}_{o,p} = [\mathbf{u}_o(i) \cdots \mathbf{u}_o(i+p-1)], \quad \mathbf{V}_{o,p} = [\mathbf{v}_o(i) \cdots \mathbf{v}_o(i+p-1)] \quad (11)$$

$$\mathbf{D}_{o,p} = [\mathbf{S}\mathbf{V}_{o,p} \quad \mathbf{W}_{o,p}], \quad \mathbf{W}_{o,p} = [\mathbf{w}_o(i) \cdots \mathbf{w}_o(i+p-1)] \quad (12)$$

and  $\mathbf{Q}_{o,p} \in \mathbb{R}^{sm \times p}$ ,  $\mathbf{Y}_{o,p}, \mathbf{U}_{o,p} \in \mathbb{R}^{sm \times pm}$ ,  $\mathbf{D}_{o,p} \in \mathbb{R}^{sm \times 2p}$ ,  $p \geq s \geq r > n$

When the new samples  $\mathbf{y}_o(i)$  and  $\mathbf{u}_o(i)$  are available, updated matrices are formulated by appending the new columns on the right and deleting the first columns in  $\mathbf{Y}_{o,p}, \mathbf{U}_{o,p}$

**Corollary 1** The subspace method aided data-driven fault detection can be detailed for systems with the additive faults, including the actuator faults. This application requests to alter the state equation (1) as:

$$\mathbf{q}(i+1) = \mathbf{F}\mathbf{q}(i) + \mathbf{G}\mathbf{u}(i) + \mathbf{H}\mathbf{f}(i) + \mathbf{v}(i), \quad \mathbf{f}(i) \in \mathbb{R}^{r_f}, \mathbf{H} \in \mathbb{R}^{n \times r_f} \quad (13)$$

$$\mathbf{f}_o(i) = \begin{bmatrix} \mathbf{f}(i) \\ \vdots \\ \mathbf{f}(i+s-1) \end{bmatrix}, \quad \mathbf{R}_f = \begin{bmatrix} \mathbf{0} & \mathbf{0} & \cdots & \mathbf{0} & \mathbf{0} \\ \mathbf{CH} & \mathbf{0} & \cdots & \mathbf{0} & \mathbf{0} \\ \vdots & \vdots & \ddots & \vdots & \vdots \\ \mathbf{CF}^{s-2}\mathbf{H} & \mathbf{CF}^{s-3}\mathbf{H} & \cdots & \mathbf{CH} & \mathbf{0} \end{bmatrix} \quad (14)$$

and modifies the matrix  $\mathbf{D}_o$  as follows, when applying in (9),

$$\mathbf{D}_{o,p} = [\mathbf{R}_f\mathbf{f}_o(i) + \mathbf{S}\mathbf{v}_o(i) + \mathbf{w}_o(i) \cdots \mathbf{R}_f\mathbf{f}_o(i+p-1) + \mathbf{S}\mathbf{v}_o(i+p-1) + \mathbf{w}_o(i+p-1)] \quad (15)$$

### 3 Construction of Data Matrix Null Spaces

The presented method is built on non-square matrices, which gives the possibility to eliminate the column redundancy by principle of the matrix null space.

**Lemma 1** The orthogonal projector onto the kernel of a non-square matrix  $\mathbf{L} \in \mathbb{R}^{a \times b}$ ,  $b > a$ , (an orthogonal complement of  $\mathbf{L}$ ) takes the form:

$$\mathbf{L}^\perp = \mathbf{I}_b - \mathbf{L}^{\square 1} \mathbf{L} \cong \mathbf{0} \quad (16)$$

Where,

$$\mathbf{L}^{\square 1} = \mathbf{L}^T (\mathbf{L} \mathbf{L}^T)^{-1} \quad (17)$$

is the Moore-Penrose pseudo-inverse of  $\mathbf{L}$ , where,  $\mathbf{L}^{\square 1} \in \mathbb{R}^{b \times a}$

**Remark 1** Noting that for a non-square matrix it yields also that  $\mathbf{L} = \mathbf{L}$ , then multiplying this equality from the left-hand side by the identity matrix  $\mathbf{I}_a$  it yields:

$$\mathbf{L} = \mathbf{I}_a \mathbf{L} = \mathbf{L} \mathbf{I}_b = \mathbf{L} \mathbf{L}^T (\mathbf{L} \mathbf{L}^T)^{-1} \mathbf{L} \quad (18)$$

which implies,

$$\mathbf{I}_b = \mathbf{L}^T (\mathbf{L} \mathbf{L}^T)^{-1} \mathbf{L} = \mathbf{L}^{\square 1} \mathbf{L} \quad (19)$$

Rewriting the equality (19) as:

$$\mathbf{L} = \mathbf{L} \mathbf{L}^{\square 1} \mathbf{L} \quad (20)$$

it can be derived that:

$$\mathbf{L}(\mathbf{I}_b - \mathbf{L}^T (\mathbf{L} \mathbf{L}^T)^{-1} \mathbf{L}) = \mathbf{L}(\mathbf{I}_b - \mathbf{L}^{\square 1} \mathbf{L}) = \mathbf{L} \mathbf{L}^\perp \cong \mathbf{0} \quad (21)$$

which defines (16).

**Lemma 2** Singular value decomposition (SVD) of a non-square matrix  $\mathbf{L} \in \mathbb{R}^{a \times b}$ ,  $b > a$ , constructs the matrix relation:

$$\mathbf{M}^T \mathbf{L} \mathbf{N} = \mathbf{\Sigma} \quad (22)$$

where,

$$\mathbf{M} = [\mathbf{m}_1 \cdots \mathbf{m}_a], \quad \mathbf{N} = [\mathbf{n}_1 \cdots \mathbf{n}_b], \quad \mathbf{M} \in \mathbb{R}^{a \times a}, \quad \mathbf{N} \in \mathbb{R}^{b \times b} \quad (23)$$

are the orthogonal matrices of the left and the right singular vectors of  $\mathbf{L}$  and

$$\mathbf{\Sigma} = \begin{bmatrix} \sigma_1 & & & & & \\ & \sigma_2 & & & & \\ & & \ddots & & & \\ & & & \mathbf{0}_{a,b-a} & & \\ & & & & \sigma_a & \\ & & & & & \end{bmatrix} \quad (24)$$

where  $\sigma_l, l=1, \dots, a$  are the singular variables of  $\mathbf{L}$ , generally ordered in such a way that  $\sigma_1 \geq \sigma_2 \geq \dots \geq \sigma_a \geq 0$ .

**Remark 2** Since (22) can be rewritten as:

$$\mathbf{M}^T \mathbf{L} [\mathbf{N}_1 \ \mathbf{N}_2] = \mathbf{\Sigma}, \quad \mathbf{N}_1 \in \mathbb{R}^{b \times a}, \mathbf{N}_2 \in \mathbb{R}^{b \times (b-a)} \quad (25)$$

the structure of  $\mathbf{\Sigma}$  implies that:

$$\mathbf{L} \mathbf{N}_2 = \mathbf{0}_{a, b-a} \quad (26)$$

that is, the orthogonal complement of  $\mathbf{L}$  is  $\mathbf{N}_2$

**Remark 3** To given  $\mathbf{L}$  it can be constructed the square matrix  $\mathbf{L} \mathbf{L}^T$  and for the eigenvalue structure of  $\mathbf{L} \mathbf{L}^T$  it yields:

$$\mathbf{L} \mathbf{L}^T \mathbf{s}_l = \rho_l \mathbf{s}_l, \quad \mathbf{u}_l^T \mathbf{L} \mathbf{L}^T = \rho_l \mathbf{u}_l^T, \quad l = 1, \dots, a \quad (27)$$

where  $\rho_l$  it the  $l^{\text{th}}$  eigenvalue of  $\mathbf{L} \mathbf{L}^T$ ,  $\mathbf{s}_l$  it the  $l^{\text{th}}$  right eigenvector of  $\mathbf{L} \mathbf{L}^T$  and  $\mathbf{u}_l^T$  it the  $l^{\text{th}}$  left eigenvector of  $\mathbf{L} \mathbf{L}^T$ . Multiplying the left side of (27) by  $\mathbf{u}_h^T$  it has to be:

$$\mathbf{u}_h^T \mathbf{L} \mathbf{L}^T \mathbf{s}_l = \rho_h \mathbf{u}_h^T \mathbf{s}_l = \rho_l \mathbf{u}_h^T \mathbf{s}_l \quad (28)$$

which can be satisfied only if:

$$\mathbf{u}_h^T \mathbf{s}_l = \begin{cases} 1, & h=l, \\ 0, & h \neq l. \end{cases} \quad h, l = 1, \dots, a \quad (29)$$

that is the left and the right eigenvectors are orthonormal. Consequently (28) can be written as:

$$\rho_h \mathbf{u}_h^T \mathbf{s}_l = \mathbf{u}_h^T \mathbf{L} \mathbf{L}^T \mathbf{s}_l = \mathbf{u}_h^T \mathbf{L} \mathbf{L}^T \mathbf{s}_l \frac{\|\mathbf{L}^T \mathbf{s}_l\|}{\|\mathbf{L}^T \mathbf{s}_l\|} = \mathbf{u}_h^T \mathbf{L} \mathbf{v}_l \sqrt{\rho_l} = \mathbf{u}_h^T \mathbf{L} \mathbf{v}_l \sigma_l \quad (30)$$

which can be satisfied only if:

$$\mathbf{u}_h^T \mathbf{s}_l = \begin{cases} 1, & h=l, \\ 0, & h \neq l, \\ 0, & l > a, \end{cases} \quad h, l = 1, \dots, a \quad (31)$$

and where,

$$\mathbf{v}_l = \frac{\mathbf{L}^T \mathbf{s}_l}{\|\mathbf{L}^T \mathbf{s}_l\|}, \quad \sqrt{\rho_l} = \|\mathbf{L}^T \mathbf{s}_l\|, \quad \sqrt{\rho_l} = \sigma_l \quad (32)$$

Then (30) defines (22).

To find the fault residual filter construction and structure, the following section is especially offered.

## 4 Fault Residuals

A general fault diagnosis can be performed using residual signal that represents a deviation from standard operating conditions and can be generated by comparing, for example, a model output with the actual system output.

The data-driven fault residuals must be generated from the system input and output data using the lagged variables.

Rewriting (9) as:

$$\mathbf{Y}_{o,p} - \mathbf{R}\mathbf{U}_{o,p} = \mathbf{P}\mathbf{Q}_{o,p} + \mathbf{D}_{o,p} \quad (33)$$

and multiplying (33) from the left-hand side by  $\mathbf{P}^\perp$  (constructed by (16) to eliminate the effect of  $\mathbf{Q}_{o,p}$ ), it yields:

$$\mathbf{P}^\perp(\mathbf{Y}_{o,p} - \mathbf{R}\mathbf{U}_{o,p}) = \mathbf{P}^\perp\mathbf{D}_{o,p} \quad (34)$$

and the fault residuals can be defined as:

$$\mathbf{\Omega}_{o,p} = \mathbf{P}^\perp\mathbf{Y}_{o,p} - \mathbf{P}^\perp\mathbf{R}\mathbf{U}_{o,p} \quad (35)$$

$$\omega_o(i) = \mathbf{P}^\perp\mathbf{y}_o(i) - \mathbf{P}^\perp\mathbf{R}\mathbf{u}_o(i) \quad (36)$$

Thus, the residual generation can be achieved if  $\mathbf{P}^\perp$ ,  $\mathbf{P}^\perp\mathbf{R}$  can be acquired from the system input and output data.

To use the residual vector  $\omega_o(i)$  at the time instant step  $i$ , the statistic test has to be applied, based on the following covariance matrix computed in the fault-free case.

$$\mathbf{\Xi}_o = \frac{1}{p-1} \sum_{j=1}^p \mathbf{\Omega}_{o,p}(j)\mathbf{\Omega}_{o,p}^T(j) \quad (37)$$

to give the possibility of generating the fault occurrence threshold as:

$$t_\omega = \mathbf{\omega}_o^T(i)\mathbf{\Xi}_o^{-1}\mathbf{\omega}_o(i) \quad (38)$$

when defining the detection logic:

$$\begin{cases} t_\omega < t_h, & \text{no fault} \\ t_\omega \geq t_h, & \text{a fault} \end{cases} \quad (39)$$

where  $t_h \in \mathbb{R}_+$  is a defined threshold.

The presented approach takes advantage of the actual system input and output data sets to generate a discrepancy (residuals) that are indicative as a potential additive fault occurrence.

It can be underlined that the data-driven technique addresses mostly anticipated fault conditions only.

## 5 Suppression of Noise Effects

When the system is corrupted by the system and measurement noise, both taking Gaussian white noise properties, the instrumental variable  $\mathbf{z}_o(i)$  can be exploited to suppress noise effects. Since in this case the past data  $\mathbf{z}_g(i)$  are uncorrelated with the future noise realizations then, using (12):

$$\lim_{p \rightarrow \infty} \frac{1}{p} \mathbf{D}_{o,p} \mathbf{Z}_{g,p}^T = \lim_{p \rightarrow \infty} \frac{1}{p} (\mathbf{S} \mathbf{V}_{o,p} \mathbf{Z}_{g,p}^T + \mathbf{W}_{o,p} \mathbf{Z}_{g,p}^T) = \mathbf{0} \quad (40)$$

where,

$$\mathbf{Z}_{g,p} = \begin{bmatrix} \mathbf{Y}_{g,p} \\ \mathbf{U}_{g,p} \end{bmatrix} = \begin{bmatrix} \mathbf{y}_g(i-1) & \cdots & \mathbf{y}_g(i-p) \\ \mathbf{u}_g(i-1) & \cdots & \mathbf{u}_g(i-p) \end{bmatrix} \quad (41)$$

The following remark shows the computation of the orthogonal complement  $\mathbf{P}^\perp$

**Remark 4** Constructing according to (16) the orthogonal complement  $\mathbf{U}_{o,p}^\perp$  then it yields for the auxiliary variable  $\Phi$

$$\Phi = \lim_{p \rightarrow \infty} \frac{1}{p} (\mathbf{Y}_{o,p} - \mathbf{R} \mathbf{U}_{o,p}) \mathbf{U}_{o,p}^\perp \mathbf{Z}_{g,p}^T = \lim_{p \rightarrow \infty} \frac{1}{p} \mathbf{Y}_{o,p} \mathbf{U}_{o,p}^\perp \mathbf{Z}_{g,p}^T = \lim_{p \rightarrow \infty} \frac{1}{p} \mathbf{P} \mathbf{Q}_{o,p} \mathbf{U}_{o,p}^\perp \mathbf{Z}_{g,p}^T \quad (42)$$

and the result of SVD to  $\Phi$ , when exploiting the property (25), means:

$$\mathbf{\Gamma}^T \Phi [\mathbf{\Psi}_1 \ \mathbf{\Psi}_2] = \mathbf{\Sigma}_\Phi \quad (43)$$

which defines that  $\mathbf{P}^\perp$  can be computed as:

$$\mathbf{P}^\perp = \mathbf{\Psi}_2 \quad (44)$$

Finally, since (40) implies for (34) that:

$$\mathbf{0} = \mathbf{P}^\perp \lim_{p \rightarrow \infty} \frac{1}{p} (\mathbf{Y}_{o,p} \mathbf{Z}_{g,p}^T - \mathbf{R} \mathbf{U}_{o,p} \mathbf{Z}_{g,p}^T) \quad (45)$$

(45) means that:

$$\mathbf{P}^\perp \lim_{p \rightarrow \infty} \frac{1}{p} \mathbf{Y}_{o,p} \mathbf{Z}_{g,p}^T = \mathbf{P}^\perp \mathbf{R} \lim_{p \rightarrow \infty} \frac{1}{p} \mathbf{U}_{o,p} \mathbf{Z}_{g,p}^T \quad (46)$$

and using the notations:

$$\mathbf{\Phi}_{YZ} = \lim_{p \rightarrow \infty} \frac{1}{p} \mathbf{Y}_{o,p} \mathbf{Z}_{g,p}^T, \quad \mathbf{\Phi}_{UZ} = \lim_{p \rightarrow \infty} \frac{1}{p} \mathbf{U}_{o,p} \mathbf{Z}_{g,p}^T \quad (47)$$

then, with the pseudoinverse of the matrix  $\mathbf{\Phi}_{UZ}$  it can be computed that:

$$\mathbf{P}^\perp \mathbf{R} = \mathbf{P}^\perp \mathbf{\Phi}_{YZ} \mathbf{\Phi}_{UZ}^{\square 1} \quad (48)$$

Thus, all the parameters are now known to construct (35) when computing the fault residuals from the system input and system output data.

Note, in practice, the limit to infinity in (40), (42), (47) is replaced by a substantially large value of  $p$ .

## 6 Reference Wind Turbine Model

The proposed reference linear model can be given by the model of the three-blade horizontal wind turbine [21].

In this scheme the aerodynamic torque is given as [22]:

$$\tau_r(t) = \frac{1}{2} \rho \pi r^3 C_q(\lambda(t), \beta(t)) v^2(t) \quad (49)$$

where  $v(t)$  is the actual speed of wind [m.s<sup>-1</sup>],  $r$  is the rotor radius [m],  $C_q(*)$  is the torque coefficient and  $\rho$  is the air density [kg.m<sup>-3</sup>]. Specifically,  $C_q(*)$  depends on the tip speed ratio  $\lambda(t)$  [rad] between the tangential speed of the tip of a blade and the actual speed of wind and the blades pitch angle  $\beta(t)$  [rad], where:

$$C_q(\lambda(t), \beta(t)) = \frac{C_p(\lambda(t), \beta(t))}{\beta(t)}, \quad \lambda(t) = \frac{r \omega_r(t)}{v(t)} \quad (50)$$

whilst  $\omega_r(t)$  is the rotor angular speed [rad.s<sup>-1</sup>] and  $C_p(\lambda(t), \beta(t))$  is a rotor torque coefficient.

The turbine speed is controlled to track the reference trajectory  $\omega_{rt}(t)$ , to maintain the tip-speed ratio at its optimal value  $\lambda_o$ , computed from the relation:

$$\omega_{rt}(t) = \lambda(t) \frac{v(t)}{r} \quad (51)$$

Thus, using  $\lambda(t)$  it yields:

$$\tau_r(t) = \frac{1}{2 \lambda^2(t)} \rho \pi r^5 C_q(\lambda(t), \beta(t)) \omega_r^2(t) \quad (52)$$

The two-mass drive train equations take the forms:

$$J_r \frac{d\omega_r(t)}{dt} = \tau_r(t) - (b_{dt} + b_r) \omega_r(t) - k_{dt} \vartheta(t) + \frac{b_{dt}}{N_g} \omega_g(t) \quad (53)$$

$$J_g \frac{d\omega_g(t)}{dt} = \frac{\mu_{dt} k_{dt}}{N_g} \vartheta(t) + \frac{\mu_{dt} b_{dt}}{N_g} \omega_r(t) - \left( \frac{\mu_{dt} b_{dt}}{N_g^2} + b_g \right) \omega_g(t) - \tau_g(t) \quad (54)$$

$$\frac{d\vartheta(t)}{dt} = \omega_r(t) - \frac{1}{N_g} \omega_g(t) \quad (55)$$

where  $\omega_r(t)$  is the rotor angular speed [rad.s<sup>-1</sup>],  $\omega_g(t)$  is the generator rotating speed [rad.s<sup>-1</sup>],  $\vartheta(t)$  is the torsion angle [rad],  $\tau_g(t)$  is the aerodynamic torque [kg.m<sup>2</sup>.s<sup>-2</sup>],  $J_r$  is rotor inertia moment [kg.m<sup>2</sup>],  $N_g$  is gear ration,  $b_{dt}$  is the torsion damping coefficient [N.m.s.rad<sup>-1</sup>],  $b_r$  is rotor external damping [N.m.s.rad<sup>-1</sup>],  $k_{dt}$  is the torsion stiffness [N.m.rad<sup>-1</sup>],  $b_g$  is the generator external damping [N.m.s.rad<sup>-1</sup>] and  $\mu_{dt}$  is efficiency of drive train.

The hydraulic pitch is modeled by the differential equation of the form [23]

$$\frac{d^2 \beta(t)}{dt^2} + 2\zeta\omega_n \frac{d\beta(t)}{dt} + \omega_n^2 \beta(t) = \omega_n^2 \beta_r(t) \quad (56)$$

while  $\beta(t)$  is the measured pitch angle [rad],  $\beta_r(t)$  is the reference pitch angle [rad],  $\omega_n$  is the pitch filter natural frequency [rad.s<sup>-1</sup>],  $\zeta$  is the damping factor and the generator and converter dynamics are modeled by the first-order differential equation [24]:

$$\frac{d\tau_g(t)}{dt} + \alpha\tau_g(t) = \alpha\tau_{gr}(t) \quad (57)$$

where  $\tau_g(t)$  is the generator torque [Nm],  $\tau_{gr}(t)$  is the generator torque reference [Nm] and  $\alpha$  is the generator and converter time-constant parameter [s<sup>-1</sup>].

Considering the continuou-time system state-space description of the reference wind turbine model of the following form:

$$\frac{d\mathbf{q}(t)}{dt} = \mathbf{A}\mathbf{q}(t) + \mathbf{B}\mathbf{u}(t), \quad \mathbf{y}(t) = \mathbf{C}\mathbf{q}(t) \quad (58)$$

then the used vector variables and the reference model matrix parameters are defined as follows:

$$\mathbf{u}^T(t) = [\tau_{gr}(t) \ \beta_r(t)], \quad \mathbf{y}^T(t) = [\omega_r(t) \ \omega_g(t)] \quad (59)$$

$$\mathbf{q}^T(t) = [\omega_r(t) \ \omega_g(t) \ \mathcal{G}_\square(t) \ \dot{\beta}(t) \ \beta(t) \ \tau_g(t)] \quad (60)$$

$$\mathbf{B}^T = \begin{bmatrix} 0 & 0 & 0 & 0 & 0 & \alpha \\ 0 & 0 & 0 & \omega_n & 0 & 0 \end{bmatrix}, \quad \mathbf{C} = \begin{bmatrix} 1 & 0 & 0 & 0 & 0 & 0 \\ 0 & 1 & 0 & 0 & 0 & 0 \end{bmatrix} \quad (61)$$

$$\mathbf{A} = \begin{bmatrix} a_{11} & \frac{b_{dt}}{J_r N_g} & -\frac{k_{dt}}{J_r} & 0 & 0 & 0 \\ \frac{\mu_{dt} b_{dt}}{J_g N_g} & -\frac{\mu_{dt} b_{dt}}{J_g N_g^2} - \frac{b_g}{J_g} & \frac{\mu_{dt} k_{dt}}{J_g N_g} & 0 & 0 & 0 \\ 0 & 0 & -\frac{1}{N_g} & 0 & 0 & 0 \\ 0 & 0 & 0 & -2\zeta\omega_n & -\omega_n^2 & 0 \\ 0 & 0 & 0 & 1 & 0 & 0 \\ 0 & 0 & 0 & 0 & 0 & -\alpha \end{bmatrix} \quad (62)$$

$$a_{11}(t) = \frac{1}{2J_r \lambda^2(t)} \rho \pi r^5 C_q(\lambda(t), \beta(t)) \omega_r(t) - \frac{b_{dt} + b_r}{J_r} \quad (63)$$

In simulation this scheme is accommodated by accordingly adding the vectors of the system noise and the measurement noise.

## 7 Simulations

The parameters used in the reference model are [21]

$$\begin{aligned} \rho &= 1.225 \text{ kg.m}^{-3} & r &= 57.5 \text{ m} & N_g &= 95 & \alpha &= 501 \text{ s}^{-1} \\ b_{dt} &= 775.49 \text{ N.m.s.rad}^{-1} & b_r &= 7.11 \text{ N.m.s.rad}^{-1} & b_g &= 45.6 \text{ N.m.s.rad}^{-1} & \xi &= 0.6 \\ k_{dt} &= 2.7 \times 10^6 \text{ N.m.rad}^{-1} & J_g &= 390 \text{ kg.m}^2 & J_r &= 55 \times 10^6 \text{ kg.m}^2 & \mu_{dt} &= 0.97 \\ \omega_n &= 11.11 \text{ rad.s}^{-1} \end{aligned}$$

and, consequently, the derived matrix elements are

$$\begin{aligned} a_{12} &= 1.4840 \times 10^{-2} & a_{13} &= -49.0909 & a_{21} &= 0.0203 \\ a_{23} &= 7.0688 \times 10^4 & a_{22} &= -0.1171 & a_{32} &= -0.0105 \\ a_{44} &= -13.3320 & a_{45} &= -123.4321 & a_{66} &= -50.0 \end{aligned}$$

Finally, supposing the constant speed wind profile, then the matrix element  $a_{11}$  is defined as:

$$\begin{aligned} \beta &= 0.05 & \lambda_s &= 2.4 & \omega_r &= 1.25 & C_q &= 0.25 \\ a_{11} &= 1.0499 \end{aligned}$$

To obtain parameters of the discrete-time system model (1), (2), the continuous-time representation was converted to the discrete-time form by the standard Matlab function using the sampling period  $t_s = 0.02 \text{ s}$  and the resulted equations were used for generating the input and output data to construct the instrumental variable in the simulation.

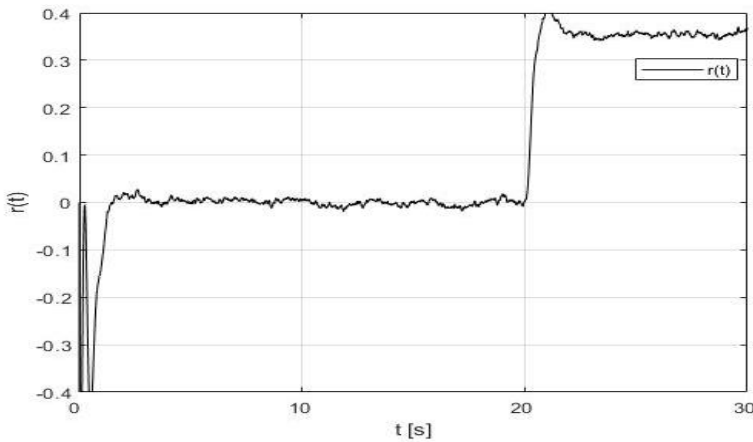


Figure 1

Time response of the residual filter on the first actuator fault

As the result Figure 1 presents the fault residual response reflecting a step-like fault in the gain loss of the first actuator at the time  $t_f = 20 \text{ s}$ . The FDI was trained according to the algorithm discussed in the paper and the result is analyzed

in the term of detection threshold. In order to generate a suitable training data set with the proportion balance of the faulty-free and the faulty event, there were set both interval parameters as  $r = s = 8$  and the value  $p = 12$ .

The system model was extended by the system noise input vector:

$$\mathbf{V}^T = [0.693 \ 0.397 \ 0.872 \ 0 \ 0 \ 0]$$

while the system noise  $v(i)$  obeys normal distribution with zero mean and standard deviation  $\sigma = 0.3$ .

These examples illustrate the power that can be invoked through the prescribed method properties.

### Conclusions

In the paper, a benchmark model is used for building and simulation testing a fault detection scheme, based on the subspace method data-driven principle, applicable to wind turbine benchmarks. To construct the reference residual from fault-free data, the discrete-time system model parameters are used for the prediction data set generation. Exploited data-driven methodology has sufficient adaptability in correspondence to different system operating points. Simulation case indicates that the residual performance is satisfactory.

Compared with the model-based fault detection method, prior knowledge of complex system model is not needed and only the parameterized matrices, need to be identified. Modifications of this framework to obtain hybrid solutions, combining neural networks and fuzzy inference system approaches, are the subject of future research in this algorithmic field, since the hybrid input-output representations are challenging research works in the wind turbine diagnosis. It is worthwhile to point out here, that the proposed method can be simply adjusted to disturbances or noise [23], which would be welcome applications in the wider industrial systems.

### Acknowledgement

The work presented in this paper was supported by VEGA, the Grant Agency of Ministry of Education and Academy of Science of Slovak Republic, under Grant No. 1/0483/21. This support is very gratefully acknowledged.

### References

- [1] R. K. Mehra and J. Peschon, "An innovations approach to fault detection and diagnosis in dynamic systems," *Automatica*, 1971, Vol. 7, pp. 637-640
- [2] A. S. Willsky, "A survey of design methods for failure detection in dynamic systems," *Automatica*, 1976, Vol. 12, pp. 601-611
- [3] D. M. Himmelblau, *Fault Detection and Diagnosis in Chemical and Petrochemical Processes*, 1978, Amsterdam, Elsevier

- 
- [4] V. Venkatasubramanian, R. Vaidyanathan, and Y. Yamamoto, "Process fault detection and diagnosis using neural networks - I. Steady-state processes," *Computers & Chemical Engineering*, 1990, Vol. 14(7), pp. 699-712
- [5] Z. Wang, Y. Wang, and Z. Ji, *Advances in Fault Detection and Diagnosis Using Filtering Analysis*, 2022, Singapore, Springer Nature
- [6] D. Du, S. Xu, and V. Cocquempot, *Observer-Based Fault Diagnosis and Fault-Tolerant Control for Switched Systems*, 2021, Singapore, Springer Nature
- [7] S. X. Ding, *Advanced Methods for Fault Diagnosis and Fault-tolerant Control*, 2021, Berlin, Springer Nature
- [8] Z. Chen, *Data-Driven Fault Detection for Industrial Processes. Canonical Correlation Analysis and Projection Based Methods*, 2017, Wiesbaden, Springer Nature
- [9] J. Zhao, W. Wang, and C. Sheng, *Data-Driven Prediction for Industrial Processes and Their Applications*, 2018, Cham, Springer Nature
- [10] J. Wang, J. Zhou, and X. Chen, *Data-Driven Fault Detection and Reasoning for Industrial Monitoring*, 2022, Singapore, Springer Nature
- [11] G. Niu, *Data-Driven Technology for Engineering Systems Health Management. Design Approach, Feature Construction, Fault Diagnosis, Prognosis, Fusion and Decision*, 2017, Singapore, Springer Nature
- [12] Q. Jia, W. Chen, Y. Zhang, and Y. Jiang, "Robust fault reconstruction in discrete-time Lipschitz nonlinear systems via Euler-approximate proportional integral observers," *Mathematical Problems in Engineering*, 2015, Vol. 2015, pp. 1-14
- [13] D. Krokavec and A. Filasová, "Descriptor approach in design of discrete-time fault estimators," *WSEAS Transactions on Systems and Control*, 2018, Vol. 13, pp. 481-490
- [14] W. Chen, S. X. Ding, A. Haghani, A. Naik, A. Q. Khan, and S. Yin, "Observer-based FDI schemes for wind turbine benchmark," *IFAC Proceedings Volumes*, 2011, Vol. 44(1), pp. 7073-7078
- [15] P. F. Odgaard and J. Stoustrup, "Fault tolerant control of wind turbines using unknown input observers," *IFAC Proceedings Volumes*, 2012, Vol. 45(20), pp. 313-318
- [16] P. F. Odgaard and J. Stoustrup, "Fault tolerant wind farm control - a benchmark model," *Proceedings of the IEEE International Conference on Control Applications CCA 2013, Hyderabad, India*, 2013, pp. 412-417

- [17] S. Simani, S. Farsoni, and P. Castaldi, "Wind turbine simulator fault diagnosis via fuzzy modelling and identification techniques," *Sustainable Energy, Grids and Networks*, 2015, Vol. 1(1), pp. 45-52
- [18] X. Liu, Z. Gao, and M. Z. Q. Chen, "Takagi-Sugeno fuzzy model based fault estimation and signal compensation with application to wind turbines," *IEEE Transactions on Industrial Electronics*, 2017, Vol. 64(7), pp. 5678-5689
- [19] D. Krokavec and A. Filasová, "One approach to design the fuzzy fault detection filters for Takagi-Sugeno models," *Advanced and Intelligent Computations in Diagnosis and Control*, 2016, Cham, Springer, pp. 19-33
- [20] D. Krokavec and A. Filasová, "Model-based fault diagnosis of wind turbines built on Takagi–Sugeno fuzzy observers," *Proceedings of the 10th International Scientific Symposium Elektroenergetika 2019*, Stara Lesna, Slovakia, 2019, pp. 377-382
- [21] P. F. Odgaard, J. Stoustrup, and M. Kinnaert, "Fault-tolerant control of wind turbines. A benchmark model," *IEEE Transactions on Control Systems Technology*, 2013, Vol. 21(4), pp. 1168-1182
- [22] J. F. Manwell, J. G. McGowan, and A. L. Rogers, *Wind Energy Explained. Theory, Design and Application*, 2009, New York, John Wiley & Sons
- [23] H. Sanchez, T. Escobet, V. Puig, and P. F. Odgaard, "Fault diagnosis of an advanced wind turbine benchmark using interval-based ARRs and observers," *IEEE Transactions on Industrial Electronics*, 2015, Vol. 62(6), pp. 3783-3793
- [24] S. Simani, S. Farsoni, and P. Castaldi, "Data–driven techniques for the fault diagnosis of a wind turbine benchmark," *International Journal of Applied Mathematics and Computer Science*, 2018, Vol. 28(2), pp. 247-268
- [25] D. Krokavec and A. Filasová, "Data driven approaches in fault detection of wind turbines," *Proceedings of the 11th International Scientific Symposium Elektroenergetika 2022*, Stara Lesna, Slovakia, pp. 126-130

# Energy Storage System Utilization, in a Distribution Power System

**Dušan Medved', Ľubomír Beňa, Rikin Jitendrakumar Tailor**

Technical University of Košice, Faculty of Electrical Engineering and Informatics,  
Department of Electric Power Engineering,  
Mäsiarska 74, 042 00, Košice, Slovak Republic  
Dusan.Medved@tuke.sk, Lubomir.Bena@tuke.sk,  
Rikin.Jitendrakumar.Tailor@tuke.sk

---

*Abstract: The contribution of energy storage systems (ESS) to the electricity system is the subject of this paper. There were implemented aspects that are extremely popular and typical in power system setup according to distribution network characteristics. For this reason, a power network included sources like wind farms and solar farms, and in some unfavorable situations, the distribution network link was used as a backup source of electricity. In this power system, load was seen as having constant power. Energy storage systems were put into place throughout the simulation to make up for lost power until a particular stage of discharge, at which point connections to the distribution system (DS) were made. Simulations were carried out in the Matlab/Simulink environment, to examine the collaboration of the aforementioned elements, over a 48-hour period, under various conditions.*

*Keywords: solar power plant; wind power plant; energy storage system*

---

## 1 Introduction

Households or companies who produce extra fuel or energy and occasionally supply it to the national (or local) distribution network, while also consuming the same fuel or energy from the network, are considered to be consumers of renewable energy sources (RES) (when their fuel or energy requirements exceed their own production). To do this, households install rooftop PV panels that produce electricity [1-3]. Additionally, these homeowners have the option to use battery storage to increase the amount of PV energy they consume on their own; this practice is called as prosumer in the literature. Businesses that produce biogas and feed it into the gas grid can also do this while using gas from the same grid at various times or in other locations.

The power network may already use such an element to regulate the power in the network if prosumers take part in benefit programs and so give free capacity for the network operator's aims. For this aim, the research discussed in this paper will be applied, in which the prosumer (Energy Storage System (ESS)) [17] [29] is used as a typical storage device and, in the case of a network power loss, the prosumer serves as an energy producer. The Simulink software, which was used to model a variety of potential circumstances in the electrical network, was used to examine the impact of such a prosumer's operation.

## 2 Simulation of a Case Study

The presented case study concerns the connection of the on-grid electrical network with the distribution system (DS) for the purposes of delivery, or power sales, and vice versa. This connection is made at the 22 kV node (designated M1 in Figure 1). The necessary power is obtained from the DS in the event that there is not enough energy to support the load. This model also includes other sources, including a wind farm (WPP) and a photovoltaic power plant (PVP) [4], [12-15].

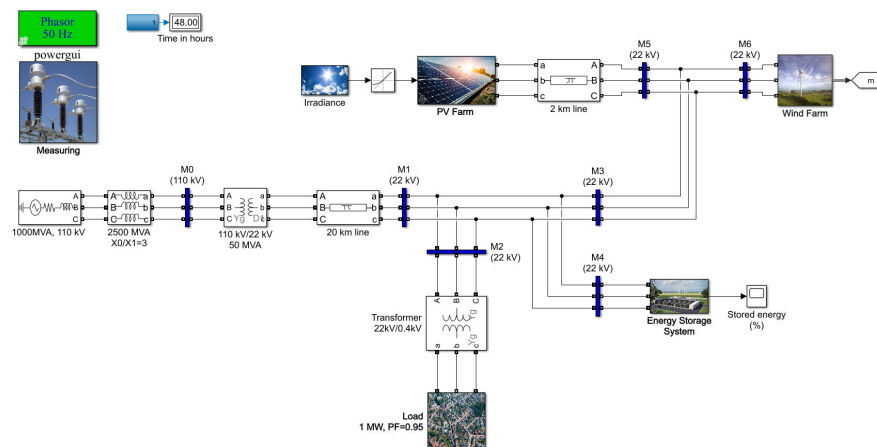


Figure 1

The environment of the Simulink program includes a schematic connection of the electrical circuit

In the distribution system, the M1 node creates the link between the distributor and prosumer. The prosumer is made up of a photovoltaic power plant (PVP), a wind power plant (WPP), and an energy storage system (ESS) at nodes M5 and M6. The measurement site for a load measurement system is also a load measuring at node M2.

The model offers measurements of critical parameters in real-time. In addition to current and active power flow, voltage monitoring in each node, frequency monitoring, and condition monitoring of the SoC (State of Charge) ESS are included.

The model also offers a comparison of the active power of production and non-production units. The identical components used to build the prosumer system depicted in Figure 1 were also used to build these systems.

## 1.1 The Predetermined Design Parameters

- A photovoltaic power plant (PVP) that is linked and has a total installed capacity of 1800 kWp, a useable area of 12000 m<sup>2</sup> and a 15% efficiency [17] [25]
- The 2-day sun diagram was used to determine the solar radiation properties (Figure 2).

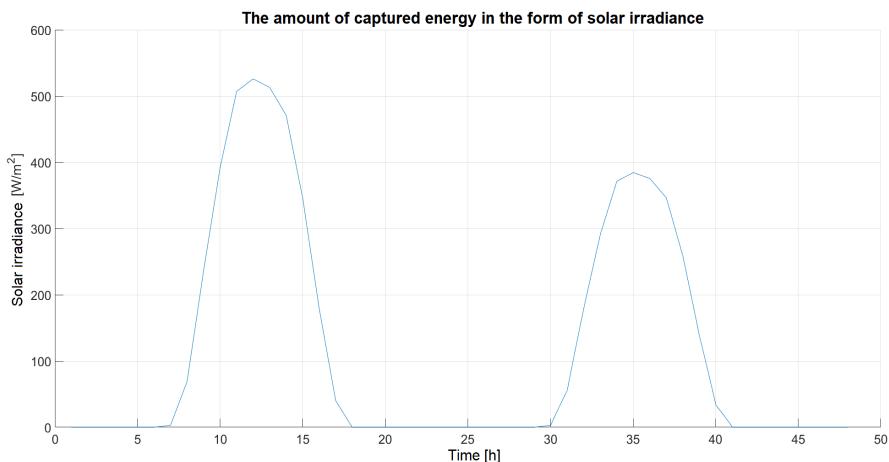


Figure 2  
Properties of solar radiation

- A load with a peak power of 1 MW (with the option to attach additional technical devices as a load with a total power of 3×50 kW in case of RES excess power)
- Load characteristics are determined using Figure 3
- The term “ESS” (Energy Storage System) can refer to a variety of potential energy storage technologies, including flywheels, compressed air, supercapacitors, etc.

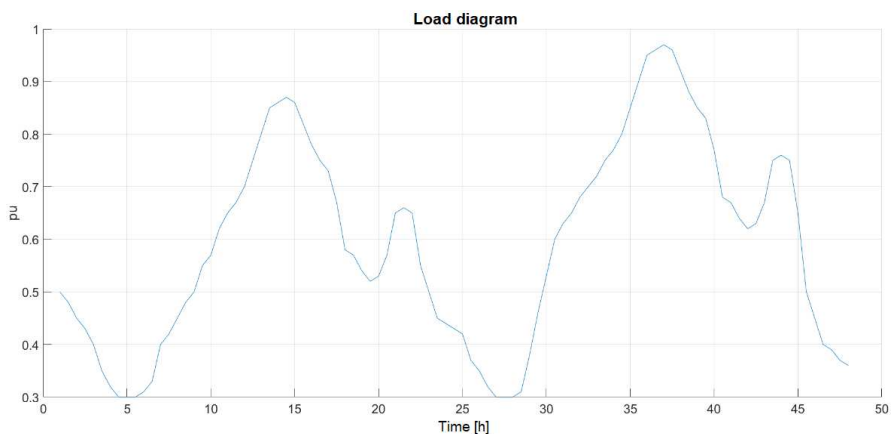


Figure 3

Graph illustrating the load throughout a 48-hour simulation (per units)

- Linked wind power plant with  $P_i = 400$  kW at nominal wind speed of  $v_{nom} = 9$  m/s
- The set ESS parameters are in accordance with Figure 4, with the exception of parameter no. 5, i.e., the maximum permitted power obtained from the DS has been adjusted from the original 400 kW to 250 kW

The Energy Storage System (ESS), similar to the Battery Energy Storage System (BESS), comprises four components: the control unit (ESS Control), the State of Charge (SoC) status computation, current sources that emulate ESS functionality (similar to a photovoltaic unit), and a 0.4 kV/22 kV transformer (Refer to Figure 4) [24].

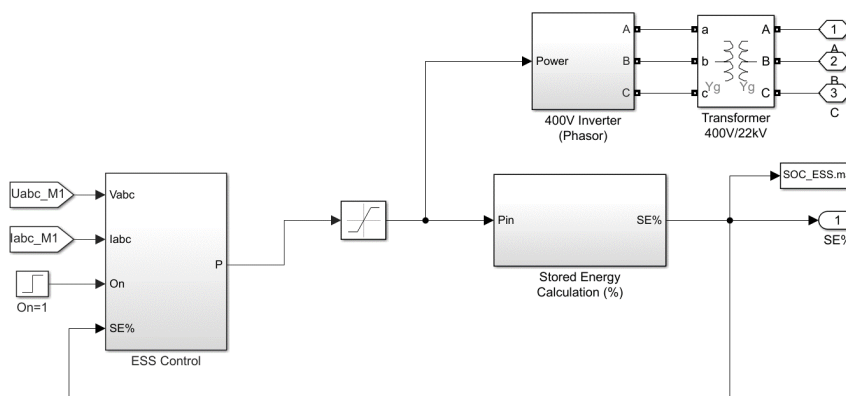


Figure 4

The ESS block subsystem is composed of four integral parts

The ESS, akin to the BESS, gets its charge from the distribution system (DS) during low tariff periods, which in this simulation model are set from 24:00 to 6:00. The system only permits charging when the ESS capacity is under the nominal ESS capacity.

The ESS control block incorporates several variables, including combined voltages and currents in node M1, active power computation, a constant for the maximum active power that can be sourced from the DS, and a constant for the maximum charging power [30].

The control block compares the immediate active power measurement with the maximum allowable active power consumption. Should the prosumer exceed the maximum allowable power consumption from the DS, the control block outputs the difference between the immediate active power value and the maximum permissible active power consumption, leading to the discharge of the ESS. This control function is only valid during the period between regular charging cycles, that is, from 6:00 to 24:00.

The “Charging Logic” block manages the charging behavior, outputting a logical “1” during the designated charging time and comparing it with the SoC state. If the SoC level falls under a set parameter, the ESS initiates charging at a specified interval [20-22].

To accurately simulate the ESS behavior, it is critical to monitor the SoC in real-time, which is accomplished using the Stored Energy Calculation block. The primary purpose of the ESS is to supplement the load when the maximum power consumption from the DS is exceeded.

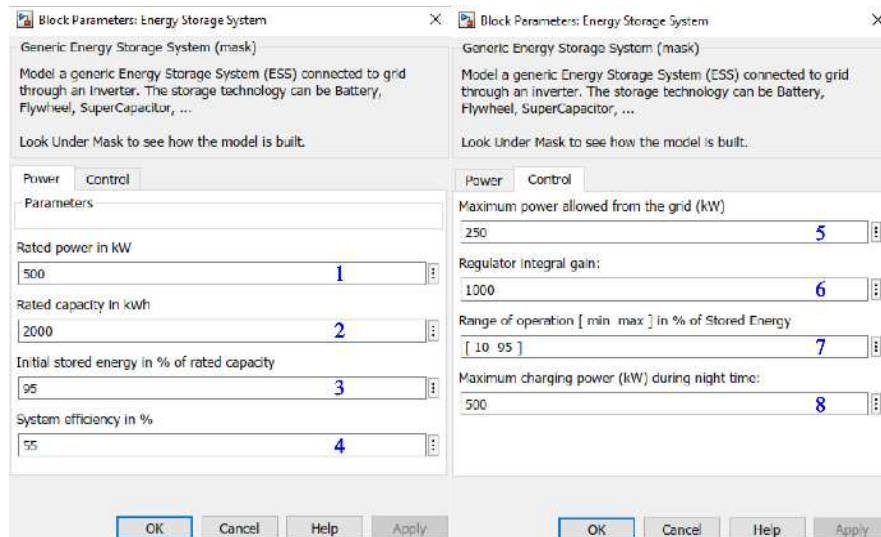


Figure 5  
ESS's default settings

Legend (parameters) for Figure 5:

- 1 Represents rated power in kW
- 2 Represents nominal ESS capacity in kWh
- 3 Represents initial ESS capacity in %
- 4 Represents system efficiency in %
- 5 Represents the maximum permitted power consumption in kW from the distribution network after which the ESS will start supplying power
- 6 Represents constant of the integration regulator
- 7 Represents range of usable battery capacity in %
- 8 Represents maximum charging power in kW

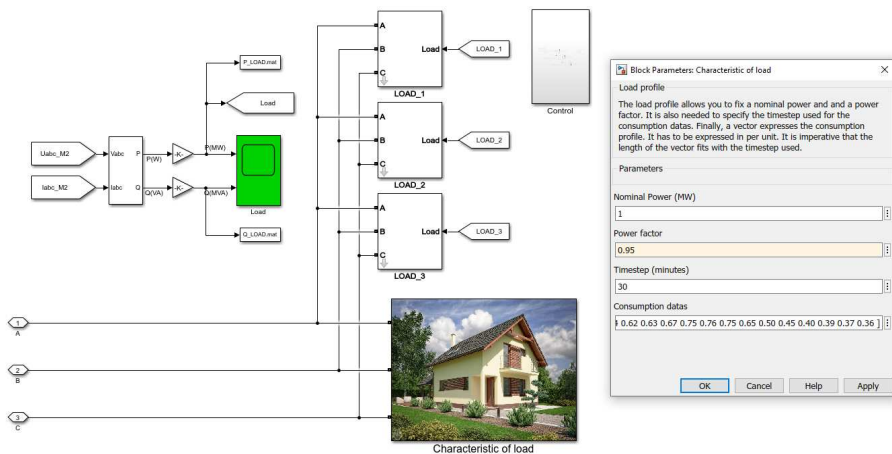


Figure 6

Diagram provides a comprehensive view of the distribution and management of dynamic and static loads within an energy system

The Load Block subsystem, depicted in Figure 6, is bifurcated into two sectors: a dynamic load and a static load.

The dynamic load incorporates the connection of several hundred households, along with the nearby industrial components. This is analogous to a dynamic network where the load varies over time. The static load, on the other hand, represents the technological equipment link, such as multiple electric boilers utilized for Domestic Hot Water (DHW) production. This connection operates in three stages ( $3 \times 50$  kW) when there's a surplus of active power on the side of the prosumer and the asynchronous motor [14].

The subsystem connection of the Load Block is shown in Figure 6. The dynamic load offers the capability to determine the nominal power in megawatts and to adjust the power factor, which influences the magnitude of the reactive power drawn by the load and the load characteristics. All electrical quantities are measured at the M2 node (22 kV), taking transformer losses into consideration.

For dynamic loads, analogous to Photovoltaic (PV) or Energy Storage System (ESS) units, there are current source connections operating on the same principle. However, the regulation of these sources is dependent on the load characteristic, and these sources contribute negative alternating current to the circuit.

### 3 An Outline of Transients

We took into account the beginning conditions of the model setup and separated the observed time (48 hours) into discrete intervals where we documented the evolution of power, voltage, frequency, and other significant features.

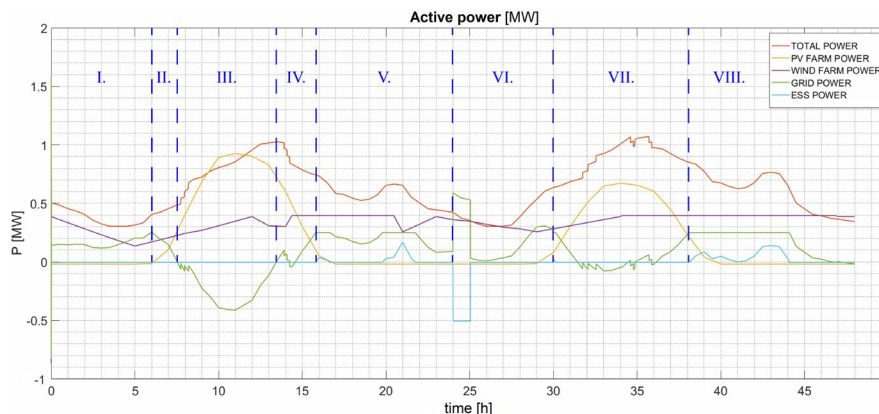


Figure 7  
Characteristics of active powers

Fig. 7's active power characteristics are described as follows:

- Power from the wind power plant (WPP) and from the DS is utilized to cover the load in the *I. interval* between 0 and 6 o'clock. ESS has finished charging.
- It begins providing PVP power to the network at the start of *II. interval*, which reduces the amount of power drawn from the DS.
- The extra electricity from RES is given to the DS during the *III. interval* with the intention of selling it. The technological equipment is connected

as a load in three states with a combined power of  $3 \times 50$  kW if the power supplied to the DS from RES exceeds the value of 50 kW, with the shutdown of technological equipment being coupled not only to the value of power supplied to the DS from RES but also for a specific period of time when they draw power from the network. This indicates that even if the RES does not supply power to the DS, these technological devices can still draw power from the network.

- Because the prerequisites for their continued operation are not satisfied, technical equipment is disconnected during the *IV. interval*.
- It will begin sending ESS power to the network at the start of the *V. interval* since the need of the maximum permitted power taken from the DS, namely 250 kW, has been satisfied.
- The period is set aside for charging the ESS during the *VI. interval*, which lasts between 24. and 30. hours. Even when fully charged to its built-in rated capacity in this time zone, the ESS cannot power the network.
- The wind farm supplies a rated output of 400 kW from around 34. o'clock in *VII. interval*, practically to the end of the simulation, which is characterized by a lower delivery of electricity from PVP than the III. period. Similar to III. interval, technical equipment is linked as a load in the event that there is extra electricity from RES.
- When it is becoming dark and the power from the PVP is fast decreasing in the last *VIII. period*, it is once again turned on by the ESS, which stabilizes the power obtained from the DS at 250 kW. Figure 13's depiction of the ESS SoC shows that the ESS capacity stabilized at 60% SoC. Table 1 shows that WPP, with a total of 16.17 MWh of power delivered to the network over the whole monitored period, was the main supplier, followed by PVP (9.85 MWh). 19.93% of the total power needed to handle the load was used by the prosumer from the DS.

Table 1  
Usage of electricity during case simulation

$W$ [MWh]	LOAD	TOTAL	ESS	GRID	PV FARM	WIND FARM
$W_{IN\_A}^*$	29.94	0.00	-0.71	-1.54	-0.51	0.0
$W_{OUT\_A}^{**}$	0.00	29.94	0.48	6.19	9.85	16.17

\*  $W_{IN\_A}$  is the electricity consumed by the load, accordingly in the form of losses

\*\*  $W_{OUT\_A}$  is electricity delivered by production units

The following graphs show the courses of the relevant quantities in nodes M0 to M6.

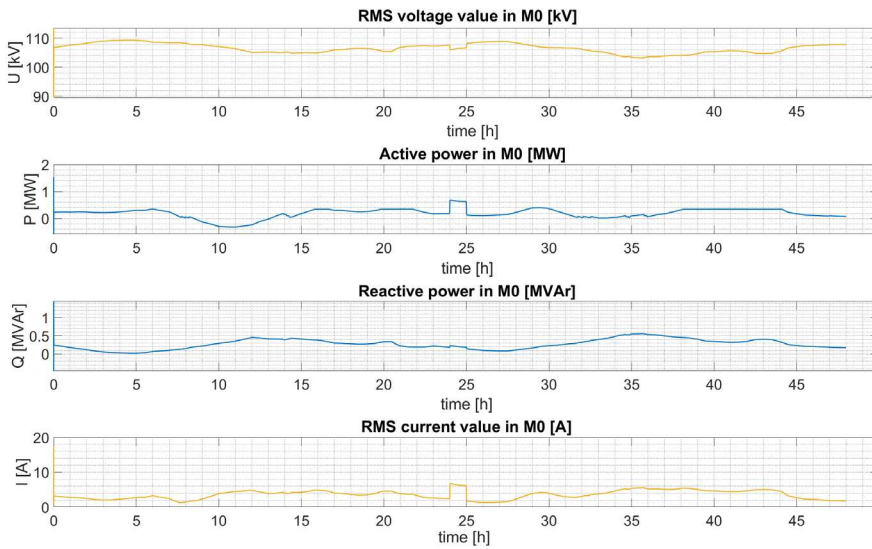


Figure 8  
Electrical parameters that were measured at the M0 node

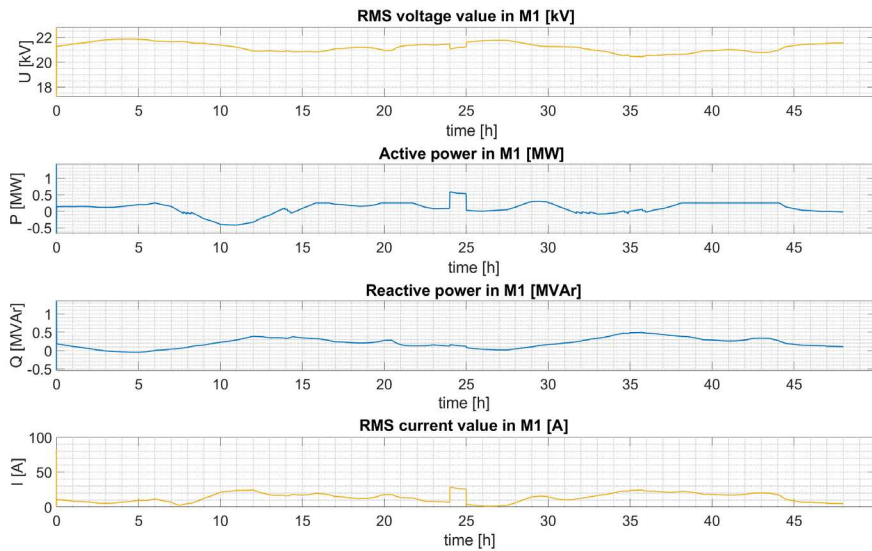


Figure 9  
Electrical parameters that were measured at the M1 node

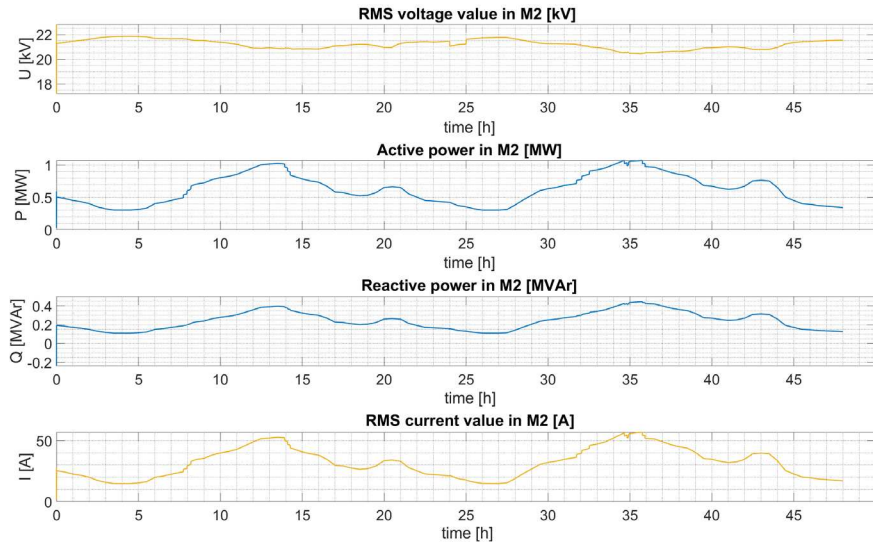


Figure 10  
Electrical parameters that were measured at the M2 node

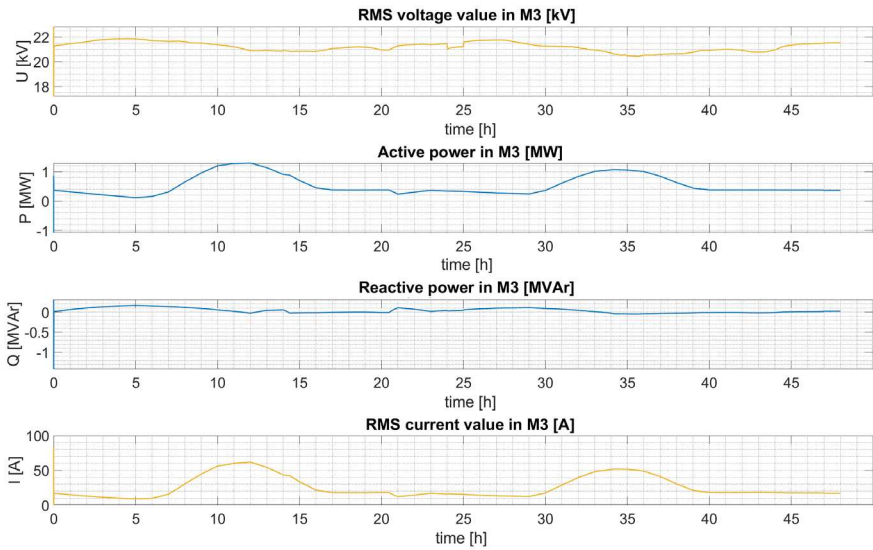


Figure 11  
Electrical parameters that were measured at the M3 node

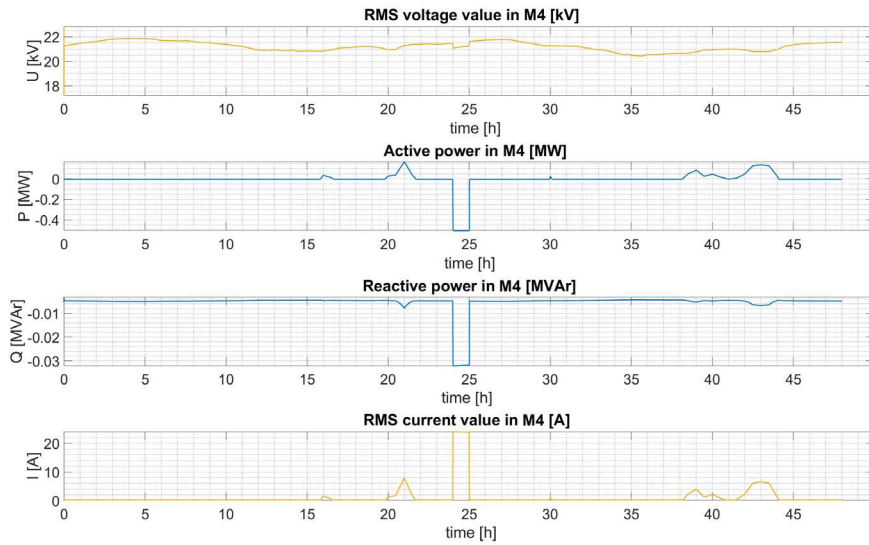


Figure 12  
Electrical parameters that were measured at the M4 node

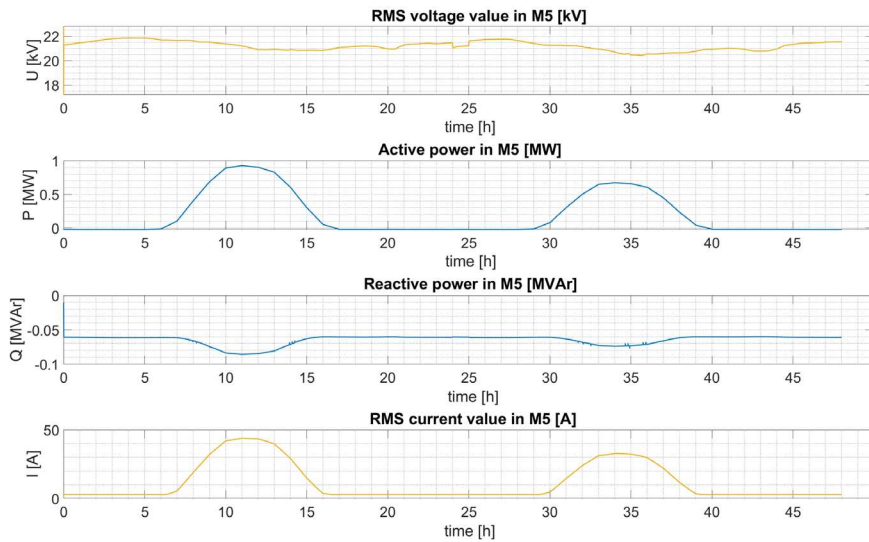


Figure 13  
Electrical parameters that were measured at the M5 node

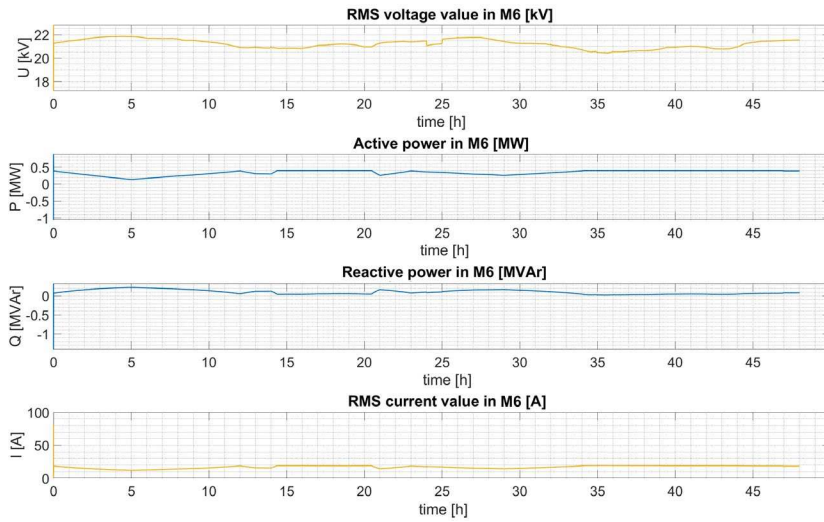


Figure 14  
Electrical parameters that were measured at the M6 node

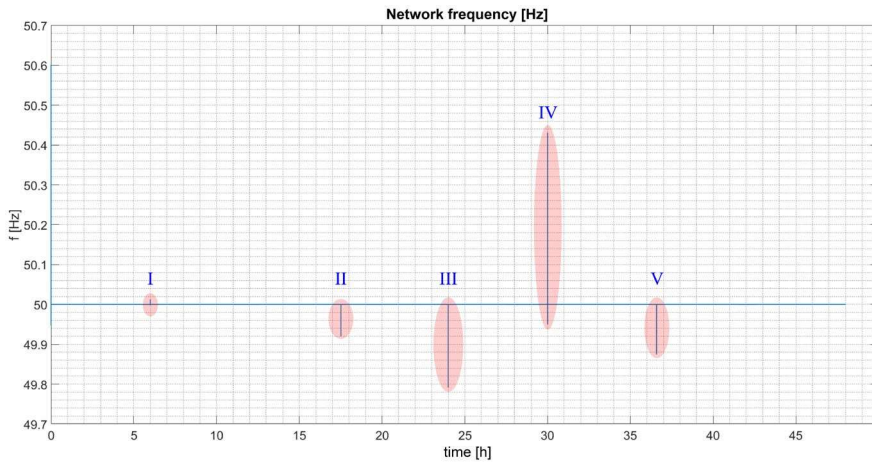


Figure 15  
The network's frequency fluctuation throughout the measured period

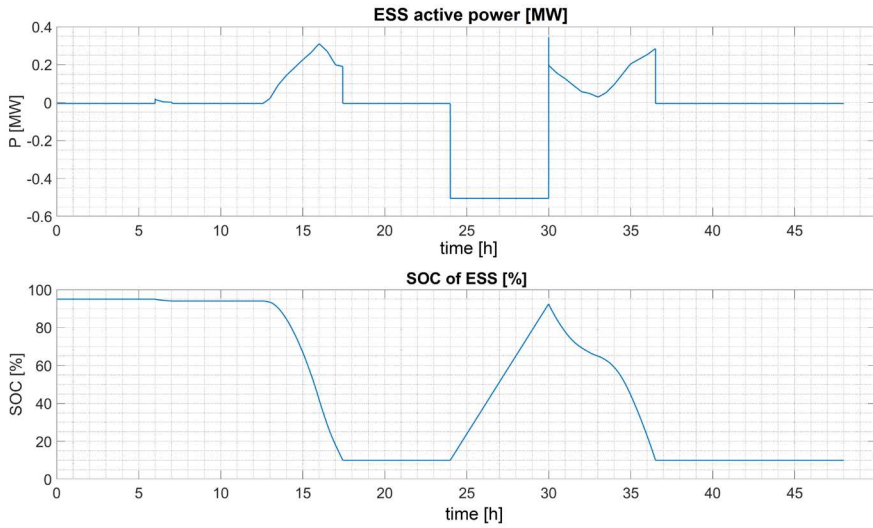


Figure 16  
The ESS's active power and state of charge state

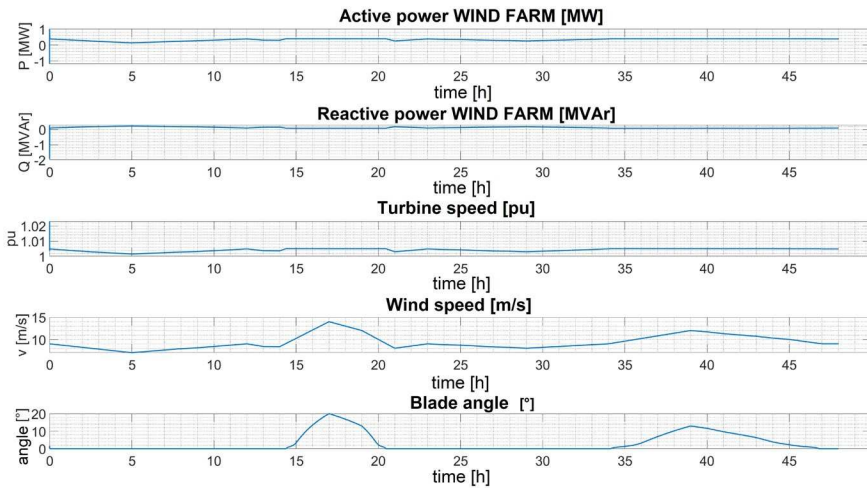


Figure 17  
Wind power plant characteristics that have been observed (blade rotation, wind speed, rotor speed)

The network's frequency characteristics are described in Figure 15:

- I. The progressive connection of the load, or technical equipment, in three stages of  $3 \times 50$  kW results in a fall in frequency below the nominal value  $f_n$
- II. The gradual disconnection of the load, or technological equipment, results in a rise in frequency above the nominal value  $f_n$
- III. The charging of the ESS causes the frequency to fall below the nominal value  $f_n$ , and the disconnection of the ESS causes the frequency to rise (end of charge, SoC = 95%)
- IV. The connection of the ESS as a result of the prosumer exceeding the maximum permitted power consumption from the DS, which is 250 kW, causes the frequency to grow over the nominal value  $f_n$
- V. The connection or disconnection of the load, where the regulation was decreased or raised by the power supply from DS, is again the cause of the frequency falling below or rising over the nominal value

### **Conclusions**

In the case scenario, a WPP with an installed power of 400 kW at a wind nominal speed of 9 m/s was added to the prosumer's electrical circuit design. The solar panels' useable area was 12000 m<sup>2</sup>, and their efficiency was 15%, increasing the PVP plant's installed capacity to  $P_i = 1800$  kWp. The parameter for the ESS, which originally set the maximum permitted power consumption from the DS at 400 kW, was adjusted to 250 kW.

In the case scenario, an extra active power demand in the form of technical equipment (such as an electric boiler) was connected in three stages of  $3 \times 50$  kW, which resulted in the consumption of 29.94 MWh of electricity within the allowed time period. Direct usage of RES electricity to meet the load accounted for 80.07% of the total (23.97 MWh). Also included in the extra RES electricity sent to the DS was a volume totaling 1.54 MWh.

When evaluating the quality of the electricity according to STN 50160 for LV and MV, we can determine that there were no dangerous phenomena in the entire interconnected electricity network when the load or production unit was connected or disconnected, respectively, and that the voltages and frequencies, the two key quality indicators, were kept within acceptable bounds. According to the frequency characteristics, the power control frequency errors for the on-grid system were in the order of tenths and did not exceed 0.5 Hz.

### **Acknowledgement**

This paper was supported by the Slovak Research and Development Agency, under the contracts APVV-19-0576, APVV-21-0312 and SK-UA-21-0024 and the Slovak Academy of Sciences, under the contracts VEGA 1/0757/21.

## References

- [1] J. Dang, J. Seuss, L. Suneja, R. G. Harley, “*SOC feedback control for wind and ESS hybrid power system frequency regulation*”, In Proceedings of the IEEE Power Electronics and Machines in Wind Applications, Denver, CO, USA, 16-18 July 2012; pp. 1-7, doi: 10.1109/PEMWA.2012.6316384
- [2] G. S. Lakshmi, O. Rubanenko, A. Hunko, “*Control of the Sectioned Electrical Network Modes with Renewable Energy Sources*”, In Proc. of the 2021 International Conference on Sustainable Energy and Future Electric Transportation (SEFET), Hyderabad, India, 21-23 January 2021; pp. 1-6, doi: 10.1109/SeFet48154.2021.9375781
- [3] G. Ren, “*MATLAB/Simulink-Based Simulation and Experimental Validation of a Novel Energy Storage System to a New Type of Linear Engine for Alt. Energy Vehicle Applications*”, IEEE Trans. Power Electron. 2018, 33, 8683-8694, doi: 10.1109/TPEL.2017.2784563
- [4] M. Makhlof, F. Messai, K. Nabti, H. Benalla, “*Modeling and simulation of grid-connected photovoltaic distributed generation system*”, In Proceedings of the 2012 First International Conference on Renewable Energies and Vehicular Technology, Nabeul, Tunisia, 26-28 March 2012; pp. 187-193, doi: 10.1109/REVET.2012.6195269
- [5] N. K. Roy, H. R. Pota, “*Current status and issues of concern for the integration of distributed generation into electricity networks*”, IEEE Syst. J. 2014, 9, 933-944, doi: 10.1109/JSYST.2014.2305282
- [6] B. Dolník, et.al., “*The Response of a Magnetic Fluid to Radio Frequency Electromagnetic Field*”. In: Acta Physica Polonica A. doi: 10.12693/APhysPolA.131.946
- [7] I. Kolcunová, et. al., “*Experimental observation of negative differential characteristic of corona discharge in ultraviolet spectrum*”. In: Journal of Electrostatics. doi: 10.1016/j.elstat.2016.12.016
- [8] J. Zbojovský, L. Kruželák, M. Pavlík, “*Impedance Spectroscopy of Liquid Insulating Materials*”. In: IEEE CANDO-EPE 2018, IEEE International Conference and Workshop in Óbuda on Electrical and Power Engineering, Nov. 20-21, 2018, Budapest, Hungary. ISBN: 978-1-7281-1154-4
- [9] M. Pavlík, I. Kolcunová, L. Lisoň, “*Measuring the shielding effectiveness and reflection of electromagnetic field of building material*”. In: 2015 16<sup>th</sup> International Scientific Conference on Electric Power Engineering (EPE), 2015, pp. 56-59, doi: 10.1109/EPE.2015.7161186
- [10] I. Kolcunová, J. Zbojovský, M. Pavlík, S. Bucko, J. Labun, M. Hegedus, M. Vavra, R. Cimbala, J. Kurimský, B. Dolník, J. Petráš, J. Džmura, “*Shielding Effectiveness of Electromagnetic Field by Specially Developed Shielding Coating*”. In: Acta Physica Polonica A. Warsaw (Poland):

- Instytut Fizyki. Vol. 137, No. 5 (2020), pp. 711-713. ISSN 0587-4246. doi: 10.12693/APhysPolA.137.711
- [11] J. Jirinec, D. Rot, R. Velev, “*The Energy Efficient Solution for Intelligent Lighting*”, In: 2019 20<sup>th</sup> International Scientific Conference on Electric Power Engineering (EPE), 2019, pp. 1-4, doi: 10.1109/EPE.2019.8777938
- [12] K. Noháč, L. Raková, V. Mužik, K. Máslo, “*Open Source Platforms for Dynamic Stability Assessment*”, In: 2019 20<sup>th</sup> International Scientific Conference on Electric Power Engineering (EPE), 2019, pp. 1-6, doi: 10.1109/EPE.2019.8778087
- [13] D. Kapral, P. Bracinik, M. Roch, M. Hoger, “*Optimization of distribution network operation based on data from smart metering systems*”, In: Electrical Engineering, Vol. 99, Issue 4, Springer, New York, USA, 2017, December, pp: 1417-1428, ISSN 0948-7921. doi: 10.1007/s00202-017-0628-x
- [14] Z. Eleschova, B. Cintula, V. Volcko, A. Belan, J. Bendik, M. Cenky, “*The Influence of Smart Grids on a Large Synchronous Generators Operation*”, In: Proceedings of the 2018 19<sup>th</sup> International Scientific Conference on Electric Power Engineering (EPE), pp 43-48, doi: 10.1109/EPE.2018.8395948
- [15] K. Nohac, M. Tesarova, L. Nohacova, J. Veleba, V. Majer, “*Utilization of Events Measured by WAMS-BIOZE-Detector for System Voltage Stability Evaluation*”, In: IFAC Workshop on Control of Transmission and Distribution Smart Grids (CTDSG), Volume: 49, Issue: 27, pp 364-369, ISSN 2405-8963, doi: 10.1115/1.4043103
- [16] D. Rot, J. Kozeny, S. Jirinec, J. Jirinec, A. Podhrazky, I. Poznyak, “*Induction melting of aluminium oxide in the cold crucible*”, In: 18<sup>th</sup> International Scientific Conference on Electric Power Engineering (EPE) 2017, pp 1-4, doi: 10.1109/EPE.2017.7967281
- [17] D. Pál, L. Beňa, J. Urbanský, M. Oliinyk, “*The impact of reconfiguration on power losses in smart networks*”, In: 2020 21<sup>st</sup> International Scientific Conference on Electric Power Engineering (EPE), 2020, pp. 1-5, doi: 10.1109/EPE51172.2020.9269189
- [18] M. Sulír, J. Porubän, “*Augmenting Source Code Lines with Sample Variable Values*”, In: 2018 IEEE/ACM 26<sup>th</sup> International Conference on Program Comprehension (ICPC), 2018, pp. 344-347, doi: 10.1145/3196321.3196364
- [19] M. Tesařová, R. Vykuka, “*Impact of Distributed Generation on Power Flows Along Parallely Operated MV Feeders*”, In: Int. Conf. on Env. and El. Eng. and 2018 IEEE Ind. and Com. Power Syst. Europe, IEEEIC/I and CPS Europe 2018, doi: 10.1109/IEEEIC.2018.8493640

- [20] P. Girovský, J. Žilková, J. Kaňuch, “*Optimization of Vehicle Braking Distance Using a Fuzzy Controller*”. In: *Energies*. 2020; 13(11):3022. doi: 10.3390/en13113022
- [21] M. Bereš, D. Kováč, T. Vince, I. Kováčová, J. Molnár, I. Tomčíková, J. Dziak, P. Jacko, B. Fecko, Š. Gans, “*Efficiency Enhancement of Non-Isolated DC-DC Interleaved Buck Converter for Renewable Energy Sources*”. In: *Energies*. 2021; 14(14):4127. doi: 10.3390/en14144127
- [22] B. Cintula, Ž. Eleschová, M. Cenký, P. Janiga, J. Bendík, A. Beláň, “*Three-Phase and Single-Phase Measurement of Overhead Power Line Impedance Evaluation*”. In: *Energies*. 2021; 14(19):6314. doi: 10.3390/en14196314
- [23] J. Kanuch, P. Girovsky, “*The device to measuring of the load angle for salient-pole synchronous machine in education laboratory*”, In: *Measurement*, Volume 116, 2018, pp 49-55, ISSN 0263-2241, doi: 10.1016/j.measurement.2017.10.043
- [24] M. Cenký, J. Bendík, Ž. Eleschová, A. Beláň, B. Cintula, P. Janiga, “*Probabilistic Model of Electric Vehicle Charging Demand to Distribution Network Impact Analyses*”, In: 2019 20<sup>th</sup> International Scientific Conference on Electric Power Engineering (EPE), 2019, pp. 1-6, doi: 10.1109/EPE.2019.8777973
- [25] B. C. Sánchez, M. Váry, M. Perný, F. Janíček, V. Šály, J. Packa, “*Prediction and production of small PV power plant*”, In: 2017 18<sup>th</sup> International Scientific Conference on Electric Power Engineering (EPE), 2017, pp. 1-5, doi: 10.1109/EPE.2017.7967276
- [26] M. Pavlik, “*Compare of shielding effectiveness for building materials*,” *Przeglad Elektrotechniczny*, 95(5), 137-140, doi: 10.15199/48.2019.05.33
- [27] S. Bucko, M. Krchnak, R. Cimbala, L. Kruzela, J. Zbojovsky, “*Abrasive properties of transformer oil-based magnetic nanofluid*,” In: 19<sup>th</sup> International Scientific Conference on Electric Power Engineering (EPE), 2018, pp. 1-4, doi: 10.1109/EPE.2018.8396038
- [28] A. Beláň, B. Cintula, M. Cenký, P. Janiga, J. Bendík, Ž. Eleschová, A. Šimurka, “*Measurement of Static Frequency Characteristics of Home Appliances in Smart Grid Systems*”. *Energies* 2021, 14, 1739. doi: 10.3390/en14061739
- [29] M. Kajanova, P. Bracinik, “*Social welfare-based charging of electric vehicles in the microgrids fed by renewables*” In: *International Journal of Electrical Power & Energy Systems*, Vol. 138, doi: 10.1016/j.ijepes.2022.107974
- [30] P. Jacko, M. Beres, I. Kovacova, J. Molnar, T. Vince, J. Dziak, B. Fecko, S. Gans, D. Kovac, “*Remote IoT Education Laboratory for Microcontrollers Based on the STM32 Chips*”, In: *Sensors*. 2022; 22(4):1440. doi: 10.3390/s2204144

- [31] M. Beres, D. Kovac, T. Vince, I. Kovacova, J. Molnar, I. Tomcikova, J. Dziak, P. Jacko, B. Fecko, S. Gans, “*Efficiency Enhancement of Non-Isolated DC-DC Interleaved Buck Converter for Renewable Energy Sources*”, *Energies*. 2021; 14(14):4127. doi: 10.3390/en14144127

# Demand-Supply Balancing in Energy Systems with High Photovoltaic Penetration, using Flexibility of Nuclear Power Plants

**Illia Diahovchenko<sup>1,2\*</sup>, Ihor Yevtushenko<sup>1</sup>, Michal Kolcun<sup>3</sup>, Zsolt Čonka<sup>3</sup>, Tetiana Zahorodnia<sup>1</sup>, Petro Vasyleha<sup>1</sup>**

<sup>1</sup>Sumy State University, Ryms'koho-Korsakova, 2, 40007 Sumy, Ukraine, i.diahovchenko@etech.sumdu.edu.ua, etech@etech.sumdu.edu.ua, t.zahorodnya@etech.sumdu.edu.ua, p.vasylega@etech.sumdu.edu.ua

<sup>2</sup>Institute for Research in Technology, ICAI, Comillas Pontifical University, Alberto Aguilera, 25, 28015 Madrid, Spain

<sup>3</sup>Technical university of Košice, Letná, 1/9, 04001 Košice, Slovakia, michal.kolcun@tuke.sk, zsolt.conka@tuke.sk

\*Corresponding author

---

*Abstract: Energy transition requires scaling up the supply of low emissions electricity from renewable energy sources (RESs) and acceleration of deployment of dispatchable sources of low emissions electricity such as hydro and nuclear. Power output from RESs, particularly photovoltaic (PV) generation, can vary periodically and irregularly, depending on weather conditions. At high PV penetration levels, this peculiarity of the technology can not only cause voltage and power flow fluctuations in the local distribution grids, but also violate the demand-supply balance of a whole energy system, resulting in issues with frequency control and difficulty of demand supply management. This study is primarily focused on demand and supply balancing of an energy system with high PV penetration levels, assuming a significant share of nuclear power plants (NPPs), as well as thermal power plants (TPPs) and a strong transmission system. The potential benefits of flexible nuclear operations in an energy system are analyzed. It is demonstrated that nuclear power plants' flexibility can reduce the share of environmentally unfriendly thermal power units and substantially reduce the restrictions for renewable energy. The IEEE 9-bus test system is used for the case study.*

*Keywords: nuclear energy; flexible operation; renewable energy integration; demand-supply balancing; transmission power system; nuclear terrorism*

---

# 1 Introduction

## 1.1 Global Energy Goals and Challenges

The expansion of solar, wind, and modern bioenergy is particularly significant, while nuclear and hydropower also contribute. Today about 25% of total energy supply is from low emissions energy sources and this expands to around 50% by 2030 in the net zero emissions by 2050 scenario [1]. In the announced pledges scenario, electricity demand increases by 30%, from around 23300 TWh today to about 30300 TWh by 2030, while global CO<sub>2</sub> emissions from electricity generation fall by around 18% in 2030 [1]. Future growth in energy is predicted to mostly come from non-industrialized countries, while for the European Union energy demand is expected to drop slightly. For Asia high growth rates of more than 60% are projected, and the largest absolute boost in energy demand will be observed in China and India [2].

Rapid decarbonization of the electricity sector requires a massive surge in the deployment of low emissions generation. The share of renewables increases from almost 30% of electricity generation globally in 2020 to about 45% in 2030 in the announced pledges scenario [1], but this is still 15% points short of the level reached in the net zero emissions.

Nuclear power and dispatchable low emissions capacity, such as hydropower, biomass and geothermal are important elements of the picture, but capacity additions are dominated by PV and wind. The largest increases in deployment to close the emissions gap take place in emerging market and developing economies [1].

Global energy supply relies predominantly on fossil fuels like oil, coal and natural gas. The most important energy fuel is oil, mostly to fuel cars. Then comes coal, which is primarily used to generate electricity. Third place goes to natural gas, which heats homes, and also generates electricity in turbines. While new sources of energy are gradually changing the energy landscape, the burning of oil, gas, and coal is harmful to the environment. Most prominently, this leads to CO<sub>2</sub> emissions causing global warming. Without further measures, average global temperature will climb by more than 3°C by the end of the century, and sea levels may rise by up to 1 m [2]. To prevent the Earth from overheating, CO<sub>2</sub> and other greenhouse gas emissions must be reduced by at least 50% by the midst of this century, compared to their 1990 levels.

In the announced pledges scenario [1], coal demand declines by 10% to 2030, and almost 85% of demand growth is met by renewables, as a result of which the share of nuclear and renewables increases from 17% to 24% in 2030 and the share of unabated fossil fuels declines to 72% of the global energy mix.

To achieve national policy targets and in response to technological progress, the power sector is expected to go through a phase of significant transformation in most countries. Germany, for example, has decided to switch to a renewable energy economy and leave oil, coal, gas and also nuclear behind. The share of renewables in the power mix in Germany is expected to increase from currently 30% to 50% in 2030 and to 80% in the year 2050 [2]. In comparison, France has decided to reduce the share of nuclear power from the current 75% to 50% over the next 10 years and to increase the share of renewable energies in turn [2].

## 1.2 Implementation of Energy Efficiency

Energy efficiency implies that more energy services can be generated with the same fuel input, or alternatively, that less fuel input is needed to achieve the same energy service [3]. It reduces reliance on external suppliers of oil and gas and also provides business opportunities for European companies such as construction firms, manufacturers of energy-using equipment or companies selling energy services. For these reasons, the efficient use of energy is also perceived as Europe's biggest energy resource.

Besides saving energy costs, energy efficiency can bring multiple other benefits to households, companies and nations. A recent study by the International Energy Agency finds that improved energy efficiency could reduce the world's energy needs in 2050 by one third at no extra costs, and thus contribute substantially to fight global warming [3]. Projections by the International Energy Agency though suggest that as much as two-thirds of the economically viable energy efficiency potential will remain untapped unless policies change [3].

Consumers, industry and governments all have a role to play in this market. Consumers buy energy efficient technologies and services. Industry invests in research and development to bring to the market energy efficient equipment. Governments invest in policy programs. Indeed, the energy efficiency markets are largely dependent on policies to create the conditions for the market to function. The potential of profitable efficiency measures is huge, but without strong, additional policies, most of it is expected to remain untapped nonetheless, especially in the building sector [4].

## 1.3 Balancing Operation and Generation Dispatch

To maintain the power balance in a system, it is necessary to schedule the generation of each dispatchable generation unit. The total power demand, which reflects all the changes of all individual demands, varies hourly, daily, weekly, depending on a season and a year. In a power system the balance of demand and supply is ensured by controlling the output of the dispatchable generators in a demand-and-supply balancing area. When the instantaneous balance is insufficient or lost, the power

system's frequency (nominally 50 Hz or 60 Hz) or voltage will fluctuate, reducing the quality of supply [5]. In the worst-case multiple devices, including power plants with rotating machines, which are designed to operate within a specified range of frequency deviation, are disconnected from the power system, leading to a blackout (see Fig. 1).

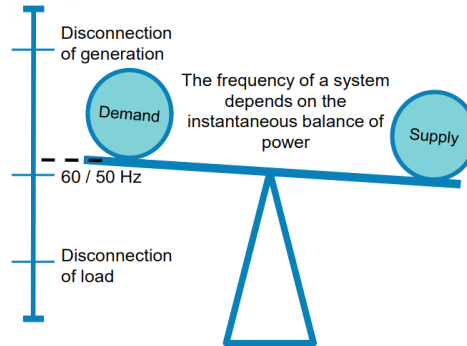


Figure 1

Frequency control in a power system [5]

The balancing between demand and supply is realized through sophisticated generation schedule to make the best use of the features of each generation unit and system: the hourly balancing through generation unit's starts and stops, the balancing in minutes through centralized automatic generation control specifying the production of each unit, the balancing in seconds through independent governor control of each unit, and the remaining mismatch is transformed into a fluctuation of the system frequency [6]. Because the balancing requirements vary by time, by day, by season, reflecting the variation of the demand and supply structure including the share of RESs (e.g., photovoltaic), the key concept to accommodate large amount of variable generation is the flexibility of a power system to cope with the balancing.

#### 1.4 Integration of Variable Renewable Energy

Ukraine has also joined the global course towards decarbonization, development and dissemination of energy-saving technologies and renewables. Recently in Ukraine there is a steady trend for reducing electricity production at pulverized coal power units and increasing the share of carbon-neutral electricity from RESs [7]. One of Ukraine's commitments under the Association Agreement with the European Union is the development and maintenance of RESs, taking into account the principles of economic feasibility and environmental protection. Renewable energy is recognized as one of the main priorities of energy reform, and the promotion of energy production from alternative energy sources is the task of state policy in the energy sector. This is enshrined in the adopted Energy Strategy of Ukraine, for the

period up to 2035 and in the provisions of the legal framework. Renewable energy guarantees environmental security and energy independence to the entities that implement it [8].

The United Energy System (UES) of Ukraine is a set of power plants, electrical and thermal networks operating in the general mode of generation, transmission and distribution of electrical and thermal energy. NPPs, TPPs and hydroelectric power plants (HPPs), combined heat and power (CHP) plants, as well as power plants running on alternative energy resources (i.e., solar, wind, biofuel and others) operate in parallel in the UES of Ukraine. All of them are connected by main electric networks. As of mid-2021, the share of electricity generated by nuclear generation is 58.7%, HPPs and pumped storage hydropower – 10.2%, RESs – 9.1%, TPPs and CHPs – 20.5% [7].

Solar energy has received the greatest development among RESs in Ukraine [9]. One of the main advantages of photovoltaics is that due to its modular aspect the size of a system may range from few Watts to several MW or even GW. Another big advantage is that this power production may often be organized directly where it is needed, eliminating most of the transportation and distribution cost. A drawback often put forward is the variability of the power production of solar power plants (SPPs). The PV modules, which constitute the SPPs, can generate electricity during a fairly narrow period of time during the day and demonstrate fluctuations in power production periods due to weather conditions. The SPPs significantly affect the schedule of operation of TPPs, which are the second main source of electricity in Ukraine, along with NPPs. This results in additional costs spent for operation of TPPs. As the installed capacity of SPPs increases, these costs will rise further, and will reduce the efficiency of TPPs in the long run.

NPPs, which account for the largest share of generation, operate on a uniform schedule and create an energy base during the day. NPPs increase or decrease power very slowly, so abrupt maneuvers are simply dangerous. As a result, nuclear power plants cannot increase production during the evening peaks and decrease it at night, when there is a "night dip" in electricity consumption. At the same time, energy share from RESs is growing rapidly, which is a cause for concern. Unlike NPPs, which emit energy constantly and in the same amount, RESs are variable and dependent on weather conditions (i.e., availability of sun or wind) [10] [11]. These are two extremes, and both need to be balanced by those energy sources that can be more easily turned on and off as needed.

The daily and seasonal variability of wind and solar generation present a challenge to their efficient integration into existing electrical grids. In general, the variability and uncertainty introduced by renewable energy calls for a higher level of system flexibility. The amount of flexibility needed to accommodate the introduction of new RESs depends on their capacity and the existing flexibility in the system's infrastructure and operation [10]. This article considers one of the possible ways to overcome this problem – the theoretical possibility of increasing the flexibility of

NPPs. Requirements for the operational stability of energy systems are discussed and highlighted.

The main tasks of the study are as follows:

- Assess the possibility of integrating high levels of variable solar energy without compromising reliability with operational and institutional changes.
- Analyze the impact of unregulated use of SPPs on the modes of electricity generation.
- Estimate the possibility of regulating the operation of the UES with different shares of SPPs in the energy balance.
- Assess the feasibility of flexible regulation of NPPs in terms of power losses and PV curtailment reduction.

Of practical importance is the possible introduction of a mechanism to maintain the balance of demand and supply in the energy system with a significant share of RESs, using the maneuverability of NPPs and TPPs.

The rest of this paper is organized as follows. Section 2 introduces the conditions to maintain the balance of demand and supply of electricity, Section 3 presents the approach to model the power system with NPPs and SPPs, Section 4, defines the case study, and Section 5 provides a discussion of the obtained results and estimates the role of flexible nuclear operations in the energy system. Finally, Section 6 presents the conclusions drawn.

## **2 Maintaining the Necessary Balance of Demand and Supply of Electricity**

### **2.1 Covering Consumers' Demand of Electric Energy in the UES of Ukraine**

The balance of production and consumption of electric energy in the UES of Ukraine is mainly maintained jointly by power units of TPPs and HPPs [12]. At the same time, the maneuverability of HPP power units is usually used during the morning and evening maximums of the power demand. Therefore, the uneven consumers' demand in the UES of Ukraine is predominantly covered with the maneuverability of power units of TPPs. It is impossible to completely exclude at least a part of thermal power units from the daily schedule of load covering in order to reduce their daily starts-stops, because without their participation it is difficult to cover uneven demand through the day, including the maximal demand periods. In addition, TPP power units often remain the only means for regulation of the modes of electricity generation at night [13].

Obviously, the forced use of TPP power units as maneuverable generating capacities of the UES is associated with significant additional costs for their daily start-ups, as well as with costs for the energy generation by these power units [14]. Moreover, this mode of operation is not provided by the design of thermal power units, which leads to the increased wear of equipment, reduced reliability of its operation, as well as increased costs for scheduled and post-emergency repairs of thermal power units [12].

It should also be noted that thermal power units, which are used to regulate the operating capacity of the UES, mostly operate in energy-inefficient modes, especially at night, and their fuel consumption increases. The cost of fuel used in the operation of TPP units with variable load also increases, as the so-called fuel "backlight" (i.e., adding a certain amount of natural gas or fuel oil to the main fuel (coal) to facilitate ignition and ensure sustainable combustion) is periodically required.

The named shortcomings of the forced use of thermal power units as maneuverable generation have a negative impact on the efficiency of the UES of Ukraine, and it is one of the reasons for the increase in wholesale prices and retail electricity tariffs. Thus, despite the significant potential of unloaded generating capacity in the UES of Ukraine, reliable and high-quality energy supply is becoming a challenging task for the energy sector.

## **2.2 Negative Impacts of Uncontrolled Use of SPPs on the Modes of Operation of TPPs**

The need to cover uneven loads is inevitably associated with reduced reliability and efficiency of the power system, the main reason is that in the UES of Ukraine there is a significant shortage of shunting generating capacities, i.e., power units that can quickly go into operation from hot or cold reserve and change the magnitude of their power output in a wide range.

The greatest difficulties in managing the modes of electricity generation in the UES occur during the night demand minimum [15]. These complications are especially noticeable on summer weekends, when consumers' demand slightly exceeds the base (almost unregulated) capacity of operating NPP units. In this situation, even relatively small fluctuations in consumers' demand are extremely difficult for the power system. In the event of reduced power demand, it may be necessary to quickly shut down one of the NPP units, which is not only undesirable for economic reasons, but also impossible for technical reasons, as well as in terms of NPP's safety [16]. In case of a short-term increase in power demand, it may be necessary to curtail some loads or limit their electricity consumption, as the TPPs in reserve cannot be brought into operation quickly enough, and this usually takes at least 1-2 hours. Limiting electricity demand leads to reduction of generation at power plants, which means a reduction of their capacity factor.

The opposite problem is the growing share of RESs in the country's energy balance. If there is an excess of unregulated generation from SPPs in the UAS, while the power demand remains unchanged, the need for electricity production by the thermal power units will decrease. Thus, there will be a need to reduce the output of TPP units or even reserve part of them. It is clear that this will increase the uneven loading of TPP units, significantly worsen their operation modes, leading to rise in costs for their operation and maintenance [12].

Given that, the uncontrolled use of SPPs can gradually exacerbate one of the biggest problems of the UES of Ukraine, which is the uneven daily load schedules of traditional generation, including TPPs. Combined with the shortage of maneuverable generating capacities, this will inevitably decrease the reliability and efficiency.

### **2.3 Applications of NPP's Flexibility for Maintaining the Balance of Demand and Supply**

Increasing the flexibility of generation sources is one of the mechanisms to address the generation variability and ensure the balance of demand and supply. Power systems with increasing penetrations of variable renewable energy sources (i.e., wind and solar power) require greater system flexibility, including operating reserves and ramping capability to ensure that the supply-demand balance is maintained at all times [17-19].

This paper considers the viability of the flexibility enhancing of existing NPPs to allow faster response to demand changes. It should be noted that flexible operation of conventional generators often results in increased fuel, maintenance and capital costs that must be balanced against the benefits of increased levels of renewable energy in the system [6].

NPPs are commonly operated in a "baseload" mode, producing their maximum rated capacity whenever online, while the electricity demand varies during the day and year. In the power system generation must constantly correspond to consumption, and if there are too many NPPs in the system, they will have to change their capacity in response to changes in demand [20]. NPPs are technically capable of more flexible operation, changing their power output over time (i.e., ramping or load following) and contributing to power system reliability needs, including frequency regulation and operating reserves [21]. Flexible operation can help manage daily and seasonal variability in demand or renewable energy output or respond dynamically to hourly market prices or system operator dispatch.

For the UES of Ukraine and for similar power systems with NPPs supplying a substantial portion of the net load and/or with a significant share of variable energy sources, the flexible capabilities of NPPs are essential for maximizing revenues for reactor owners, ensuring system's reliability, reducing system's operational costs, integrating renewable energy, and reducing greenhouse gas emissions [21].

However, in literature nuclear units are typically represented as inflexible “must-run” (baseload) resources [19, 20, 22]. These traditional representations do not accurately capture the flexible capabilities of NPPs or the peculiar operational constraints arising from nuclear reactor dynamics and fuel irradiation cycles [21].

For example, pressurized water reactors (PWR), which are common in Ukraine and throughout the world, are capable of flexible operation by adjusting power output primarily by withdrawing neutron absorbing control rods into the core to increase power and inserting control rods to reduce power [21]. The PWR reactor operates in a double-circuit nuclear power system, and ordinary non-boiling water is a neutron moderator and coolant and is under high pressure ( $\sim 16$  MPa) [22]. Inserting or withdrawing control rods is an effective way of modulating power output for flexible operation, but the maximum rate at which reactors can adjust electricity production, or “ramp,” is constrained by limitations on the thermal and mechanical stresses incurred by nuclear fuel assemblies.

Depending on the design, French and German reactors can safely operate with ramp rates of up to 2–5.2% of rated power capacity per minute, without increasing the rate of fuel cladding failure [23] [24]. However, in practice ramp maneuvers performed by operators typically proceed at a more conservative pace (e.g., at  $< 0.5\%$  per minute) to limit stress on reactor components [21]. Existing nuclear plants in France and Germany contribute up to 5% of their maximum rated power to frequency regulation [23] [24].

## 2.4 Is it Safe to Invest in Nuclear Power?

Nuclear power plants are considered among the safest and most reliable installations in the world. But at the same time, accidents with negative consequences are possible. Today, along with accidents due to technical causes and human factors, nuclear energy engineers must reckon with the possibility of accidents due to military actions. A never known before situation occurred in 2022 at the Zaporizhzhia Nuclear Power Station (ZNPP), in the southeastern Ukraine, which is the largest nuclear power plant in Europe and among the 10 largest in the world.

The ZNPP has become the center of an ongoing nuclear safety crisis, also known as an act of nuclear terrorism by Russia, which is considered the most difficult situation of this kind in history [25]. The military forces of the Russian Federation captured the plant, destroyed the power station's infrastructure, damaged its power lines [25]. The potential threat from the development of events may exceed the scale of previous disasters at nuclear power plants [26].

According to the International Atomic Energy Agency (IAEA), the situation in Ukraine is unprecedented, and this is for the first time when an armed conflict continues on the territory of a large nuclear installation [27]. In their report, the IAEA expressed great concern regarding the situation and impact of the military

conflict at the ZNPP with respect to operating staff, physical integrity of the facilities, nuclear safety and security systems, communication and power supply [27].

In such a context, nuclear power plants can have threatening consequences for humanity and the environment. Can investing in nuclear energy be considered safe in the 21<sup>st</sup> century?

### 3 Regulation and Constraints on Flexible Operation of Nuclear Power Plants

#### 3.1 Modelling of Generation of Different Types of Power Plants

##### 3.1.1 Power Output of Solar Units

As the distributed generation penetration increases, it is necessary to possess generic models of distributed generators and appropriate power flow equivalents, especially in large scale power system models, for which modeling the distribution network is not feasible [28].

In general, it can be assumed that generation in distribution network not modeled in the power flow, but replaced by some combined resultant load and generation (or the sum of both that may results in negative load) may be considered as distributed generation [28]. In this study the modelled SPP represents an aggregated equivalent of a solar PV plant.

The solar irradiation data and the ambient temperature data were extracted from the Photovoltaic Geographical Information System (PVGIS) [29] for the geographical location of Southern Ukraine, latitude: 50°89', longitude: 34°8', as an example. It is assumed that the slope of the PV modules (i.e., the angle with the horizontal plane) is 37° for a fixed (non-solar) mounting type, the azimuth is -1°. The crystalline silicon photoelectric technology is considered. The PV electric output was estimated in accordance with [30]:

$$P_{PV} = \eta_{PV} \cdot A_{PV} \cdot G_{PV} \cdot \left(1 + \gamma (T_{PV} - T_{ref})\right), \quad (1)$$

where,  $P_{PV}$  is power produced from the PV system in kW;  $\eta_{PV}$  is the power conversion efficiency of the PV module in p.u.;  $\eta_{PC}$  is the efficiency of the power converter in p.u.;  $A_{PV}$  is the area of the PV array in m<sup>2</sup>;  $G_{PV}$  is the solar irradiance incident on the plane of the PV array in kW/m<sup>2</sup>;  $\gamma$  is the temperature coefficient of

the PV module;  $T_{PV}$  is the PV module temperature in °C; and  $T_{ref}$  is the reference temperature in °C.

### 3.1.2 Power Output of Nuclear Units

The output of the nuclear power units is regulated with regard to the ramp rate of the reactors, total power demand and amount of power output from PV installations:

$$P_i^{NPP} = \begin{cases} P_{i-1}^{NPP} (1 + K_{ramp}), & \frac{P_i^{\Sigma cons} \cdot \psi}{P_{i-1}^{NPP} + P_i^{SPP}} \geq 1 + K_{ramp} \\ P_{i-1}^{NPP} \left( \frac{P_i^{\Sigma cons} \cdot \psi}{P_{i-1}^{NPP} + P_i^{SPP}} \right), & \left[ 1 \leq \frac{P_i^{\Sigma cons} \cdot \psi}{P_{i-1}^{NPP} + P_i^{SPP}} < 1 + K_{ramp} \right] \vee \dots \\ \dots \vee \left[ 1 - K_{ramp} < \frac{P_i^{\Sigma cons} \cdot \psi}{P_{i-1}^{NPP} + P_i^{SPP}} < 1 \right] \\ P_{i-1}^{NPP} (1 - K_{ramp}), & \frac{P_i^{\Sigma cons} \cdot \psi}{P_{i-1}^{NPP} + P_i^{SPP}} \leq 1 - K_{ramp} \end{cases} \quad (2)$$

In (2)  $P_i^{NPP}$  is the instant active power output of the NPP at the  $i$ -th time step;  $P_i^{SPP}$  is the instant active power output of the SPP at the  $i$ -th time step;  $P_i^{\Sigma cons}$  is the total instant active power consumption at the  $i$ -th time step;  $\psi$  is the maximum possible share of NPPs in total energy production in the UES;  $K_{ramp}$  is the ramping rate of the NPP in p.u. per a time step. The coefficient  $\psi$  depends on the available capacity of nuclear power units and balancing capabilities of the UES and is assumed to be 0.6.

### 3.1.3 Power Output of Thermal Units

In this the TPP is considered the most maneuverable generation source in the UES, which can cover around 30% of the nominal power demand. Depending on the operational conditions and the load profile, the TPP's output can vary to match the demand and supply. In the model this type of source will be connected to a slack bus.

## 3.2 Operational Constraints

During the operation of the UES it is important to ensure that system's constraints are satisfied. At each step of the modelling the power system must meet operational constraints, such as power balance, voltage limit at each node, and transmission lines' current capacity limits. In this work the demand and generation values change in hourly steps. To simulate different operating states of the UES, power flow should be recalculated for all the snapshots of load demand values. The constraints are determined as follows [31].

Voltage limits constraints:

$$|V_n^{\min}| \leq |V_n| \leq |V_n^{\max}| \quad (3)$$

Branch capacity constraints:

$$\begin{aligned} |I_{fn}| &\leq |I_{fn}^{\max}| \\ |I_{rn}| &\leq |I_{rn}^{\max}| \end{aligned} \quad (4)$$

SPP real and reactive power constraints:

$$\begin{aligned} P_{\min}^{SPP} \leq P^{SPP} \leq P_{\max}^{SPP} \\ Q_{\min}^{SPP} \leq Q^{SPP} \leq Q_{\max}^{SPP} \end{aligned} \quad (5)$$

In the equations (3)-(5)  $V_i$  is the voltage at the  $n$ -th bus,  $I_{fn}$  is the forward flow capacity of the  $n$ -th branch of the UES;  $I_{rn}$  is the reverse flow capacity of the  $n$ -th branch of the UES;  $P^{SPP}$  and  $Q^{SPP}$  are the available real and reactive power capacities of the SPP. The superscripts and subscripts *min* and *max* represent the maximum and minimum allowable limits of the corresponding values. It is accepted in this work that voltage deviations should not exceed  $\pm 0.1$  p.u. threshold [32].

## 4 Case Study

The object under study is a UES with a significant share of NPPs, TPPs and SPPs, which in some approximation reminds the simplified energy system of Ukraine and some European countries. The IEEE 9-bus test system with the base 100 MVA was chosen to simulate such a UES. The diagram of the system is shown in Fig. 2.

The modified IEEE 9 bus system was modelled in PowerWorld simulator, and load flow studies were performed to assess the system's performance under different PV penetration levels, using Newton-Raphson method. The rated bus voltages, load values and transformers' impedances are in accordance with [33]. The overhead transmission lines are of 50 km length and have AC-240/32 wires with 605 A current capacity and 217 MW power capacity. The bus data and the rated load data is shown in Table 1, and the branch data is given in Table 2.

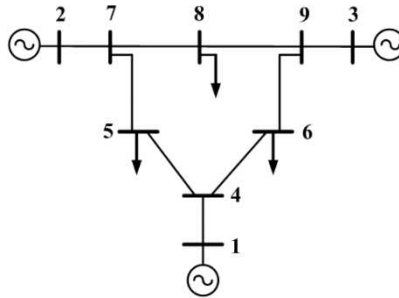


Figure 2

Single-line diagram of the IEEE 9-bus test system

Table 1  
Bus data for the power system under study

Bus No.	Bus type	Voltage, p.u.	Voltage, kV	Load	
				MW	Mvar
1	TPP (Slack)	1.04	16.5	0	0
2	NPP	1.025	18.0	0	0
3	SPP	1.025	13.8	0	0
4	PQ	1	230	0	0
5	PQ	1	230	125	50
6	PQ	1	230	90	30
7	PQ	1	230	0	0
8	PQ	1	230	100	35
9	PQ	1	230	0	0

Table 2  
Branch data for the power system under study

Line from	Line to	Resistance, $R$ , $\Omega/\text{km}$	Reactance, $X$ , $\Omega/\text{km}$	Conductivity, $B$ , $\text{S}/\text{km}$
1	4	0	0.0576	0
4	5	0.121	0.435	$2.6 \cdot 10^{-6}$
4	6	0.121	0.435	$2.6 \cdot 10^{-6}$
5	7	0.121	0.435	$2.6 \cdot 10^{-6}$
6	9	0.121	0.435	$2.6 \cdot 10^{-6}$
7	2	0	0.0625	0
7	8	0.121	0.435	$2.6 \cdot 10^{-6}$
9	3	0	0.0586	0
9	8	0.121	0.435	$2.6 \cdot 10^{-6}$

A single-line diagram of the UES modelled in PowerWorld simulator is shown in Fig. 3.

SPPs are the most unstable sources of the UES with a variable output. Scenarios with the SPPs’ installed capacity of 10%, 20%, 30%, 40%, 50%, 75% and 100% of the total system’s capacity are considered. The installed capacity of the solar generation units with regard to the total system’s capacity is further referred as the penetration level.

TPP power units are maneuverable generating capacities of the UES, and, therefore, they are located at the slack bus, which can adjust its output in wide limits to match the demand and supply.

NPPs are less maneuverable. In the UES of Ukraine the nuclear units usually operate in a “baseload” mode. For the first seven scenarios it is considered that the NPP operates with the ramp rate up to 2% of rated power per a time step, while the installed capacity of SPPs moderately changes from 10% to 100% of the power system’s capacity. For the next seven scenarios the NPP power units are considered to have more flexibility so that they are able to operate with the ramp rate of up to 20% per a time step. In this case the NPPs will better contribute to frequency regulation and provision of an operating reserve.

In total, there are fourteen scenarios that differ in the installed capacity of the SPPs and the NPPs’ flexibility. Their summary is given in Table 3.

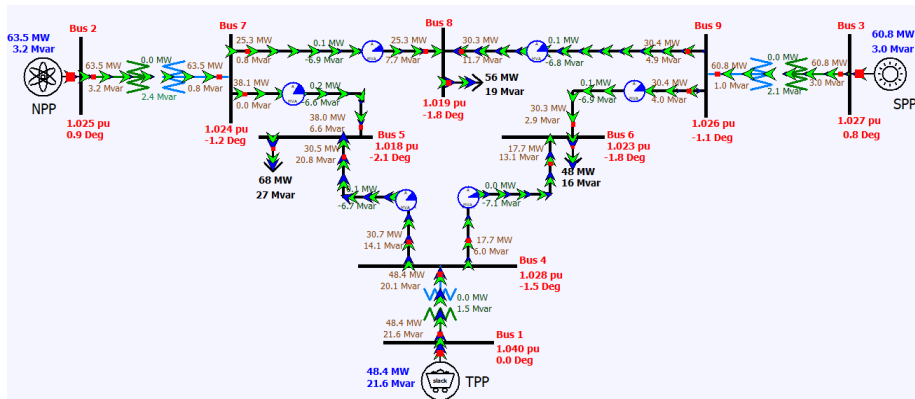


Figure 3

Single-line diagram of the UES in PowerWorld (the simulation is ongoing)

Table 3  
Scenarios for the case study

Scenarios	Description
1-7	The installed capacity of the SPPs is 10%, 20%, 30%, 40%, 50%, 75%, 100% of the total power system’s capacity. The NPPs have low flexibility and operate with the ramp rate up to 2% of the rated power per a time step.

8-14	The installed capacity of the SPP is 10%, 20%, 30%, 40%, 50%, 75%, 100% of the total power system's capacity. The NPPs have higher flexibility and operate with the ramp rate up to 20% of the rated power per a time step.
------	---

## 5 Results and Discussion

The simulated scenarios are operationally feasible, i.e., power flow converged successfully, and none of the established constraints were violated. The results of the simulation are given in Table 4.

Table 4  
Simulation results for different scenarios

Scenario	TPP share, p.u.	NPP share, p.u.	SPP share, p.u.	Power Loss share, p.u.	PV curtailment necessary?	PV curtailment, %
1	41.35	56.29	2.37	0.67	No	0
2	41.70	53.56	4.74	0.65	No	0
3	40.94	51.95	7.11	0.64	Yes	$9.02 \cdot 10^{-5}$
4	39.58	50.95	9.48	0.64	Yes	$6.9 \cdot 10^{-2}$
5	38.05	50.11	11.84	0.66	Yes	0.47
6	33.44	48.81	17.75	0.76	Yes	3.21
7	28.64	47.75	23.61	0.96	Yes	7.06
8	41.35	56.29	2.37	0.67	No	0
9	41.70	53.56	4.74	0.64	No	0
10	40.94	51.95	7.11	0.63	No	0
11	39.58	50.95	9.48	0.64	No	0
12	38.05	50.11	11.84	0.66	Yes	$13.32 \cdot 10^{-4}$
13	33.44	48.81	17.75	0.77	Yes	0.64
14	28.64	47.75	23.61	0.94	Yes	3.23

The voltage variations were checked for different operating conditions, and the voltage levels in the nodes were found to be within the established limits (i.e., deviations do not exceed  $\pm 0.1$  p.u. threshold). As an example, a color map visualization with the voltage levels is shown in Fig. 4 (a capture during the running scenario 7).

The “colder” colors correspond to lower bus voltage levels (i.e., below 1.0 p.u.), and the “warmer” colors – to higher bus voltage levels (i.e., above 1.0 p.u.).

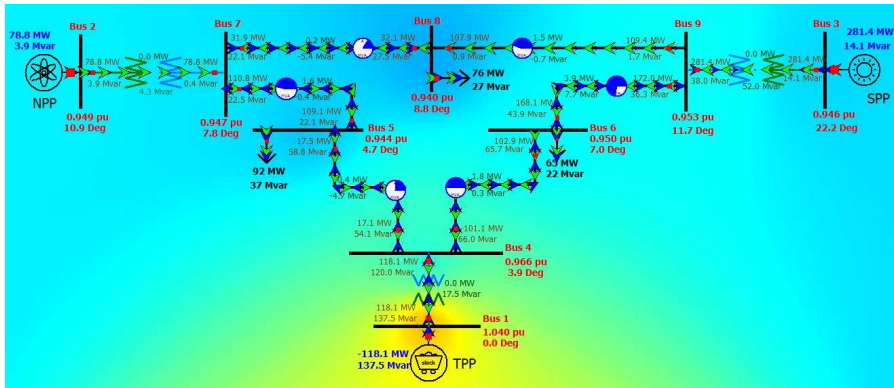


Figure 4

Voltage color map for the UES in PowerWorld (scenario 7)

Dependences of the share of thermal and nuclear power units in the energy generation balance of the UES from PV penetration are shown in Fig. 5. For the scenarios with mild ramp rate of the NPPs (i.e., baseload operation) the shares of TPPs and NPPs in energy generation mix both decrease with the increase of the PV penetration. For the scenarios with additional flexibility of NPPs the share of the NPPs in energy generation mix constantly decreases, while the share of the TPPs moderately increases until the PV penetration level of 50%. Further the share of the TPPs starts to decrease, but its declining proceeds notably slower than the declining of the NPPs.

Comparing flexible and inflexible operation of the nuclear, the share of NPPs in the total generation mix is higher with the NPPs' ramp rate of 20% than with the NPPs' ramp rate of 2% until the PV penetration reaches 30%. At the same time, the share of TPPs in the total energy generation mix is lower with the NPPs' ramp rate of 20% than with the NPPs' ramp rate of 2% until the PV penetration reaches 30%. This means that flexible operation of nuclear units allows to better engage them in the demand-supply balancing and to reduce the share of environmentally unfriendly thermal power units. However, when the PV penetration exceeds 30%, the situation changes to the opposite. This can be explained by the peculiarities of NPP regulation under high penetration of RESs. Thus, higher PV penetrations, reduce the value of nuclear flexibility and enhance demand for reserves. Forecasting of solar generation and scheduling of NPPs with regard to the expected SPPs output can be a helpful measure to increase the share of cleaner energy technologies.

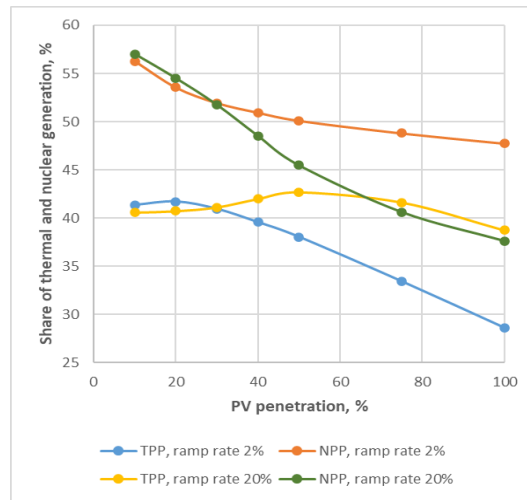


Figure 5

Dependences of the share of TPPs and NPPs in total energy generation

Comparison of power losses in the energy system with different ramp rates of the NPPs is shown in Fig. 6. As it can be seen, additional flexibility of the NPPs has negligible influence on the power losses.

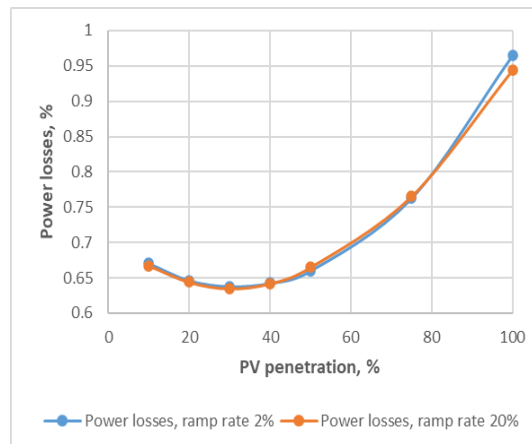


Figure 6

Comparison of power losses in the energy system with different ramp rates of the NPP

Additionally, nuclear flexibility allows to significantly reduce PV curtailment in the system. For example, at high PV penetrations of 75% and 100% (scenarios 13 and 14) the PV curtailment with flexible nuclear power is 0.64% and 3.23% accordingly, while 3.21% and 7.06% of PV generation must be curtailed when there are inflexible nuclear power units in the energy system (scenarios 6 and 7).

## Conclusions

Many countries and regions have policy targets in place, which steer the energy system towards meeting future demands for clean, reliable and affordable energy services, using PV and wind technologies. However, high penetration levels of PV in the united energy systems can violate demand-supply balance, cause issues with frequency control and complicate demand-supply management. While TPPs have the best maneuverable generating capacities, NPPs can also contribute to the demand and supply balancing in the UES.

In this paper the potential impacts of flexible nuclear operations within an energy system with a significant share of NPPs, high solar penetration and a strong transmission system has been investigated. The results have shown that a flexible nuclear operation can substantially reduce curtailment of renewables and, in some cases, reduce the share of environmentally unfriendly thermal energy. Higher than a 30% PV penetration reduces the value of nuclear flexibility and enhances the demand for reserves. Forecasting of solar generation and scheduling of NPPs with regard to the expected SPPs output can be a helpful measure to increase the share of cleaner energy technologies, such as nuclear and renewable energy.

Although the numerical results are case specific, the flexible operation of nuclear power stations is likely to yield similar benefits in power systems with comparable shares of RESs and NPPs.

A rigorous sensitivity analysis, exploring which factors are most crucial for economic benefits of nuclear flexibility, would be a productive avenue for future work.

## Acknowledgements

This work was supported by the Ministry of Education, Science, Research and Sport of the Slovak Republic and the Slovak Academy of Sciences under the contract VEGA 1/0757/21. This work was supported by the Slovak Research and Development Agency under the contract No. APVV-19-0576.

## References

- [1] International Energy Agency. World Energy Outlook 2021. IEA Publications, 2021
- [2] J. Schleich. “Energy efficiency: What are the global energy challenges? MOOC: New Energy Technologies - Energy Transition and Sustainable Development,” 2017 [Online] Available: <https://en.grenoble-em.com/mooc-new-energy-technologies> [Accessed Oct. 03, 2022]
- [3] J. Schleich. “Energy efficiency: How is policy fostering energy efficiency? MOOC: New Energy Technologies - Energy Transition and Sustainable Development,” 2017 [Online] Available: <https://en.grenoble-em.com/mooc-new-energy-technologies> [Accessed Oct. 03, 2022]

- [4] M. Olsthoorn, “Energy efficiency: Energy efficiency markets and trends? MOOC: New Energy Technologies - Energy Transition and Sustainable Development,” 2017 [Online] Available: <https://en.grenoble-em.com/mooc-new-energy-technologies> [Accessed Oct. 03, 2022]
- [5] F. Gafaro, “Planning the operability of power systems – Overcoming technical and operational bottlenecks,” 2017 [Online] Available: <https://www.irena.org/-/media/Files/IRENA/Agency/Events/2017/Jan/17/IRENA-WFES-Scaling-up-VRE---Operation-Planning---Final.pdf>. [Accessed Oct. 03, 2022]
- [6] K. Ogimoto, “Power System Operation and Augmentation Planning with PV Integration,” Report IEA PVPS T14-04:2014, 2015
- [7] “The share of thermal generation in total electricity production has decreased by 5% since 2016” [in Ukrainian], 2021 [Online] Available: [http://mpe.kmu.gov.ua/minugol/control/publish/article?art\\_id=245538724](http://mpe.kmu.gov.ua/minugol/control/publish/article?art_id=245538724). [Accessed Apr. 30, 2022]
- [8] U. Terletska, “Renewable energy in Ukraine (RES) is reality,” 2019. [Online] Available: <http://www.institute.lviv.ua/index.php/uk/2018-02-16-08-36-56/126-2019-11-15-11-44-25>. [Accessed Apr. 30, 2022]
- [9] “The capacity of RESs in Ukraine in 2021 increased by almost a third, SPP – by less than 5%” [in Ukrainian] 2022 [Online] Available: <https://greendeal.org.ua/potuzhnist-ves-v-ukrayini-za-pidsumkamy-2021-roku-zrosla-majzhe-na-tretynu-ses-menshe-nizh-na-5/>. [Accessed Apr. 30, 2022]
- [10] V. V. Volokhin, I. M. Diahovchenko, and B. V. Derevyanko, “Electric energy accounting and power quality in electric networks with photovoltaic power stations,” 2017 IEEE International Young Scientists Forum on Applied Physics and Engineering (YSF), 2017, pp. 36-39, doi: 10.1109/YSF.2017.8126588
- [11] I. M. Diahovchenko and Z. Viacheslav, “Optimal composition of alternative energy sources to minimize power losses and maximize profits in distribution power network,” 2020 IEEE 7<sup>th</sup> International Conference on Energy Smart Systems, ESS 2020 – Proceedings, 2020, pp. 247-252, doi: 10.1109/ESS50319.2020.9160259
- [12] O. Chernousenko, “The state of energy of Ukraine and the results of modernization of TPP power units” [in Ukrainian] Problems of general energy, Vol. 39, No. 4, pp. 20-28, 2014
- [13] M. P. Kuznetsov, O. V. Lysenko, and O. A. Melnyk, “Optimal regulation of a local power system with renewable energy sources” [in Ukrainian], Bulletin of the National Technical University “KhPI”, Vol. 2, No. 1, pp. 52-61, 2021

- 
- [14] V. F. Nakhodov, "Management of consumption regimes and efficiency of electricity use in energy systems" [in Ukrainian] Doctoral thesis, Kuiv, 2018
- [15] G. Morva and I. Diahovchenko, "Effects of COVID-19 on the electricity sectors of Ukraine and Hungary: challenges of energy demand and renewables integration," 2020 IEEE 3<sup>rd</sup> International Conference and Workshop in Óbuda on Electrical and Power Engineering (CANDO-EPE) 2020, pp. 000041-000046, doi: 10.1109/CANDO-EPE51100.2020.9337785
- [16] V. P. Severin et. al., "The problem of maneuverability of the NPP power unit and development of the models of its control systems" [in Ukrainian], Bulletin of the National Technical University "KhPI", Vol. 1103, No. 61, pp. 24-29, 2014
- [17] P. D. Lund, J. Lindgren, J. Mikkola, and J. Salpakari, "Review of energy system flexibility measures to enable high levels of variable renewable electricity," *Renewable and Sustainable Energy Reviews*, Vol. 45, pp. 785-807, 2015, doi: 10.1016/j.rser.2015.01.057
- [18] A. Pfeifer, L. Herc, I. B. Bjelić, and N. Duić, "Flexibility index and decreasing the costs in energy systems with high share of renewable energy," *Energy Conversion and Management*, Vol. 240, 114258, 2021, doi: 10.1016/j.enconman.2021.114258
- [19] S. Impram, S. Varbak Nese, and B.t Oral, "Challenges of renewable energy penetration on power system flexibility: A survey," *Energy Strategy Reviews*, Vol. 31, 100539, 2020, doi: 10.1016/j.esr.2020.100539
- [20] What to know about the "conflict" between nuclear and renewable energy, 2020 [Online] Available: <https://ecoaction.org.ua/renewables-vs-nuke.html> [Accessed Apr. 30, 2022]
- [21] J. D. Jenkins et. al., "The benefits of nuclear flexibility in power system operations with renewable energy," *Applied Energy*, Vol. 222, pp. 872-884, 2018, doi: 10.1016/j.apenergy.2018.03.002
- [22] K. B Denisevich et. al., "Energy: history, present and future. Development of nuclear energy and integrated energy systems," Kyiv, 2011
- [23] Lokhov A. "Technical and Economic Aspects of Load Following with Nuclear Power Plants." Paris: Nuclear Energy Agency, 2011. Available: <https://www.oecd-nea.org/ndd/reports/2011/load-following-npp.pdf>
- [24] H. Ludwig, T. Salnikova, A. Stockman, and U. Waas, "Load cycling capabilities of German Nuclear Power Plants (NPP)," *International Journal for Nucl Power*, Vol. 55, No. 8/9, pp. 2-8, 2010
- [25] "The russian military shelling ZNPP to destroy its infrastructure and disconnect it from the Ukrainian power system." *EnergoAtom*, 2022 [Online] Available: <https://www.energoatom.com.ua/app-eng/eng-0608221.html>. [Accessed Oct. 03, 2022]
-

- [26] “The situation is close to Fukushima, there is no help from the world.” Interview with the engineer of the Zaporizhzhya NPP, 2022 [in Ukrainian] [Online] Available: <https://www.bbc.com/ukrainian/features-62532425>. [Accessed Oct. 03, 2022]
- [27] Nuclear Safety, Security and Safeguards in Ukraine: 2nd Summary Report by the Director General, 28 April – 5 September 2022, IAEA, Vienna, 2022 [Online] Available: [https://www.iaea.org/sites/default/files/22/09/ukraine-2ndsummaryreport\\_sept2022.pdf](https://www.iaea.org/sites/default/files/22/09/ukraine-2ndsummaryreport_sept2022.pdf) [Accessed Oct. 03, 2022]
- [28] A. Semerow et al., “Dynamic Study Model for the interconnected power system of Continental Europe in different simulation tools,” 2015 IEEE Eindhoven PowerTech, 2015, pp. 1-6
- [29] “Photovoltaic Geographical Information System (PVGIS),” European Commission Joint Research Centre, 2022
- [30] I. Diahovchenko, L. Petrichenko, “Comparative Analysis of Power Distribution Systems with Individual Prosumers Owing Photovoltaic Installations and Solar Energy Communities in Terms of Profitability and Hosting Capacity,” *Energies*, Vol. 15, No. 23, 8837, 2022, doi: 10.3390/en15238837
- [31] I. M. Diahovchenko, G. Kandaperumal, A. K. Srivastava, Z. I. Maslova, and S. M. Lebedka., “Resiliency-driven strategies for power distribution system development,” *Electric Power Systems Research*, Vol. 197, 107327, 2021, doi: 10.1016/j.epsr.2021.107327
- [32] I. Diahovchenko, N. Sushchenko, A. Shulumei, and O. Strokin, “Influence of supply voltage and frequency variations on the electrical equipment and power consumption in LV and MV distribution networks,” *Energetika*, Vol. 65, No. 4, pp. 172-187, 2019, doi: 10.6001/energetika.v65i4.4246
- [33] M. Anderson, *Power System Control and Stability*, 2<sup>nd</sup> edition, IEEE Press Power Engineering Series, 2003

# The Role of Flexibility Resources in the Energy Transition

**Nikolaos Koltsaklis and Jaroslav Knápek**

Department of Economics, Management and Humanities, Czech Technical University in Prague, Faculty of Electrical Engineering, Prague, Czech Republic, koltsnik@fel.cvut.cz; knapek@fel.cvut.cz

---

*Abstract: Extremely adaptable power systems are required, as the share of variable renewable energy sources increases. The variable renewable energy sources' ability to be installed on the grid, is frequently thought to be constrained by a limited flexible capacity. A general, methodological framework, for the optimal scheduling of an islanded power system, with a variety of flexibility resources, is presented in this work. In particular, it takes into account a significant amount of intermittent RES and the widespread use of electric vehicles that offer charging and discharging options. The modeling in this work also considers demand response programs' active market participation and the installation of energy storage capacities. Additionally, it covers the involvement of electricity interconnections, as a source of flexibility. Two illustrative case studies of an island power system connected to a mainland power system, have been used, to evaluate the applicability of the proposed strategy. The scheduling framework is daily, with an hourly interval. The results of the modeling show how important all of the flexibility resources are, for effective energy management and the supply of ancillary services, especially in cases for high-RES penetration. The proposed method can be used by market operators, policymakers and regulatory authorities, to choose the best system development, market design and portfolio synthesis.*

*Keywords: optimization; island system; flexibility; interconnection; energy storage; demand response*

---

## 1 Introduction

The availability of domestic energy resources and/or their importing options via available transportation means, the system-wide energy requirements that must be met, and the applied energy policy decision-making based on a series of factors such as economic, historical, social, environmental, demographic, institutional and/or geopolitical ones, are the key factors that determine the synthesis of the energy supply mix for each energy system. Especially recently, the issue of energy security has been gaining importance, both with regard to the availability of primary

energy sources and the reliability of power systems in relation to the growing share of volatile renewable sources.

The rapidly growing share of electricity generation plants, based on volatile RES, together with the changes in the structure and functioning of the energy sector, brought about by progressive decarbonization, among other things, increase the importance of modeling the further development of energy systems. One of the key aspects of modeling is the issue of "generation adequacy", i.e., the search for such an arrangement of the electricity system structure (system elements, internal links between them, and links of the system to surrounding systems) that ensures energy security both in terms of short-term operation of the system (reliability of electricity supply) and in terms of long-term development of the energy system [1].

A series of works have been presented in the literature investigating the combined optimization of energy and reserves, dealing with the various aspects of generation adequacy and energy security. [2] highlights the increasing complexity of models reflecting the changing structure of the electricity industry, as a sector and a range of new constraints and target values. At the same time, [2] points out that models are often based on different assumptions, using different modeling approaches. This in turn, often leads to a wide dispersion of modeling results and the results of different models are often difficult to compare. In relation to this, it emphasizes the transparency of the description of the models, the assumptions used, and the modelling techniques. For example, [3] compares nine power sector models. Similar to [2], it highlights the differences between the models, both in the application of various constraints and in terms of the data used. In particular, they highlight differences in the ways in which the impact of EVs, pumped storage and demand response are captured. A survey of modeling techniques and trends in the co-optimization of the energy and reserves markets was provided by the authors in [4]. In [5], the authors formulated two approaches for clearing the energy and spinning reserve markets while examining the effects of demand involvement in the reserve offers. Investigation on the impact of demand flexibility on the clearing of the energy and reserves markets can be found in [6]. The thermal unit commitment problem has been studied through a mixed-integer linear programming (MILP) model in [7]. A version with a comparable unit commitment has also been given in [8]. A co-optimization strategy for energy-reserve power markets has been introduced in [9]. The authors of [10] presented a MILP model for the joint clearance of energy and reserve power exchanges by integrating the hourly offers module of EUPHEMIA (pan-EUroPean Hybrid Electricity Market Integration Algorithm) with particular unit commitment constraints. Additionally, the same authors in [11] studied the market products offered by EUPHEMIA for the interconnected Greek electricity grid. In addition, the authors of [12] created an optimization model for deciding how to dispatch energy and reserves in electricity markets. The authors of [13] developed a methodological approach for integrating bidding schemes, in day-ahead energy and spinning reserve markets, focusing on the bidding strategies. For a generation business to optimize its economic profit in

day-ahead energy and spinning reserve markets, the authors in [14] devised an optimization model for the optimal bidding strategy problem. The authors in [15], focused on islanded power systems and underscored the role that electricity interconnection plays in meeting reserve requirements.

This paper proposes an optimization approach for the optimal scheduling of energy and reserves for an island power system, taking into account the involvement of thermal power plants, renewable energy sources, an energy storage system, electric vehicles, and demand response initiatives (DRPs). The work's consideration of the activation of electricity interconnections as a provider of flexibility services is a significant contribution. The mathematical model will be used to make operational decisions on the examined power system's energy generation mix, reserve provision mix, and quantification of flexibility provided by ESS, EVs, DRPs, and electricity interconnection.

The remaining parts of this paper are arranged as follows: The problem to be solved is defined in Section 2, and the mathematical model's explanation is provided in detail. Section 3 also provides a description of the case study and the relevant input data, and Section 4 provides a comprehensive discussion of the model outputs to highlight the main findings. Last but not least, Section 5 provides a summary of the primary conclusions.

## **2 Methodology**

### **2.1 Objective Function**

The optimization model co-optimizes the energy and reserves scheduling of an island that is interconnected with the mainland power system from the system operator's perspective. A flowchart of the proposed methodological approach is depicted in Figure 1.

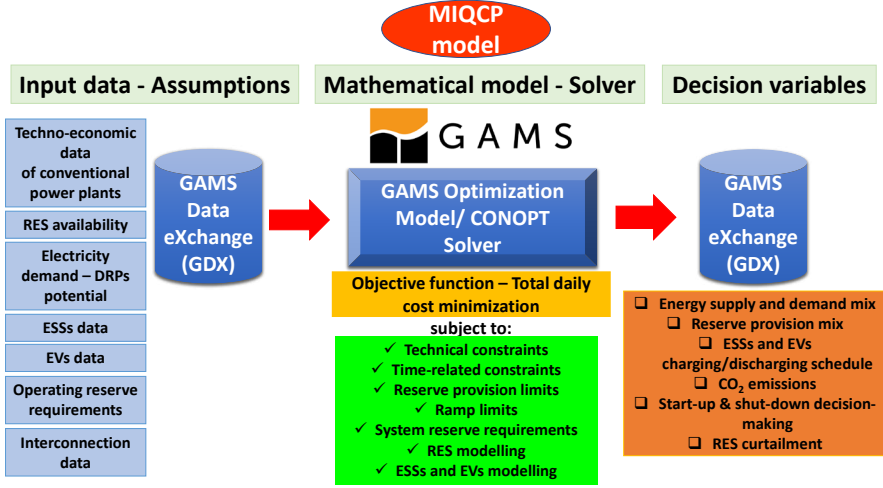


Figure 1

Superstructure of the proposed methodological approach

The mathematical model's objective function to be minimized refers to the net daily cost (1), including the following components:

- (i) Electricity production cost of installed diesel-fired power generators
- (ii) Start-up costs of diesel-fired power generators
- (iii) RES curtailment cost
- (iv) Operating reserve-up and -down provision cost

$$MinC^{oper} =$$

$$\begin{aligned}
 & \overbrace{\sum_i \sum_t C_{i,t}^{prod}}^{\text{Energy supply cost from thermal power units}} + \overbrace{\sum_i \sum_t C_i^{stup} \cdot y_{i,t}}^{\text{Thermal power units start-up cost}} \\
 & + \overbrace{\sum_r \sum_t C_{r,t}^{curt} \cdot p_{r,t}^{curt}}^{\text{RES curtailment cost}} + \overbrace{\sum_n \sum_t C_{n,t}^{up} \cdot r_{n,t}^{up}}^{\text{Reserve up cost}} \\
 & + \overbrace{\sum_m \sum_t C_{m,t}^{dn} \cdot r_{m,t}^{dn}}^{\text{Reserve down cost}}
 \end{aligned} \tag{1}$$

## 2.2 Electricity Supply and Demand Balance

The energy demand balance of the studied islanded power system is formulated in Equation (2). More specifically, the electricity supply from diesel-fired power generators ( $\sum_i p_{i,t}^{conv}$ ), renewable energy sources ( $\sum_r p_{r,t}^{res}$ ), power discharge from ESSs ( $\sum_w p_{w,t}^{dis}$ ) and EVs ( $\sum_v p_{v,t}^{dis} \cdot n_v^{tot}$ ), and electricity imports from the mainland power system ( $imp_t$ ) must satisfy the final electricity demand after potential activation of demand response programs ( $\sum_y d_{y,t}^{cl}$ ), the electricity exports to the mainland power system ( $exp_t$ ) and the charging requirements from both ESSs ( $\sum_w p_{w,t}^{ch}$ ) and EVs ( $\sum_v p_{v,t}^{ch} \cdot n_v^{tot}$ ) in each time interval.

$$\begin{aligned} & \sum_i p_{i,t}^{conv} + \sum_r p_{r,t}^{res} + \sum_v p_{v,t}^{dis} \cdot n_v^{tot} + \sum_w p_{w,t}^{dis} \\ & + imp_t = \sum_y d_{y,t}^{cl} + \sum_v p_{v,t}^{ch} \cdot n_v^{tot} + \sum_w p_{w,t}^{ch} + exp_t \end{aligned} \quad \forall t \quad (2)$$

## 2.3 Technical Constraints

The production cost of each diesel-fired power generator ( $C_{i,t}^{prod}$ ) is calculated by Equation (3), and is a function of its electricity output ( $p_{i,t}^{conv}$ ) and its specific cost coefficients ( $a_i$ ,  $b_i$ , and  $c_i$ ). The operational range of each diesel-fired power generator, both maximum ( $P_i^{max}$ ) and minimum ( $P_i^{min}$ ), is bounded by constraints (4) and (5). Both constraints take into account the power unit's participation in energy ( $p_{i,t}^{conv}$ ) and reserves-up ( $r_{i,t}^{up}$ ) and down ( $r_{i,t}^{dn}$ ) scheduling, subject also to the decision of its operation or not ( $x_{i,t}^{oper}$ ). Furthermore, constraints (6) and (7) set the ramp limits, both up ( $RU_i$ ) and down ( $RD_i$ ), of each diesel-fired power generator. In addition, Constraint (8) determines the minimum uptime ( $UT_i$ ) of each diesel-fired power generator after its start-up decision ( $y_{i,t}$ ), as well as Constraint (9), describes the minimum downtime ( $UT_i$ ) of each diesel-fired power generator after its shut-down decision ( $z_{i,t}$ ). Finally, Equation (10) is a logical one, correlating operation, start-up, and shut-down decision-making.

$$C_{i,t}^{prod} = a_i \cdot (p_{i,t}^{conv})^2 + b_i \cdot p_{i,t}^{conv} + c_i \quad \forall i, t \quad (3)$$

$$p_{i,t}^{conv} + r_{i,t}^{up} \leq P_i^{max} \cdot x_{i,t}^{oper} \quad \forall i, t \quad (4)$$

$$p_{i,t}^{conv} - r_{i,t}^{dn} \geq P_i^{min} \cdot x_{i,t}^{oper} \quad \forall i, t \quad (5)$$

$$(p_{i,t}^{conv} + r_{i,t}^{up}) - (p_{i,t-1}^{conv} + r_{i,t-1}^{dn}) \leq RU_i \quad \forall i, t \quad (6)$$

$$(p_{i,t-1}^{conv} + r_{i,t-1}^{up}) - (p_{i,t}^{conv} - r_{i,t}^{dn}) \leq RD_i \quad \forall i, t \quad (7)$$

$$\sum_{t'=t-UT_i+1}^t y_{i,t'} \leq x_{i,t}^{oper} \quad \forall i, t \quad (8)$$

$$\sum_{t'=t-DT_i+1}^t z_{i,t'} \leq 1 - x_{i,t}^{oper} \quad \forall i, t \quad (9)$$

$$y_{i,t} - z_{i,t} = x_{i,t}^{oper} - x_{i,t-1}^{oper} \quad \forall i, t \quad (10)$$

## 2.4 RES Modeling

The upper production potential of each RES in each time interval ( $F_{r,t}$ ) is imposed by Constraint (11). In particular, it equals the amount that is directly utilized ( $p_{r,t}^{res}$ ) and the other one that is curtailed ( $p_{r,t}^{curt}$ ). Furthermore, Constraint (12) sets a maximum limit on the reserve-down supply potential of each RES in each time interval ( $r_{r,t}^{dn}$ ).

$$p_{r,t}^{res} + p_{r,t}^{curt} \leq F_{r,t} \quad \forall r, t \quad (11)$$

$$p_{r,t}^{res} - r_{r,t}^{dn} \geq 0 \quad \forall r, t \quad (12)$$

## 2.5 Electricity Exchanges Modeling

The energy and reserve exchanges with the mainland power system are formulated in Constraints (13)-(16). More specifically, Constraint (13) sets the maximum value ( $IMP_t^{cap}$ ) of electricity imports ( $imp_t$ ) and operating reserve-up ( $r_t^{up}$ ) supply from the mainland power system. In the same context, Constraint (14) describes the respective upper capability of reserve-down provision ( $r_t^{dn}$ ). Last but not least, Constraints (15) and (16) set the corresponding limits for the case of electricity exports and reserve exchanges to the mainland power system.

$$imp_t + r_t^{up} \leq IMP_t^{cap} \quad \forall t \quad (13)$$

$$imp_t - r_t^{dn} \geq 0 \quad \forall t \quad (14)$$

$$exp_t + r_t^{dn} \leq EXP_t^{cap} \quad \forall t \quad (15)$$

$$exp_t - r_t^{up} \geq 0 \quad \forall t \quad (16)$$

## 2.6 ESSs Modeling

Constraint (17) quantifies the state-of-charge balance level of each ESS in each time interval. ( $soC_{w,t}^{st}$ ), considering both charging ( $SF_w^{ch}$ ) and discharging efficiencies ( $SF_w^{dis}$ ) for charging ( $p_{w,t}^{ch}$ ) and discharging ( $p_{w,t}^{dis}$ ) modes, correspondingly.

Moreover, the upper charging ( $G_w^{ch-max}$ ) and discharging limits ( $G_w^{dis-max}$ ) of each ESS are expressed by Constraints (18) and (19), respectively, considering its participation in both energy ( $p_{w,t}^{ch}$  and  $p_{w,t}^{dis}$ ) and reserve ( $r_{w,t}^{dn}$  and  $r_{w,t}^{up}$ ) markets. Also, constraints (20) and (21) guarantee that ESS energy level and reserve schedules are within the allowable bounds, both minimum ( $SOC_w^{min}$ ) and maximum ( $SOC_w^{max}$ ), respectively.

$$soc_{w,t}^{st} = soc_{w,t-1}^{st} + p_{w,t}^{ch} \cdot SF_w^{ch} - \frac{p_{w,t}^{dis}}{SF_w^{dis}} \quad \forall w, t \quad (17)$$

$$p_{w,t}^{ch} + r_{w,t}^{dn} \leq G_w^{ch-max} \quad \forall w, t \quad (18)$$

$$p_{w,t}^{dis} + r_{w,t}^{up} \leq G_w^{dis-max} \quad \forall w, t \quad (19)$$

$$soc_{w,t}^{st} - \frac{r_{w,t}^{up}}{SF_w^{dis}} \geq SOC_w^{min} \quad \forall w, t \quad (20)$$

$$soc_{w,t}^{st} + r_{w,t}^{dn} \cdot SF_w^{ch} \leq SOC_w^{max} \quad \forall w, t \quad (21)$$

## 2.7 EVs Modeling

The corresponding EV modeling is formulated analogously to the ESS one by Constraints (22-26). More specifically, Equation (22) sets the state-of-charge level in each time interval ( $soc_{v,t}^{ev}$ ), as well as constraints (23) and (24) impose the maximum limits on charging ( $G_v^{ch-max}$ ) and discharging decision-making ( $G_v^{dis-max}$ ), taking into account their involvement in both energy and reserve markets. Finally, constraints (25) and (26) guarantee that EV energy levels and reserve schedules are within specific imposed energy limits.

$$soc_{v,t}^{ev} = soc_{v,t-1}^{ev} + p_{v,t}^{ch} \cdot SF_v^{ch} \cdot n_v^{tot} - \frac{(p_{v,t}^{dis} + E_{v,t}^{cons})}{SF_v^{dis}} \quad \forall v, t \quad (22)$$

$$p_{v,t}^{ch} + r_{v,t}^{dn} \leq G_v^{ch-max} \quad \forall v, t \quad (23)$$

$$p_{v,t}^{dis} + r_{v,t}^{up} \leq G_v^{dis-max} \quad \forall v, t \quad (24)$$

$$soc_{v,t}^{ev} - \frac{r_{v,t}^{up}}{SF_v^{dis}} \geq SOC_v^{min} \quad \forall v, t \quad (25)$$

$$soc_{v,t}^{ev} + r_{v,t}^{dn} \cdot SF_v^{ch} \leq SOC_v^{max} \quad \forall v, t \quad (26)$$

## 2.8 DRPs Modeling

Constraints (27-30) formulate the DRPs modeling. In particular, Equation (27) describes the amount of the modified energy demand ( $d_{y,t}^{cl}$ ), taking into account the applied DRPs ( $d_{y,t}^{up}$  and  $d_{y,t}^{dn}$ ) upon the reference electricity demand ( $D_{y,t}^{ref}$ ).

Equation (28) ensures that the total energy demand is at the same levels over the scheduling time horizon. Finally, constraints (29-30) set the minimum ( $D_{y,t}^{min}$ ) and maximum ( $D_{y,t}^{max}$ ) demand variation ranges, respectively.

$$d_{y,t}^{cl} = D_{y,t}^{ref} + d_{y,t}^{up} - d_{y,t}^{dn} \quad \forall y, t \quad (27)$$

$$\sum_t d_{y,t}^{up} = \sum_t d_{y,t}^{dn} \quad \forall y \quad (28)$$

$$d_{y,t}^{cl} - r_{y,t}^{up} \geq D_{y,t}^{min} \quad \forall y, t \quad (29)$$

$$d_{y,t}^{cl} + r_{y,t}^{dn} \leq D_{y,t}^{max} \quad \forall y, t \quad (30)$$

## 2.9 System Reserve Requirements

Constraints (31) and (32) determine the system operating reserve requirements in both upward ( $R_t^{up}$ ) and downward ( $R_t^{dn}$ ) directions, respectively.

$$\sum_i r_{i,t}^{up} + \sum_w r_{w,t}^{up} + \sum_v r_{v,t}^{up} + \sum_y r_{y,t}^{up} + r_t^{up} \geq R_t^{up} \quad \forall t \quad (31)$$

$$\sum_i r_{i,t}^{dn} + \sum_w r_{w,t}^{dn} + \sum_v r_{v,t}^{dn} + \sum_y r_{y,t}^{dn} + \sum_r r_{r,t}^{dn} + r_t^{dn} \geq R_t^{dn} \quad \forall t \quad (32)$$

The objective function (1) to be minimized is included in the overall optimization problem, which is expressed as a mixed-integer quadratically constrained programming problem that is subject to the imposed constraints and equations (2)-(32).

## 3 Case Study

The developed optimization model has been tested on an illustrative case study of an islanded power system. In particular, the four diesel-fueled power units of the chosen islanded power system are detailed in their techno-economic characteristics in Tables 1 and 2. These data include the start-up cost, the technical minimums and maximums, the ramp limits, and the minimum uptimes and downtimes for each diesel-fired unit.

Wind turbines account for 200 MW, and solar photovoltaics for the remaining 80 MW of the 280 MW installed capacity in addition to the diesel-fueled generators. The daily reference electricity demand and the RES potential for each technology type over each time period are depicted in Figure 2.

Table 1  
Economic data of the studied power system

Diesel-fired generator $i$	a (€/MW <sup>2</sup> )	b (€/MW)	c (€)	Start-up cost (€)
Diesel-1	3	20	100	50000
Diesel-2	4.05	18.07	98.87	50000
Diesel-3	3.99	19.21	107.2	50000
Diesel-4	3.88	26.18	95.31	50000

Table 2  
Technical data of the studied power system

Diesel-fired generator $i$	Technical minimum (MW)	Technical maximum (MW)	Ramp-up and down (MW/min)	Minimum uptime (h)	Minimum downtime (h)
Diesel-1	28	150	4	16	1
Diesel-2	20	120	3	16	1
Diesel-3	30	100	3	16	1
Diesel-4	20	200	5	16	1

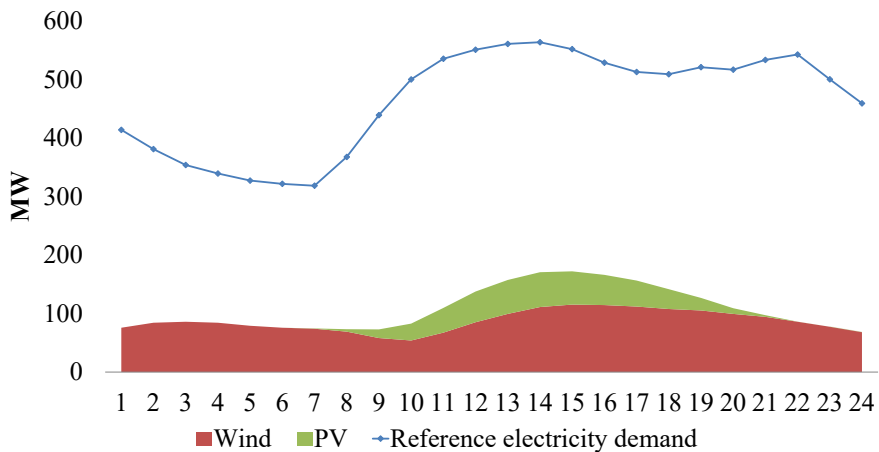


Figure 2  
Reference electricity demand and RES potential per technology type in each time period

The battery capacity, the initial energy storage level, the charging and discharging efficiencies, the minimum allowable energy storage level, and the charging and discharging rates of the ESS considered are all shown in Table 3.

Table 3  
ESS operational data

<b>ESS data</b>	<b>Value</b>
Battery capacity (MWh)	50
Initial storage level (MWh)	25
Charging efficiency (%)	0.95
Discharging efficiency (%)	0.9
Minimum battery energy storage level (MWh)	5
Charging rate (MW)	50
Discharging rate (MW)	50

Table 4 presents the operational data of the considered EVs, including the number of EVs (1000 in total), the battery capacity, the charging and discharging efficiencies, as well as the charging and discharging rates. Each electric vehicle is assumed to have a minimum energy storage level equal to 10% of its battery capacity, and the initial energy storage level at hour "0" is assumed to be 50% of its battery capacity. Figure 3 presents the EVs' electricity consumption allocation for the trips conducted during the examined day.

Table 4  
EVs techno-economic data

<b>Electric vehicle type</b>	<b>Number of electric vehicles</b>	<b>Charging, discharging efficiency (%)</b>	<b>Charging, discharging power (MW)</b>	<b>Battery capacity (MWh)</b>
EV-1	300	95	0.0072	0.0173
EV-2	50	95	0.011	0.1
EV-3	250	95	0.0037	0.0076
EV-4	150	95	0.0046	0.0358
EV-5	250	95	0.0037	0.023

In both directions, the reserve requirements are assumed to be 20% of the reference electricity demand. Diesel-fired generating units will receive a reserve provision price of 10 €/MW, ESS of 12 €/MW, EVs of 15 €/MW, the grid will receive 20 €/MW, and DRPs will receive 25 €/MW.

Lastly, the electricity interconnection capacity with the mainland power system in both directions is assumed to be 250 MW.

An additional case study ("Energy transition case") has been executed to assess the case where RES more than cover the expected electricity load. In particular, the installed capacity of both wind and solar power is assumed to be 1000 MW each. Moreover, the battery storage capacity increases to 1000 MWh with the same

techno-economic data as in the reference case. Finally, the reserve provision price of all providers (diesel-fired units, ESS, EVs, DRPs, RES) is assumed to be 10 €/MW.

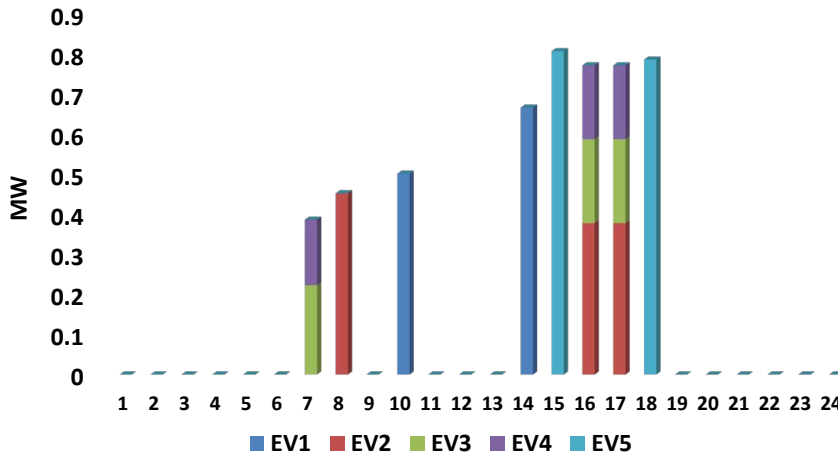


Figure 3

EVs electricity consumption on an hourly basis

## 4 Results and Discussion

The problem has been globally optimized using the CONOPT solver within the General Algebraic Modeling System (GAMS) Studio 37 [16]. An optimality gap of 0% has been achieved.

### 4.1 Reference Case

The total daily operating cost of the islanded power system amount to around 1.77 million €. This value is quite important when compared to the case where there is no electricity interconnection with the mainland power system, where the corresponding number equals around 3.1 million €. The net cost of purchasing electricity makes up 71% of the 1.77 million euros; the remaining cost is split between the generation cost of diesel-fired units (26%) and the cost of providing reserves (3%). The energy supply and demand mix of the analyzed islanded power system is shown in Figure 4 on an hourly basis. With their charging and discharging cycles, ESSs and EVs make energy allocation easier for several hours a day. The main charging hours for ESSs are the 6<sup>th</sup> and the 24<sup>th</sup> hours, as well as the EVs are being charged during the 1<sup>st</sup> day hour and the time interval between hours 3-5.

ESSs discharge during the 1<sup>st</sup> and the 8<sup>th</sup> day hours, and the EVs during 8<sup>th</sup>, 9<sup>th</sup> and 22<sup>nd</sup> day hour. There is also a model assumption that the storage levels at both ESSs and EVs must remain unchanged between the beginning (hour "0") and the end (hour "24") of the examined day. Figure 5, which depicts the daily allocation of energy supply, demonstrates that the grid's net imports share accounts for nearly 49% of the total supply, followed by diesel-fired generators, which stand for 28%, and RES, whose share represents the remaining 23%. In the case of the absence of electricity interconnection with the mainland power system, diesel-fired power generators meet around 77% of the total electricity contribution, and the remaining 23% is supplied by RES power units.

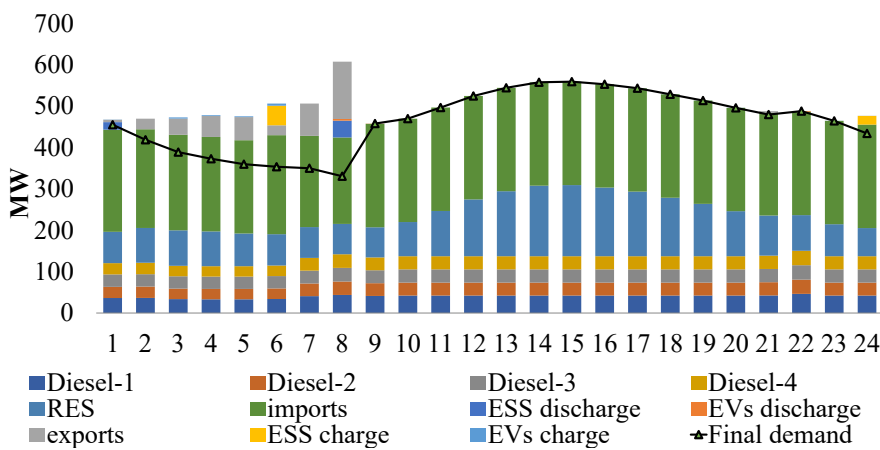


Figure 4

Hourly energy supply and demand mix of the examined islanded power system

The operating-up reserve provision mix of the analyzed islanded power system is depicted in Figure 6. Diesel-fired generators are the only ones providing this service, and they are regarded as the most cost-effective means of doing so. Figure 7 depicts how they operate close to their technical minimums and remain operational throughout the day. As a result, they may be able to provide this upward service by increasing their power output. This is also the case in the scenario without electricity interconnection with the mainland power system, where the diesel-fired power generators operate between 52% and 67% of their technical maximums, as depicted in Figure 8. Thus, there is enough capacity to provide, that upward service, during all of the day hours.

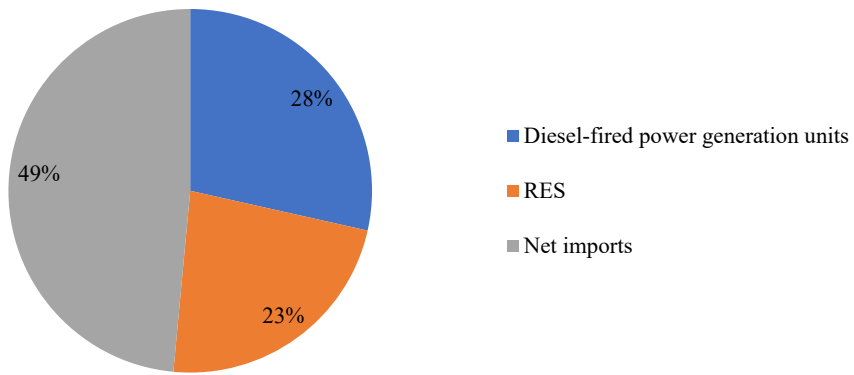


Figure 5  
Daily energy supply allocation of the examined islanded power system

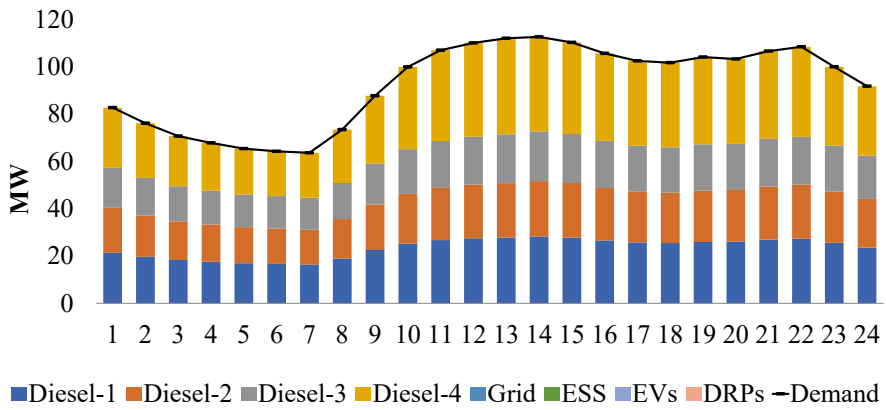


Figure 6  
Operating-up reserve provision mix of the examined islanded power system

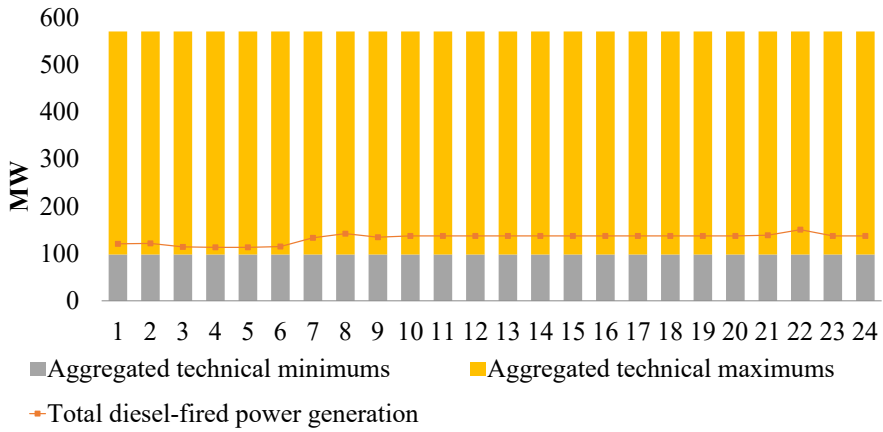


Figure 7

Hourly diesel-fired power generation of the examined islanded power system in the case of electricity interconnection with the mainland power system

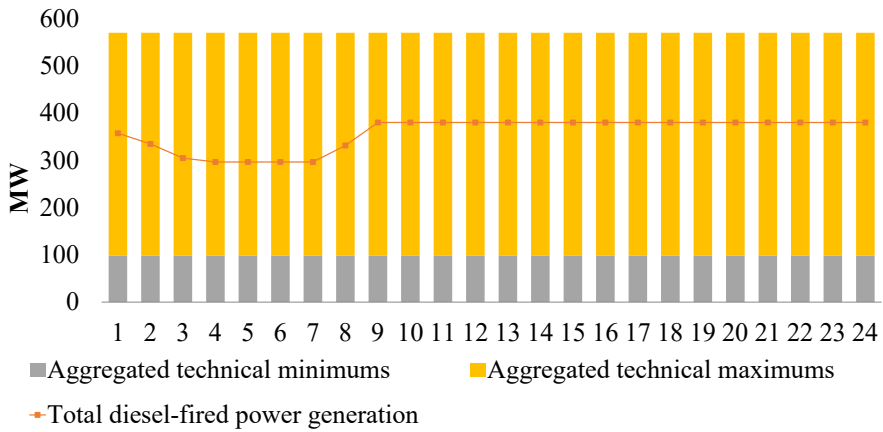


Figure 8

Hourly diesel-fired power generation of the examined islanded power system in the case of no electricity interconnection with the mainland power system

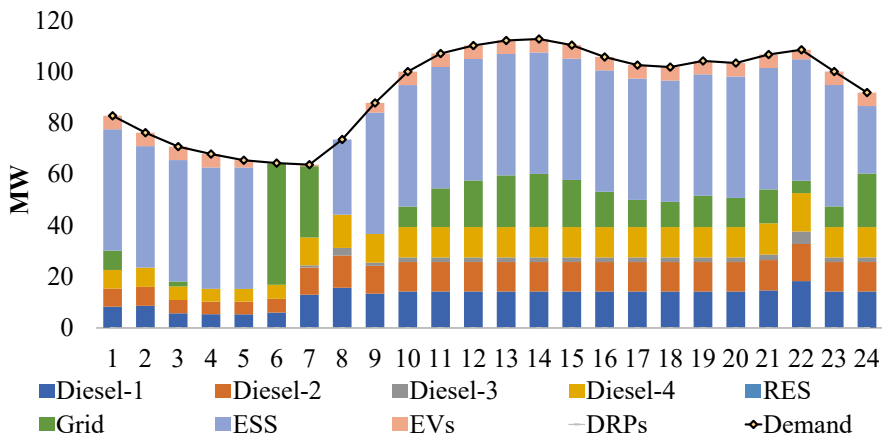


Figure 9

Operating-down reserve provision mix of the examined islanded power system

The operating-down reserve provision mix of the analyzed islanded power system is depicted in Figure 9. On a daily basis, the ESS meets 45% of that service's total requirements. Diesel-fired units account for approximately 37% of total requirements, while EVs cover almost 5% of daily requirements. It is important to note that the electricity interconnection with the power system on the mainland contributes to the service's coverage, providing approximately 13% of the total daily requirements. Note that due to the fact that the diesel-fired power units operate at medium levels in the case of no electricity interconnection with the mainland power system (see Figure 7), they have increased capability to provide also downward service. In particular, they cover the whole daily needs in that case.

The modified and reference electricity demands of the studied islanded power system are shown in Figure 10. Although the total daily load remains unchanged, there are distinct patterns in the allocation of the hourly electricity demand. During the hours when the net reference electricity demand is at its lowest, the modified electricity demand is characterized by some increases compared to the reference demand. These times are between 1 and 7 hours, 9 hours, and 15 to 18 hours. During specific hours, namely 8<sup>th</sup>, 10<sup>th</sup>-14<sup>th</sup> and 19<sup>th</sup>-24<sup>th</sup>, the modified electricity demand decreases somewhat in comparison to the reference. The model determines the best scheduling strategy to reduce these peak periods of the net reference electricity demand in order to satisfy the net load at a more cost-effective rate. The results are almost identical when the electricity interconnection, with the mainland power system, is not included.

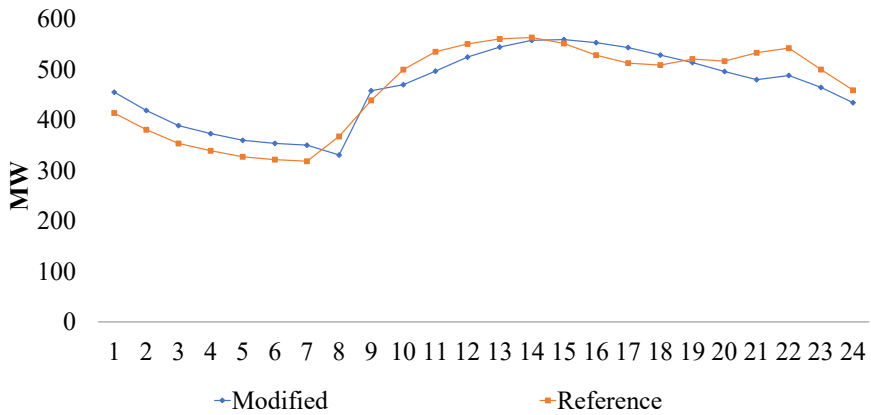


Figure 10

Modified and reference electricity demand of the examined islanded power system

Figure 11 portrays the state-of-charge levels of each EV type of the examined islanded power system. It is assumed in the case study adopted that the storage level at the time period prior to the optimization process (hour "0") and the last day hour, namely the 24<sup>th</sup> one, must remain the same and amount to 50% of the aggregated battery capacity of each EV type. It can be observed that the 6<sup>th</sup> and 7<sup>th</sup> hours comprise the ones where the battery capacities are almost full for all EV types, and they gradually discharge, either selling electricity to the grid or using it for their consumption for the conduction of their trips, to reach the 50% level at the end of the day.

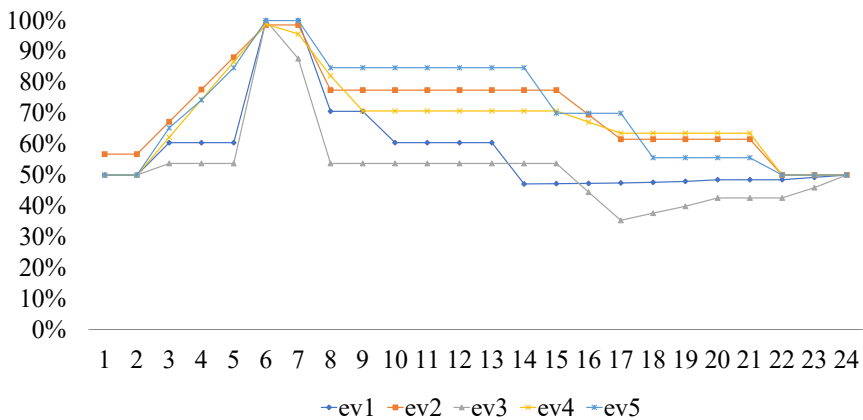


Figure 11

Aggregated state-of-charge levels of each EV type of the examined islanded power system

## 4.2 Energy Transition Case

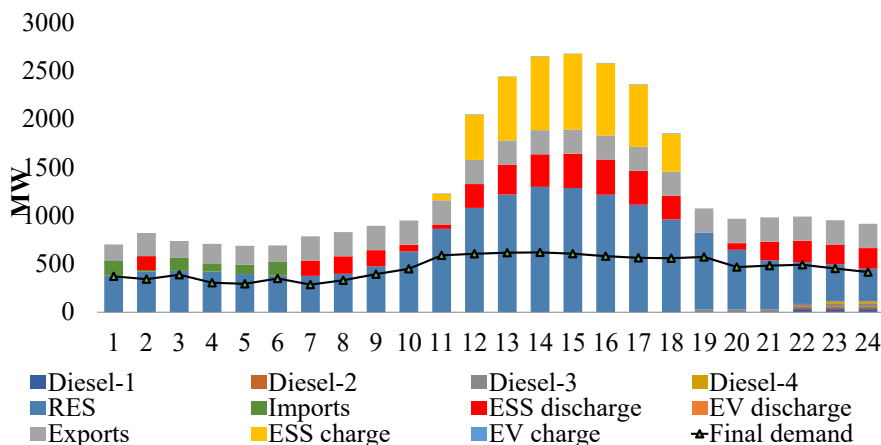


Figure 12

Hourly energy supply and demand mix of the examined islanded power system in the Energy Transition case

Figure 12 depicts the hourly energy supply and demand mix of the examined islanded power system in the Energy Transition case. This case is characterized by high penetration of RES in the power system. The results show that the islanded power system has been converted into a net electricity exporter, reporting around 5 GWh of net exports. Electricity imports occur only during the first 6 hours of the day when there is zero production from photovoltaics, and the diesel-fired power units are shut down. The aggregated electricity generation from diesel-fired power units has been minimized to less than 0.4 GWh daily, while ESS flexibility (charging and discharging cycle) is used during almost all of the hours of the day.

Figure 13 portrays the operating-up reserve provision mix of the examined islanded power system in the Energy Transition case. In contrast to the reference case where diesel-fired power units exclusively meet this service, there is a great diversification of that service's coverage in the Energy transition one. ESS contributes around 39% of the total daily needs, followed by the main grid with around 36%, the DRPs with almost 14%, diesel-fired power units with 9%, and EVs with less than 2%.

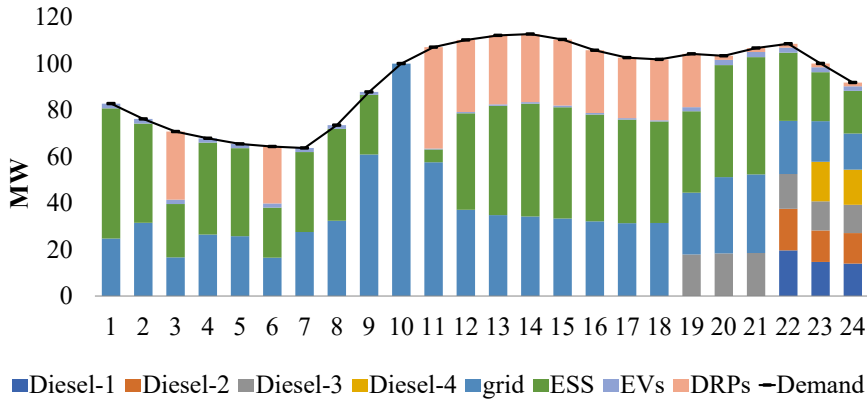


Figure 13

Operating-up reserve provision mix of the examined islanded power system in the Energy Transition case

Figure 14 portrays the operating-down reserve provision mix of the examined islanded power system in the Energy Transition case. All the available providers take part in the coverage of that service, with RES accounting for around 45%, ESS standing for 35%, DRPs with almost 13%, electricity interconnection with less than 5%, EVs with almost 2% and an almost negligible share from diesel-fired power units.

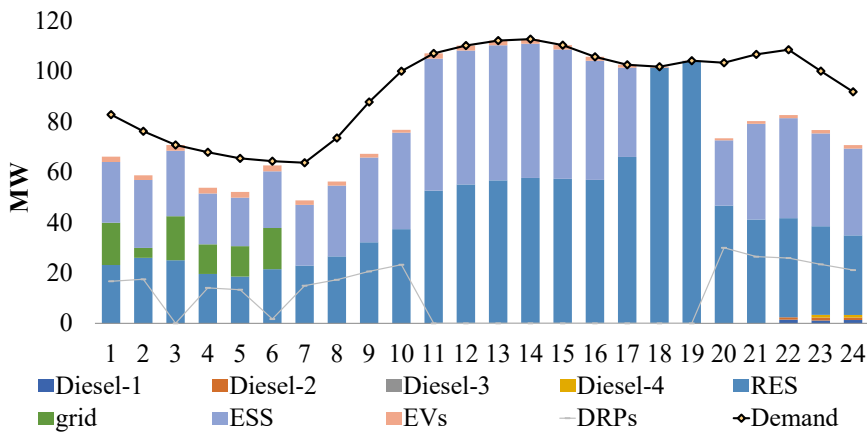


Figure 14

Operating-up reserve provision mix, for the examined islanded power system, in the Energy Transition case

### Conclusions

In their efforts to meet their electricity needs in a dependable, cost-effective and long-term manner, islanded power systems face numerous obstacles. Taking into

account the existence of various flexibility providers like ESS, EVs, and DRPs, this work proposes an optimization strategy, based on mixed-integer quadratic programming, to optimally determine an islanded power system's energy and reserves scheduling. It also examines the role that electricity interconnections play as providers of energy and reserve.

The results emphasize the significance of including these resources in the mix of energy and reserves, which may be even more significant, in the event of extremely high-RES penetration. In addition, the model outputs highlight the economic significance, when considering the electricity interconnection, with the mainland power system, compared to the case without.

All of these flexibility providers' design decisions and detailed testing of their performance on mid- and long-term planning frameworks, are future challenges.

### Acknowledgment

This work received no external funding.

### References

- [1] Poncela Blanco M; Spisto A; Fulli G; Hrelja N. Generation Adequacy Methodologies Review. EUR 27944. Luxembourg (Luxembourg): Publications Office of the European Union; 2016. JRC101590
- [2] S. Misconel, R. Leisen, J. Mikurda, F. Zimmermann, C. Fraunholz, W. Fichtner, D. Möst, C. Weber, Systematic comparison of high-resolution electricity system modeling approaches focusing on investment, dispatch and generation adequacy, *Renewable and Sustainable Energy Reviews*, Volume 153, 2022, 111785, ISSN 1364-0321, <https://doi.org/10.1016/j.rser.2021.111785>
- [3] Hans Christian Gils, Hedda Gardian, Martin Kittel, Wolf-Peter Schill, Alexander Zerrahn, Alexander Murmann, Jann Launer, Alexander Fehler, Felix Gaumnitz, Jonas van Ouwkerk, Christian Bußar, Jennifer Mikurda, Laura Torralba-Díaz, Tomke Janßen, Christine Krüger, Modeling flexibility in energy systems — comparison of power sector models based on simplified test cases, *Renewable and Sustainable Energy Reviews*, Volume 158, 2022, 111995, ISSN 1364-0321, <https://doi.org/10.1016/j.rser.2021.111995>
- [4] P. González, J. Villar, C. A. Díaz, and F. A. Campos, "Joint energy and reserve markets: Current implementations and modeling trends". *Electric Power Systems Research*, Vol. 109, 2014, pp. 101-111, doi: 10.1016/j.epsr.2013.12.013
- [5] S. S. Reddy, P. R. Bijwe and A.R. Abhyankar, "Optimum day-ahead clearing of energy and reserve markets with wind power generation using anticipated real-time adjustment costs". *International Journal of Electrical Power & Energy Systems*, October 2015, Vol. 71, pp. 242-253, doi: 10.1016/j.ijepes.2015.03.002

- 
- [6] G. Liu, and K. Tomsovic, "A full demand response model in co-optimized energy and reserve market". *Electric Power Systems Research*, June 2014, Vol. 111, pp. 62-70, doi: 10.1016/j.epsr.2014.02.006
- [7] M. Carrion, and J. M. Arroyo, "A computationally efficient mixed-integer linear formulation for the thermal unit commitment problem". *IEEE Transactions on Power Systems*, Aug. 2006, Vol. 21, No. 3, pp. 1371-1378, doi: 10.1109/TPWRS.2006.876672
- [8] A. Viana, and J. P. Pedroso, "A new MILP-based approach for unit commitment in power production planning". *International Journal of Electrical Power & Energy Systems*, January 2013, Vol. 44, No. 1, pp. 997-1005, doi: 10.1016/j.ijepes.2012.08.046
- [9] D. Divényi, B. Polgári, Á. Sleisz, P. Sörös, and D. Raisz, "Algorithm design for European electricity market clearing with joint allocation of energy and control reserves". *International Journal of Electrical Power & Energy Systems*, October 2019, Vol. 111, pp. 269-285, doi: 10.1016/j.ijepes.2019.04.006
- [10] N. E. Koltsaklis, A. S. Dagoumas, "Incorporating unit commitment aspects to the European electricity markets algorithm: An optimization model for the joint clearing of energy and reserve markets". *Applied Energy*, December 2018, Vol. 231, pp. 235-258, doi: 10.1016/j.apenergy.2018.09.098
- [11] N. Koltsaklis, A. Dagoumas, "Policy Implications of Power Exchanges on Operational Scheduling: Evaluating EUPHEMIA's Market Products in Case of Greece". *Energies*, October 2018, Vol. 11, 2715, doi: 10.3390/en1102715
- [12] M. Zugno, and A. J. Conejo, "A robust optimization approach to energy and reserve dispatch in electricity markets". *European Journal of Operational Research*, December 2015, Vol. 247, No. 2, pp. 659-671, doi: 10.1016/j.ejor.2015.05.081
- [13] F. Wen, and A. K. David, "Coordination of bidding strategies in day-ahead energy and spinning reserve markets". *International Journal of Electrical Power & Energy Systems*, May 2002, Vol. 24, No. 4, pp. 251-261, doi: 10.1016/S0142-0615(01)00038-2
- [14] M. E. Nazari, and M. M. Ardehali, "Optimal bidding strategy for a GENCO in day-ahead energy and spinning reserve markets with considerations for coordinated wind-pumped storage-thermal system and CO2 emission". *Energy Strategy Reviews*, November 2019, Vol. 26, pp. 100405, doi: 10.1016/j.esr.2019.100405
- [15] E. Lobato, L. Sigrist, and L. Rouco. "Value of electric interconnection links in remote island power systems: The Spanish Canary and Balearic archipelago cases". *International Journal of Electrical Power & Energy Systems*, 2017, Vol. 91, pp. 192-200, 10.1016/j.ijepes.2017.03.014

- [16] A. Brooke, D. Kendrick, A. Meeraus, and R. Raman, "GAMS: A User's Guide", GAMS Development Corporation, Washington D.C., 1998

## Appendix

### Nomenclature

#### Sets

$t$	Time periods
$i$	Conventional power units (Diesel-fired power generators)
$r$	Renewable Energy Sources (RES)
$v$	Electric Vehicles (EVs)
$w$	Energy Storage Systems (ESSs)
$y$	Demand Response Programs (DRPs)
$n$	Upward reserve supplier resources (Conventional, ESSs, EVs, DRPs, Grid)
$m$	Downward reserve supplier resources (Conventional, ESSs, EVs, DRPs, Grid, RES)

#### Parameters

$C_i^{stup}$	Unit's $i$ start-up cost
$C_{m,t}^{dn}$	Unit's $m$ operating-down reserve provision cost
$C_{n,t}^{up}$	Unit's $n$ operating-up reserve provision cost
$C_{r,t}^{curt}$	RES curtailment cost
$DT_i$	Unit's $i$ minimum downtime
$D_{y,t}^{max}$	Maximum DRP consumption
$D_{y,t}^{min}$	Minimum DRP consumption
$D_{y,t}^{ref}$	DRP reference consumption level
$EXP_t^{cap}$	Maximum value of electricity exports
$E_{v,t}^{cons}$	EV energy consumption
$F_{r,t}$	RES availability factor
$G_v^{ch-max}$	EV maximum charging power
$G_v^{dis-max}$	EV maximum discharging power
$G_w^{ch-max}$	ESS maximum charging power
$G_w^{dis-max}$	ESS maximum discharging power
$IMP_t^{cap}$	Maximum value of electricity imports
$P_i^{max}$	Unit's $i$ technical maximum
$P_i^{min}$	Unit's $i$ technical minimum
$RD_i$	Unit's $i$ ramp-down limit
$RU_i$	Unit's $i$ ramp-up limit
$R_t^{dn}$	Operating-down reserve requirements
$R_t^{up}$	Operating-up reserve requirements
$SF_v^{ch}$	EV charging efficiency
$SF_v^{dis}$	EV discharging efficiency
$SF_w^{ch}$	ESS charging efficiency

$SF_w^{dis}$	ESS discharging efficiency
$SOC_v^{max}$	EV battery capacity
$SOC_v^{min}$	EV minimum allowable state-of-charge level
$SOC_w^{max}$	ESS maximum capacity
$SOC_w^{min}$	ESS minimum allowable state-of-charge level
$UT_i$	Unit's $i$ minimum uptime
$a_i, b_i, c_i$	Production cost coefficients of unit $i$
$n_v^{tot}$	Number of EVs of each EV type

### Variables

$c_{i,t}^{prod}$	Unit's $i$ production cost in each time period $t$
$d_{y,t}^{cl}$	Cleared DRP energy consumption
$imp_t$	Electricity imports in each time period $t$
$exp_t$	Electricity exports in each time period $t$
$d_{y,t}^{dn}$	Downward DRP energy consumption
$d_{y,t}^{up}$	Upward DRP energy consumption
$p_{i,t}^{conv}$	Unit's $i$ cleared total energy supply in each time period $t$
$p_{r,t}^{curt}$	Cleared amount of RES curtailed in each time period $t$
$p_{r,t}^{res}$	Cleared contribution of each RES directly utilized in each time period $t$
$p_{v,t}^{ch}$	Cleared EV charging power in each time period $t$
$p_{v,t}^{dis}$	Cleared EV discharging power in each time period $t$
$p_{w,t}^{ch}$	ESS cleared charging power in each time period $t$
$p_{w,t}^{dis}$	ESS cleared discharging power in each time period $t$
$r_{n,t}^{up}$	Unit's $n$ cleared operating-up reserve supply
$r_{m,t}^{dn}$	Unit's $m$ cleared operating-down reserve supply
$r_t^{up}$	Operating-up reserve supply from the mainland power system
$r_t^{dn}$	Operating-down reserve supply from the mainland power system
$soc_{v,t}^{ev}$	EV state-of-charge level
$soc_{w,t}^{st}$	ESS state-of-charge level

### Binary variables

$y_{i,t}$	Unit's $i$ start-up decision-making in each time period $t$
$z_{i,t}$	Unit's $i$ shut-down decision-making in each time period $t$
$x_{i,t}^{oper}$	Unit's $i$ operation decision-making in each time period $t$

### Acronyms

DRPs	Demand Response Programs
ESSs	Energy Storage Systems
EVs	Electric Vehicles
RES	Renewable Energy Sources